Gravity and Magnetic Fields of Small Planets

M.Sc. Kurosh Karimi

A dissertation submitted for the degree of Doctor of Philosophy

Supervisor: prof. RNDr. Gunther Kletetschka, Ph.D.

Charles University, Faculty of Science

Institute of Hydrogeology, Engineering Geology and Applied Geophysics

Prague, 2024

Prohlášení

Tímto prohlašuji, že jsem předkládanou diplomovou práci vypracoval(a) samostatně. Práce uvedená v této diplomové práci nebyla předložena k získání žádného jiného odborného titulu. V případě společně autorských publikací byla řádná zásluha vždy výslovně uvedena. Všechny citované reference a zdroje informací jsou uvedeny na konci této diplomové práce.

V Praze, červenec 2024

Kurosh Karimi

Acknowledgement

I would like to express my deepest gratitude to those who have supported and guided me throughout the journey of completing my PhD thesis.

First and foremost, I want to thank my wife, Atefeh and my beloved daughter, Mahoora. Your unwavering love, patience, and encouragement have been my greatest source of strength. Without your support, this accomplishment would not have been possible. You have been my rock, my confidante, and my biggest cheerleader, and for that, I am truly grateful.

I am also deeply indebted to my supervisor, Prof. Gunther Kletetschka. Your expert guidance, insightful feedback, and constant encouragement have been invaluable throughout my research. Your dedication to my academic and professional growth has profoundly impacted my work and my life. Thank you for believing in me and pushing me to achieve my best.

And lastly, I would like to extend my sincere thanks to Professors Mark Wieczorek, Jeff Andrews-Hanna and Jaroslav Klokočník. I am grateful for your support and constructive comments on my manuscripts during my work.

List of publications

During my doctoral studies, I worked on 4 research articles. In three out of four, I am the first author where I made the main contributions.

The articles are as follows:

- Distribution of water phase near the poles of the Moon from gravity aspects
- Comparison between the geological features of Venus and Earth based on gravity aspects
- Formation of Australasian tektites from gravity and magnetic indicators
- Subsurface geology detection from application of the gravity-related dimensionality constraint

Content

List of Tables

List of Figures

Abstrakt

Tato diplomová práce zkoumá gravitační a magnetické aspekty (funkcionály) odvozené z tenzoru gradientu gravitace (GGT) a tenzoru magnetického gradientu (MGT). Tyto funkcionály zahrnují topografii, gravitační poruchu, složky GGT, invarianty GGT, úhel úderu, kombinační faktor, celkové magnetické pole, redukované magnetické pole, složky MGT, celkový horizontální gradient, úhel sklonu, logistický celkový horizontální gradient a filtry pro pokračování směrem nahoru a dolů. Hlavním účelem tohoto výzkumu je komplexně identifikovat tyto všestranné funkcionály a aplikovat je na Zemi, Měsíc a Venuši, což vyústilo ve čtyři recenzované články.

1. Lokace s přítomností vody na Měsíci: Analýza gravitačních aspektů, zejména úhlů úderu, odhaluje potenciální lokace s přítomností vody v polárních oblastech Měsíce, což naznačuje oblasti s tekutými a ledovými vodními ložisky. Tyto nálezy jsou klíčové pro budoucí lunární průzkum a vývoj habitatů, zejména v souvislosti s procesem „impact gardening“.

2. Srovnávací analýza Země a Venuše: Vzhledem k podobným gravitačním vlastnostem Země a Venuše aplikace gravitačních funkcionálů - včetně topografie, složek GGT, úhlu úderu, kombinačního faktoru a invariantů GGT - odhaluje rozdíly v subdukčních rysech, úrovních deformace, složitých vulkanických procesech a mantlových pláštech na obou planetách.

3. Struktura impaktu v poušti Badain Jaran: Vyšetřování potenciálních funkcionálů pole, včetně volné vzdušné a Bouguerovy gravitační anomálie, složek GGT a MGT, celkového horizontálního gradientu, logistického celkového horizontálního gradientu, úhlu úderu, kombinačního faktoru, magnetického pole a jeho transformace redukované na pól, podporuje existenci pohřbené impaktní struktury v poušti Badain Jaran, severozápadní Čína. Tato struktura je charakterizována ročními gravitačními výškami, preferovanými paralelními směry a magnetickými anomáliemi indikujícími rázové vlny a magnetizační vzory, což poskytuje vhled do identifikace impaktních kráterů a regionálních geologických procesů.

4. Odhad hloubky anomálních těles: Aplikace gravitačních aspektů, jako jsou gravitační porucha, složky a invarianty GGT, nabízí nový způsob odhadu hloubky podzemních anomálních těles s různými rozměry. Tato metoda poskytuje odhady horizontální lokace a hloubky na základě relativních variací v horizontálním rozsahu způsobujícího tělesa, přičemž zohledňuje různé typy těles a hloubky. Testování na měsíčních datech a různých modelových scénářích demonstruje účinnost metody, což naznačuje její použitelnost jak v planetárních, tak inženýrských kontextech.

Abstract

This thesis explores the gravity and magnetic aspects (functionals) derived from the gravity gradient tensor (GGT) and magnetic gradient tensor (MGT). These functionals include topography, gravity disturbance, GGT components, GGT invariants, strike angle, comb factor, total magnetic field, reduced-to-pole total magnetic field, MGT components, total horizontal gradient, tilt angle, logistic total horizontal gradient, and upward and downward continuation filters.

The primary purpose of this research is to comprehensively identify these versatile functionals and apply them to Earth, the Moon, and Venus, culminating in four peer-reviewed papers.

1. Lunar Water-Bearing Locations:
The analysis of gravity aspects, particularly strike angles, reveal potential water-bearing locations in the lunar polar regions, indicating areas with liquid and ice water deposits. These findings are crucial for future lunar exploration and habitat development, especially concerning the process of Impact gardening.
2. Comparative Analysis of Earth and Venus:
Given the similar gravitational properties of the Earth and Venus, the application of the gravity functionals- including topography, GGT components, strike angle, comb factor and GGT invariants- unravel differences in subduction features, deformation levels, complex volcanic processes, and mantle plumes on the two planets.
3. Impact Structure in Badain Jaran Desert:
The investigation of the potential field functionals, including free air and Bouguer gravity anomalies, GGT and MGT components, total horizontal gradient, logistic total horizontal gradient, strike angle, comb factor, magnetic field, and its reduced-to-pole transformation, supports the existence of a buried impact structure in Badain Jaran Desert, northwest China. This structure is characterized by annual gravity heights, preferred parallel directions, and magnetic anomalies indicative of shock waves and magnetization patterns, providing insights into impact crater identification and regional geological processes
4. Depth Estimation of Anomalous Bodies: .
The application of gravity aspects, such as gravity disturbance, GGT components and invariants, offers a novel method for estimating the depth of underground anomalous bodies with varied dimensions. This method provides horizontal location and depth estimates based on the relative variations in the horizontal extent of the causative body, accommodating different body types and depths. Testing on lunar data and various model scenarios demonstrates method's effectiveness, suggesting its applicability inn both planetary and engineering contexts.

Chapter 1

Introduction

1.1 Objectives and structure of the Thesis

The primary objective of this thesis is to demonstrate the utility of gravity and magnetic aspects in various geophysical applications on Earth, the Moon, and Venus. Through the compilation of four distinct articles, each addressing specific geological features and employing unique analytical method. The thesis aims to provide new insights into the subsurface characteristics of these celestial bodies. Each Article leverages specific sets of gravity and/or magnetic parameters. The articles are presented in chronological order of their publication to illustrate the progression and development of the research.

1. Article 1: *Distribution of Water Phase Near the Poles of the Moon from Gravity Aspects*
    - Objective: Identify potential water-bearing sites in the lunar polar regions using gravity aspects derived from the Moon's gravity field model.
    - Key Findings: Suggested the presence of water in the polar regions of the Moon, potentially originating from terrestrial hydrogen and oxygen ions. Highlighted the importance of these findings for future lunar research and human colonization.
2. Article 2: *Comparison Between the Geological Features of Venus and Earth Based on Gravity Aspects*
    - Objective: Compare the gravitational properties of Venus and Earth to understand their geological features and tectonic activities.
    - Key Findings: Found similarities and differences in the gravitational characteristics of specific zones on Venus and Earth. Suggested no subduction character for Lakshmi Planum on Venus and compared Venus's equatorial rifting zone with the East African Rift system on Earth.
3. Article 3: *Formation of Australasian Tektites from Gravity and Magnetic Indicators*
    - Objective: Locate the parent crater of Australasian tektites using gravity and magnetic data.
    - Key Findings: Identified a potential impact structure in the Badain Jaran Desert, Northwest China. Combined gravity and magnetic analyses indicated the presence of an impact crater, contributing to the understanding of tektite formation and distribution.
4. Article 4: *Subsurface Geology Detection from Application of the Gravity-Related Dimensionality Constraint*
    - Objective: Develop a method for detecting subsurface geological features using gravity-related dimensionality constraints.
    - Key Findings: Generalized the application of dimensionality indicators for a spectrum of dimensionalities, improving depth estimation of anomalous bodies. Validated the method with lunar data, showing its efficacy in geological studies.

Each article contributes to the overarching goal of the thesis by employing gravity and/or magnetic aspects to uncover new geological insights across different planetary bodies. The comprehensive approach taken in these studies showcases the versatility and effectiveness of these geophysical tools in advancing our understanding of planetary geology.

1.2 Potential Field Data and Its Aspects

Potential field data is a type of geophysical method through the measurement of natural variations in the gravitational or magnetic fields of the planets [1–4]. These variations are caused by differences in the density or magnetic properties of geological structures and/ or subsurface materials like fault, fracture,

fold, schistosity, and different units of rocks and minerals [1]. The potential field method is widely used for exploration purposes [5–16] and planetary-scale investigations [17–24]. Interpretation of the potential field data often involves processing and analyzing the data to create maps or models of subsurface geological features and anomalies. A thorough study of potential field data could be found in [1,3,4,25,26]. For, specifically, gravity and geodesy analysis the reader is referred to Heiskanen and Moritz (1967)[2] and Hofmann-Wellenhof and Moritz (2006)[27]. Two tensors resulting from the gravity and magnetic potentials are, respectively, Gravity Gradient Tensor (GGT or Marussi tensor) and Magnetic Gradient Tensor (MGT). These tensors along with mathematical compositions derived from their components give us a set of tools, called "gravity and magnetic functionals" or "gravity and magnetic aspects" [22]. It is worth mentioning that we use GGT and Marussi tensor interchangeably. Moreover, the terms "gravity functionals" and "gravity aspects" are employed interchangeably, in this thesis. The same is the case for the terms "magnetic functionals" and "magnetic aspects".

There are various forward and inverse modelling techniques to locate potential field anomalies and their density/ magnetization contrast in the literature. Thompson (1982) [28] introduced a method for estimating causative bodies' location based on Euler's homogeneity relationship, which enabled the investigation of subsurface magnetic anomalies with diverse shapes. This approach was later expanded upon by others, such as Reid et al., (1990)[29], who applied Euler's equation to estimate the positions of gravity anomalies. The analysis of the GGT and MGT by Pedersen and Rasmussen (1990)[13] significantly enhanced the utility of the potential field data, leading to extraction of valuable information from geological bodies with contrasting density and/or magnetic properties. In fact, their work on GGT and MGT provided quantitative insights into strike direction, horizontal dimensions, and locations of subsurface anomalies, and became a cornerstone of subsequent research by others [17,30,5,11,12,31–34,21,35–37,22,38–44,18]. These researchers developed various techniques for strike, depth, deformational state, and edge estimation of potential field anomalies, representing various geological features.

Pedersen and Rasmussen (1990)[13] presented three invariants of GGT and MGT to show how source dimensionality and amplification of high frequency signals work. They also indicated that the maximum eigenvalues and their corresponding eigenvectors are related to the locations of simple-shaped gravity and magnetic sources. Although their work was exceptional, they did not develop any practical techniques for estimating complex-shaped bodies' location. Additionally, they neglected the interpretive power contained in the eigenvector corresponding to the minimum eigenvalue.

Zhang et al., (2000)[41] and Mikhailov et al., (2007)[38] demonstrated that rather than relying on the gravity anomaly itself, leveraging the components of the GGT can enhance the effectiveness of the Euler deconvolution technique. Beiki and Pedersen (2010)[5] developed a new method to locate complex geologic bodies using eigenvector analysis of the GGT through least squares procedure, where the eigenvectors corresponding to the largest and smallest eigenvalues were applied to estimate the position of the source bodies and strike directions, respectively. Beiki et al.,[30] utilized the simultaneously contrasting gravity and magnetic properties of igneous structures and introduced the Psuedo-gravity gradient tensor in study of such geological constructs. Karimi and Shirzaditabar (2017)[31] computed the components of MGT with the aid of Fourier transform and could approximate the depth of magnetic bodies underground using Analytic Signals obtained from the anomalous TMF and MGT components.

Instead of directly measured GGT components, Karimi et al., [12] proposed solutions for calculating the GGT components from the measured gravity anomaly and applied them to depth and strike detection of the anomalous underground masses. In parallel, they analyzed the behavior of the MGT tensor to estimate the depth of the simple shaped magnetic bodies [11]. They indicated that though the eigenvector analysis of MGT is not as informative as that of GGT, it could still be a useful source of information in magnetometry surveys.

Zhou (2015)[42] expanded the application of the normalized imaging technique to interpret GGT data and analyze normalized directional analytic signals to determine the horizontal position and depth range of

salt dome structures. Zuo et al., (2017)[44] introduced a novel approach utilizing eigenvector analysis to identify the centroids and horizontal boundaries of geological formations from GGT data. This method employed eigenvector analysis to extract centroid information, diverging from traditional boundary detection techniques in potential field analysis. The study delved into the theoretical underpinnings and practical significance of eigenvector analysis in GGT, addressing challenges associated with multiple sources and parameter identification. Yuan et al., (2020)[40] proposed an innovative depth estimation method based on the Chebyshev–Padé downward continuation technique, with an emphasis on stability and accurate depth calculation. The research compared filter curves in the wave number domain between Tikhonov regularization and Chebyshev–Padé methods, highlighting the superior convergence of the latter's filter curve to zero, rendering it suitable for precise depth estimation. Zhou et al., (2021)[43] enhanced the normalized imaging method by integrating the downward continuation technique based on continued fractions, enabling the determination of geometric parameters of sources across various depths.

In a planetary scale, analysis of the eigenvectors of the GGT obtained from the GRAIL mission's gravity field model, (Andrews-Hanna et al (2013)[18] revealed numerous long linear gravity anomalies within the lunar crust, which were not observable geologically. These anomalies suggest likely ancient intrusions formed by magmatism and lithospheric extension. They attributed these features to an early increase in the Moon's radius according to thermal models. Andrews-Hanna et al., (2016) [17] also conducted the eigenvector analysis of GGT over selected regions of Venus where the data resolution is sufficiently high to provide geological interpretations for the observed GGT signature. In a series of papers, Klokocnik's team [21,22,32–36,45,46] employed the gravity aspects of Earth, Moon, and Mars. They studied the pore-space and fractured structures around impact craters, paleolakes and subglacial volcanoes and subglacial lakes on these planets. They made use of the most recent gravity field model for each planet and opened new windows towards more research in geological and geophysical scopes. One of the main defects in Klokocnik's approach in SA was that his choice of coordinate system was not consistent with the coordinate system in which the strike angles were first introduced by Pedersen and Rasmussen (1990)[13]. Consequently, their calculated strike angles were 90 degrees off the actual strike angles that needed to be estimated.

During my PhD, I found this contradiction and modified these angles for satellite gravimetry, where the coordinate systems are different from those for exploration purposes. This modification solves the inconsistency and coincides with the geological evidence, giving sensible information about the geology of the area under investigation. This correction is brought in section 2.12. It is important to note that the components of GGT and MGT can be (1) directly calculated from the gravity and magnetic potentials in the spatial domain [1,4], (2) obtained through Fourier domain transform, and later, back to the spatial domain [1], and (3) measured directly by gravity and magnetic gradiometers [4,5,13,38]. Aside from direct calculation of the gravity potential in spatial domain, we bring in calculation of **g** (gravity vector), **B** (magnetic vector), **GGT** and **MGT** components, RTP (reduction to pole) and upward and downward continuations in the Fourier domain in the "mathematical tools" section (**section 2**).

The aspects or functionals of the gravity field model are defined as gravity disturbance (δg), components (Γ_{ij}) and invariants (I_0, I_1, I_2) of the Marussi tensor. Aside from the Earth, these functionals have been studied for other small planets- Moon [18,23,24,33], Mars [23,47], and Venus [17,19,20,23,48], where the gravity field models are available to certain spherical harmonics degrees and orders. Each functional derived from the gravity field possesses unique characteristics. For instance, traditional δg is commonly employed to assess regional isostatic conditions, elastic thickness, and density variations within the crust [1,23,49]. The Γ_{zz} component and I_2 invariant of the Marussi tensor are particularly effective at amplifying higher frequency signals, making them suitable for identifying properties related to shallow density anomalies . Specific compositions of the GGT components such as total-horizontal-gradient (gravity-THG) can identify the boundaries of anomalous density structures and contact zones, especially at shallow depths [1,4,26,39]. In contrast to the gravity-THG that amplifies the high-frequency/shallow signals, tilt angle of

the gravity field (gravity-TA) could detect the signals from different depths [52]. gravity-TA is specifically useful in delineation of geological constructs with distinct density contrasts buried at various depths. When it comes to detection of the sharp boundaries between contrasting density units, the logistic-total-horizontal-gradient of the gravity field (gravity-LTHG) is one of the newest and most efficient means with the property of boundary detection at different depths [39]. Gravity-LTHG has a parameter, α, that could be adjusted in sharpening the geological boundaries to a desirable extent. As a matter of fact, the excellence of LTHG was evidenced by Pham et al (2019) [39] as compared with other filters already in use, such as THG, TA, Analytic Signal, and Theta map. LTHG is superior to other edge detecting methods in both satellite magnetic and gravity data surveys. Strike alignment (SA) [5,13,32,35] and comb factor (CF) [32,53] can indicate potential structural weaknesses, geological boundaries, and the extent of crustal deformation under specific conditions [54,55].

Though more complicated in nature, the magnetic functionals (aspects), i.e., the anomalous total magnetic field (TMF) and its reduced to the pole transformation (RTP), components of the magnetic gradient tensor (MGT), total-horizontal-gradient of magnetic field (magnetic-THG), tilt-angle of magnetic field (magnetic-TA) and logistic-total-horizontal-gradient of magnetic field (magnetic-LTHG) could serve in characterization of various geological features with distinguished magnetic properties. These magnetic aspects are of similar qualities to their gravity counterparts [1,11,13,31].

TMF has the capability to indicate anomalous magnetized units and their variations [1,4,26]. These areas could occur in the impact basins and their surroundings [56], sites with mineral deposits, volcanic features, and the areas with different types of fault and fracture systems [1,4,26,26,28,32,54]. Having an a priori knowledge of the remanent magnetization direction, the RTP would help horizontal delineation of magnetic anomalous sites [56]. This is particularly useful in identification of the impact crater basins. Like Γ_{zz} component of GGT, B_{zz} component of MGT possesses high-frequency amplification quality which emphasizes the shallow magnetic signals from geological structures and differentiates them from each other [11]. Magnetic-THG serves as a practical tool in detection of the superficially magnetic units [6,37,39]. Regardless of their depth of burial, both shallow and deep-seated magnetic constructs could be simultaneously unraveled by magnetic-TA [39]. Magnetic-LTHG pinpoints the margins between geological units with contrasting magnetic properties/magnetization directions, whether near surface or in depth, with an adjustable α parameter [39].

The other mathematical tools that would increase the efficiency of the potential field data analysis are upward and downward continuation transformations [1,4,10]. These mathematical filters can help remove the high frequency/shallow signals (upward continuation) from geologically anomalous construct or strengthen them (downward continuation). In the case of applying downward continuation filter, however, caution should be taken as it is an unstable transformation, strengthening the noise level resulting in appearance of the artifacts in the potential field study [1].

1.3 Data Resources

We used a number of gravity and topography field models in spherical harmonics format for Moon and Venus. As for the Earth, in addition to gravity and topography, the magnetic field model was also considered. More details can be found in the individual publications [53–55,57].

1.3.1 Moon

Free-Air Gravity Field Model: "GRGM900C"[58], truncated at d/o = 600 and continued downward to an elevation of 0 and 5 km with respect to the reference ellipsoid. The grid resolution of GRGM1200A at d/o = 600 is approximately 10 km on the ground with a precision of around 10 mGal. [58]

Topographic Gravity Model: "STU_MoonTopo720"[59], truncated at a degree and order of 600 to be consistent with "GRGM900C" for calculation of Bouguer anomaly.

Surface Topography Model: lunar digital elevation model of the LOLA[60,61] (Lunar Orbiter Laser Altimeter), an instrument on the payload of Lunar Reconnaissance Orbiter (LRO) spacecraft. The Moon's reference radius is 1737.4 km. The grid resolution of the LOLA altimeter is ~ 10 cm [60].

1.3.2 Earth

Free-Air Gravity Field Model: "EIGEN-6C4" [62]. This model was generated with help of satellite gravity data from the entire GOCE mission. This model has a maximum spherical degree and order of 2160. It reaches a half wavelength resolution of 5×5 arc min (approximately 9 km) on the Earth's surface [62].

Topography Model: "ETOPO1" [63], available in two versions- "Ice Surface" (top of Antarctic and Greenland ice sheets) and "Bedrock" (base of the ice sheets). Both were generated from diverse global and regional digital data sets, shifted to a common datum. ETOPO1 is vertically referenced to sea level, and horizontally referenced to the World Geodetic System of 1984 (WGS 84). The grid resolution is 1 arc-minute.

Magnetic Field Model: EMAG2 [64] is a compilation of measured data from satellite, ship, and airplane. The ground resolution is about 2 × 2 arc min, and the altitude is about 4 km above the geoid.

1.3.3 Venus

Free-Air Gravity Field Model: "Shgi180ua01" [65], is the latest model gained from the Magellan spacecraft (1997) to an attainable maximum spherical degree and order of about 100, with a half wavelength resolution of ~ 1.8×1.8 degrees (~ 190 km) over the Venus' surface. It is the maximum resolution achievable with the available data at its equator. However, in some regions, the resolution decreases to degrees as low as 40. It is expected that a new gravity model of a consistent higher resolution will be provided by the proposed VERITAS mission to Venus [66].

Topography Model: "shtjv360.a01" [67] topography data completed with Pioneer Venus Orbiter topography data. The data were averaged over a rectangular grid in latitude-longitude, with a grid spacing of one degree. This product is a set of two ASCII tables: a header table and a coefficients table, defined below. The Magellan Venus topography model is known as the Spherical Harmonics Topography ASCII Data Record (SHTADR) and is produced by the Magellan Gravity Science Team at JPL.

Chapter 2

Chronological development and the origin of the new ideas and hypotheses behind the four published papers

This thesis is a compilation of four articles, all published in Scientific Reports. It demonstrates the utility of gravity and magnetic aspects in various geophysical applications on Earth and other celestial bodies. Based on the geological features of the areas under investigation, three articles [53,54,57] utilize specific sets of gravity aspects, while one article [55] applies selected sets of gravity and magnetic aspects and filters. I introduce these papers in chronological order of their publication:

1.2.1 In the first papers, "Distribution of Water Phase Near the Poles of the Moon from Gravity Aspects"[53], we proposed the existence of water in the polar regions of the Moon, which probably originate from the terrestrial hydrogen and oxygen ions when the Moon goes through the geomagnetic tail of the Earth for five days per month. These potential permafrost/ water-bearing sites, being of density contrasts due to the presence of water deposited in the faults and fractures around impact craters, could be identified through the gravity aspects-strike anomaly (SA) derived from the spherical harmonic coefficients of the Moon's gravity field model. We suggest that a portion of around 3000 km^3 of water phase of the Earth may have escaped the Earth's atmosphere and distributed in and around pore space regolith of the impact craters located in lunar polar regions. The importance of this study is that it can direct the future research focus on the Moon and delineate some potential sites for colonization of humans on this celestial body.

1.2.2 In the second paper, "Comparison Between the Geological Features of Venus and Earth Based on Gravity Aspects" [54], we made use of the similar gravitational properties of the Earth and Venus. The spherical harmonics coefficients of the two planets were truncated at degree and order of 100 to make this comparison reasonable because the maximum trustable degree and order of the Venus gravity

field model for the surveyed zones is up to 100. We considered only SA, Γ_{zz}, CF and I_2 parameters of the gravity functionals as well as topography for specific zones on the planets. From comparing the Γ_{zz} of Lakshmi Planum on Venus and Indian Peninsula on Earth, we found that the Lakshmi Planum boundaries behave like the Earth's passive margins embracing the Indian Peninsula and suggested no subduction character for this zone. The Pacific and Philippine-North American Contact Zone on Earth exhibits significant deformation due to converging plate motions, as indicated by SA and CF analyses. Conversely, in Venus's equatorial rifting zone (ERZ) between Atla-Beta Regios, deformation is minimal and restricted, attributed to diverging boundaries. As a Venusian analog, the East African Rift system (EAR) on Earth is even, by far, more restricted, and smaller. Analysis of topography and I_2 indicates the complex nature of the topographic rise in Beta Regio. Our findings reveal that certain areas within this volcanic rise are experiencing initial upward movement, with denser mantle material rising towards the surface, resulting in crustal thinning. Meanwhile, other elevated regions show signs of molten and less dense crustal materials beneath. Additionally, some elevated areas are attributed to mantle plumes and local volcanic activities, characterized by high-density underlying material.

1.2.3 The third paper "Formation of Australasian tektites from gravity and magnetic indicators"[55] applies both the satellite-derived gravity and magnetic functionals to the Badain Jaran Desert (BJD), Northwest China. The goal locating the currently unknown parent crater that created Australasian tektites distributed over one sixth of the Earth surface. As for the gravity aspects, we employed both free-air and Bouguer gravity anomalies, gravity-THG, Bouguer and free-air vertical gradients, gravity-TA, and upward continuation filter. To analyse the magnetic signature of the area, aside from the anomalous TMF and RTP, we calculated the magnetic indicators B_{zz}, magnetic-TA and magnetic-LTHG. The combined gravity and magnetic analysis strongly indicate the presence of an impact structure hidden beneath the sands in BJD. Gravity measurements show a characteristic pattern of annular gravity highs surrounding a central gravity low. The SA analysis identifies preferred parallel directions, suggesting that specific zones, both inside and outside the rim, are more susceptible to impact shock waves. The TMF data reveals a significant magnetic anomaly in the southern part of the proposed crater, which is further displaced and confined within the rim by the RTP. The B_{zz} data diminishes long-wavelength anomalies while enhancing and horizontally separating the superficial ones. Finally, the TA and LTHG analyses distinguish between deep-seated and shallow magnetic signals, corresponding to the peak and border magnetization values, respectively.

1.2.4 The fourth paper, "Subsurface geology detection from application of the gravity-related dimensionality constraint"[57] takes advantage of the dimensionality indicator (I), Γ_{zz} and δg, for locating the gravitationally anomalous bodies. Though I was previously used as a tool in determining the structural index of Euler deconvolution method in pure 2-dimensional and 3-dimensional cases by Mikhailov et al (2007) [38], we generalized its application for bodies with a spectrum of dimensionalities from pure-2D to pure 3D. This generalization allows horizontal and depth estimation of causative bodies with respect to their horizontal extent and turns into the final solutions of the Euler Deconvolution and Mikhailov methods for end-member cases, i.e., pure-2D and pure-3D. The approach categorizes causative bodies into two types according to

their horizontal spread: the line of poles to point pole (LOP–PP) category, and the line of poles to plane of poles (LOP–POP) category. This classification facilitates the derivation of two separate solutions. When dealing with objects of limited depth and small size, the depth estimate is related to the center of mass; however, for deep bodies, it is associated with the top surface. We show that depth estimates are influenced by both the depth and dimensionality of the object. As depth increases, the impact of I on estimated depth becomes more pronounced. Furthermore, estimated depth displays fewer errors for higher I values in LOP–POP solutions compared to LOP–PP solutions. We experimented with various model scenarios, including isolated and overlapping sources with and without simulated noise, and applied our method to real lunar data containing significant linear features and surrounding impact basins. The results aligned well with geological expectations and previous studies, validating the method's efficacy. This method excels in accurately determining the depth of anomalous objects across a wide spectrum of dimensionalities, from 2 to 3D.

Chapter 3

Methodology and Mathematical Tools

In this section, we study the required mathematical tools and assumptions to derive the gravity and magnetic aspects. Table 1 represents the definition of the parameters used in the potential field analysis of the small planets in this work.

Table 1: symbol and definition of the parameters for different gravity functionals.

Symbol	Definition
X, Y, Z	Geocentric rectangular coordinate system (Figure 3.1)
r, φ, λ	Spherical radius, spherical latitude and spherical longitude, respectively (Figure 3.1)
x, y, z	Local north oriented frame (LNOF) components; x (north), y (west), z (radially outward from the center of the planet) (Figure 3.1)
x', y', z'	x' (north), y' (east), z' (radially inward to the center of the planet) (Figure 3.1)
e, n, z	e (east) n (north), z (radially outward from the center of the planet) (Figure 3.1)
n, m	Spherical harmonic degree and order, respectively
n_{min}, n_{max}	Minimum and maximum degree of the spherical harmonic expansion, respectively
$\bar{P}_{n,m}(\sin\varphi)$	4π fully normalized associated Legendre function of the first kind of degree n and order m
$\bar{C}_{n,m}, \bar{S}_{n,m}$	4π fully normalized spherical harmonic coefficients of degree n and order m related to global geopotential model
GM, R	Geocentric gravitational constant and radius of the reference sphere, respectively
$\bar{C}^{ell}_{n,m}, \bar{S}^{ell}_{n,m}$	4π fully normalized spherical harmonic coefficients of degree n and order m related to the reference ellipsoid
GM^{ell}, a^{ell}	Geocentric gravitational constant and semimajor axis of the reference ellipsoid, respectively
ω	Angular velocity of the planet
g_x, g_y, g_z	Cartesian components of the gravity field
B_x, B_y, B_z	Cartesian components of the anomalous total magnetic field (TMF)
RTP	Reduced to the pole anomalous TMF

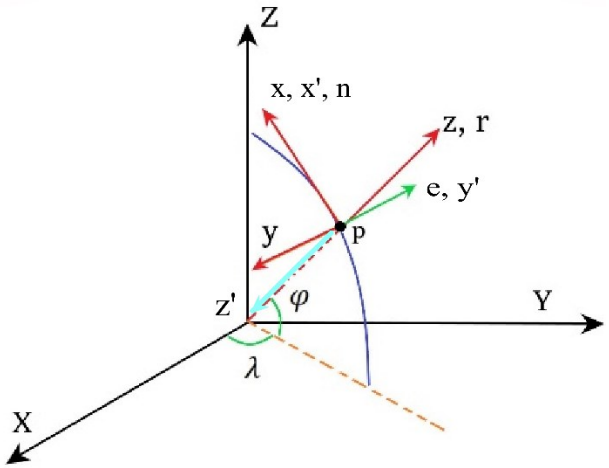

Figure 3.1: Representation of various coordinates systems and their inter-relationships. (*X, Y, Z*) geocentric rectangular coordinate system. (*r, φ, λ*) spherical radius, spherical latitude, and spherical longitude, respectively. (*x, y, z*) local north oriented frame (LNOF) components: *x* (north), *y* (west), *z*

(radially outward from the center of the planet). (x', y', z') with x' pointing to the north, y' east, and z' radially inward to the center of the planet. (*e, n, z*) with *e* pointing to the east, *n* north, and *z* radially outward from the center of the planet.

3.1 Gravity Potential, Gravity Field, and Disturbing Potential

The gravity potential, resulted from the gravitational and centrifugal potential of a rotating planet is [27]:

$$W(r,\varphi,\lambda) = \frac{GM}{r}\sum_{n=n_{min}}^{n_{max}}\left(\frac{R}{r}\right)^n\sum_{m=0}^{n}\left(\overline{C}_{n,m}\cos m\lambda + \overline{S}_{n,m}\sin m\lambda\right)\overline{P}_{n,m}(\sin\varphi) + \frac{1}{2}\omega^2 r^2\cos^2\varphi \quad (1)$$

The gravity vector is:

$$\boldsymbol{g}(r,\varphi,\lambda) = \nabla W(r,\varphi,\lambda) = \begin{pmatrix} g_i \\ g_j \\ g_k \end{pmatrix} \quad (2)$$

where the subscripts *i, j, k* are the orthogonal components of the adopted coordinate system.

The disturbing potential is:

$$T(r,\varphi,\lambda) = \frac{GM}{r}\sum_{n=n_{min}}^{n_{max}}\left(\frac{R}{r}\right)^n\sum_{m=0}^{n}\left(\overline{C}_{n,m}\cos m\lambda + \overline{S}_{n,m}\sin m\lambda\right)\overline{P}_{n,m}(\sin\varphi) \quad (3)$$

And the spherical approximation of the gravity disturbance is:

$$\delta g_{sa}(r,\varphi,\lambda) = -\frac{\partial T(r,\varphi,\lambda)}{\partial r} = \frac{GM}{r^2}\sum_{n=n_{min}}^{n_{max}}\left(\frac{R}{r}\right)^n(n+1)\sum_{m=0}^{n}\left(\Delta\bar{C}_{n,m}\cos m\lambda + \Delta\bar{S}_{n,m}\sin m\lambda\right)\overline{P}_{n,m}(\sin\varphi) \quad (4)$$

where:

$$\Delta\bar{C}_{n,m} = \bar{C}_{n,m} - \bar{C}^{ell}_{n,m}\frac{GM^{ell}}{GM}\left(\frac{a^{ell}}{R}\right)^n$$

$$\Delta\bar{S}_{n,m} = \bar{S}_{n,m} - \bar{S}^{ell}_{n,m}\frac{GM^{ell}}{GM}\left(\frac{a^{ell}}{R}\right)^n = \bar{S}_{n,m}$$

3.2 Calculation of GGT components Through Direct Spatial Derivatives

The GGT is a multichannel dataset represented as a symmetric matrix with five independent components:

$$\boldsymbol{\Gamma} = \nabla(\boldsymbol{\nabla}\mathrm{T}) = \begin{bmatrix} \Gamma_{ii} & \Gamma_{ij} & \Gamma_{ik} \\ \Gamma_{ji} & \Gamma_{jj} & \Gamma_{jk} \\ \Gamma_{ki} & \Gamma_{kj} & \Gamma_{kk} \end{bmatrix} \quad (5)$$

where T is the disturbing potential.

In an LNOF, we have:

$$\boldsymbol{\Gamma} = \nabla(\boldsymbol{\nabla} \mathrm{T}) = \begin{bmatrix} \Gamma_{xx} & \Gamma_{xy} & \Gamma_{xz} \\ \Gamma_{zx} & \Gamma_{yy} & \Gamma_{yz} \\ \Gamma_{zx} & \Gamma_{zy} & \Gamma_{zz} \end{bmatrix} \tag{6}$$

The $\boldsymbol{\Gamma}$ components are:

$$T_{xx}(r,\varphi,\lambda) = \frac{GM}{r^3}\sum_{n=n_{min}}^{n_{max}}\left(\frac{R}{r}\right)^n \sum_{m=-n}^{n} \Delta\overline{C}_{n,m}\, Q_m(\lambda)\left(a_{n,m}\overline{P}_{n,|m|-2}(\sin\varphi) + \left[b_{n,m} - (n+1)(n+2)\right]\overline{P}_{n,|m|}(\sin\varphi) + c_{n,m}\overline{P}_{n,|m|+2}(\sin\varphi)\right) \tag{7}$$

$$T_{xy}(r,\varphi,\lambda) = \frac{GM}{r^3}\sum_{n=0}^{n_{max}}\left(\frac{R}{r}\right)^n \sum_{m=-n}^{n} \Delta\overline{C}_{n,m}\, Q_{-m}(\lambda)\left(d_{n,m}\overline{P}_{n-1,|m|-2}(\sin\varphi) + g_{n,m}\overline{P}_{n-1,|m|}(\sin\varphi) + h_{n,m}\overline{P}_{n-1,|m|+2}(\sin\varphi)\right), m \neq 0 \tag{8}$$

$$T_{xz}(r,\varphi,\lambda) = \frac{GM}{r^3}\sum_{n=n_{min}}^{n_{max}}\left(\frac{R}{r}\right)^n \sum_{m=-n}^{n} \Delta\overline{C}_{n,m}\, Q_m(\lambda)\left(\beta_{n,m}\overline{P}_{n,|m|-1}(\sin\varphi) + \gamma_{n,m}\overline{P}_{n,|m|+1}(\sin\varphi)\right) \tag{9}$$

$$T_{yy}(r,\varphi,\lambda) = -\frac{GM}{r^3}\sum_{n=0}^{n_{max}}\left(\frac{R}{r}\right)^n \sum_{m=-n}^{n} \Delta\overline{C}_{n,m}\, Q_m(\lambda)\left(a_{n,m}\overline{P}_{n,|m|-2}(\sin\varphi) + b_{n,m}\overline{P}_{n,|m|}(\sin\varphi) + c_{n,m}\overline{P}_{n,|m|+2}(\sin\varphi)\right), m \neq 0 \tag{10}$$

$$T_{yz}(r,\varphi,\lambda) = \frac{GM}{r^3}\sum_{n=0}^{n_{max}}\left(\frac{R}{r}\right)^n \sum_{m=-n}^{n} \Delta\overline{C}_{n,m}\, Q_{-m}(\lambda)\left(\mu_{n,m}\overline{P}_{n-1,|m|-1}(\sin\varphi) + \upsilon_{n,m}\overline{P}_{n-1,|m|+1}(\sin\varphi)\right), \quad m \neq 0 \tag{11}$$

$$T_{zz}(r,\varphi,\lambda) = \frac{GM}{r^3}\sum_{n=n_{min}}^{n_{max}}\left(\frac{R}{r}\right)^n (n+1)(n+2)\sum_{m=-n}^{n} \Delta\overline{C}_{n,m}\, Q_m(\lambda)\overline{P}_{n,|m|}(\sin\varphi) \tag{12}$$

where:

$$Q_m(\lambda) = \begin{cases} \cos m\lambda, & m \geq 0 \\ \sin|m|\,\lambda, & m < 0 \end{cases}$$

$$a_{n,m} = 0, |m| = 0{,}1$$

$$a_{n,m} = \frac{\sqrt{1+\delta_{|m|,2}}}{4}\sqrt{n^2-(|m|-1)^2}\sqrt{n+|m|}\sqrt{n-|m|+2}, 2 \leq |m| \leq n$$

$$b_{n,m} = \frac{(n+|m|+1)(n+|m|+2)}{2(|m|+1)}, |m| = 0{,}1$$

$$b_{n,m} = \frac{n^2+m^2+3n+2}{2}, 2 \leq |m| \leq n$$

$$c_{n,m} = \frac{\sqrt{1+\delta_{|m|,0}}}{4}\sqrt{n^2-(|m|+1)^2}\sqrt{n-|m|}\sqrt{n+|m|+2}, |m| = 0{,}1$$

$$c_{n,m} = \frac{1}{4}\sqrt{n^2-(|m|+1)^2}\sqrt{n-|m|}\sqrt{n+|m|+2}, 2 \leq |m| \leq n$$

$$d_{n,m} = 0, |m| = 1$$

$$d_{n,m} = -\frac{m}{4|m|}\sqrt{\frac{2n+1}{2n-1}}\sqrt{1+\delta_{|m|,2}}\sqrt{n^2-(|m|-1)^2}\ \times\sqrt{n+|m|}\sqrt{n+|m|-2}, 2 \le |m| \le n$$

$$g_{n,m} = \frac{m}{4|m|}\sqrt{\frac{2n+1}{2n-1}}\sqrt{n+1}\sqrt{n-1}(n+2), |m| = 1$$

$$g_{n,m} = \frac{m}{2}\sqrt{\frac{2n+1}{2n-1}}\sqrt{n+|m|}\sqrt{n-|m|}, 2 \le |m| \le n$$

$$h_{n,m} = \frac{m}{4|m|}\sqrt{\frac{2n+1}{2n-1}}\sqrt{n-3}\sqrt{n-2}\sqrt{n-1}\sqrt{n+2}, |m| = 1$$

$$h_{n,m} = \frac{m}{4|m|}\sqrt{\frac{2n+1}{2n-1}}\sqrt{n^2-(|m|+1)^2}\sqrt{n-|m|}\sqrt{n-|m|-2}, 2 \le |m| \le n$$

$$\beta_{n,m} = 0, m = 0$$

$$\beta_{n,m} = \frac{n+2}{2}\sqrt{1+\delta_{|m|,1}}\sqrt{n+|m|}\sqrt{n-|m|+1}, 1 \le |m| \le n$$

$$\gamma_{n,m} = -(n+2)\sqrt{\frac{n(n+1)}{2}}, m = 0$$

$$\gamma_{n,m} = -\frac{n+2}{2}\sqrt{n-|m|}\sqrt{n+|m|+1}, 1 \le |m| \le n$$

$$\mu_{n,m} = -\frac{m}{|m|}\left(\frac{n+2}{2}\right)\sqrt{\frac{2n+1}{2n-1}}\sqrt{1+\delta_{|m|,1}}\sqrt{n+|m|}\sqrt{n+|m|-1}$$

$$\nu_{n,m} = -\frac{m}{|m|}\left(\frac{n+2}{2}\right)\sqrt{\frac{2n+1}{2n-1}}\sqrt{n-|m|}\sqrt{n-|m|-1}$$

$$\delta_{p,q} = \begin{cases} 1, & p = q \\ 0, & p \neq q \end{cases}$$

Five independent components exist in equation (6) for two reasons: (1) In a free-source condition, i.e., when the measurement is performed outside the gravitational source, the Laplace equation holds, i.e., $\nabla^2 T = 0$ and $\Gamma_{zz} = -(\Gamma_{xx} + \Gamma_{yy})$; and (2) Γ is symmetric ($\Gamma_{xz} = \Gamma_{zx}$, $\Gamma_{xy} = \Gamma_{yx}$, and $\Gamma_{yz} = \Gamma_{zy}$). In this work, the gravity disturbance and Γ components/invariants are calculated from the disturbing static gravitational potential in terms of spherical harmonics and derived using Graflab software [68].

3.3 Calculation of $\vec{g}$ and GGT Through Fourier domain

There is another way to calculate the gravity field, Marussi tensor components, thereby its invariants. This procedure is particularly useful when the gravity field anomaly at our disposal is the "measured gravity data (g_z)". This parameter could be used for calculating the horizontal components of **g**, i.e., (g_x and g_y). We take advantage of Hilbert transform and Fourier domain, to this purpose. Firstly, from g_z, the horizontal components of **g** (g_x and g_y) are calculated. Then, the first derivatives of these three components are computed in different directions. The horizontal and vertical derivatives of disturbing potential, *T*, are Hilbert transforming pairs [69]:

$$\begin{cases} \dfrac{\partial T}{\partial z} = \mathcal{H}\ (\nabla_H T) \\ \mathcal{F}\left(\dfrac{\partial T}{\partial z}\right) = -i\ \dfrac{k_x}{|k|}\ \mathcal{F}\left(\dfrac{\partial T}{\partial x}\right) - i\ \dfrac{k_y}{|k|}\ \mathcal{F}\left(\dfrac{\partial T}{\partial y}\right) \end{cases} \tag{13}$$

Using inverse Fourier transformation of equation (13), we have:

$$\begin{cases} g_x = \dfrac{\partial T}{\partial x} = \ \mathcal{F}^{-1}\left(i\ \dfrac{k_x}{|k|}\dfrac{\partial T}{\partial z}\right) \\ g_y = \dfrac{\partial T}{\partial y} = \ \mathcal{F}^{-1}\left(i\ \dfrac{k_y}{|k|}\dfrac{\partial T}{\partial z}\right) \end{cases} \tag{14}$$

And the directional derivatives of **g** are:

$$\Gamma_{mn} = \mathcal{F}^{-1}[ik_m(\mathcal{F}(g_n))] \tag{15}$$

where $\begin{cases} m = x, y, z \\ n = x, y, z \end{cases}$ are the unit vectors in three orthogonal directions in the Cartesian coordinate system.

3.4 Calculation of $\vec{\mathbf{B}}$ and MGT from *TMF*, Through Fourier Transformation

In the same vein as GGT, the MGT is defined as:

$$\mathbf{MGT} = \begin{bmatrix} \mathrm{B}_{xx} & \mathrm{B}_{xy} & \mathrm{B}_{xz} \\ \mathrm{B}_{zx} & \mathrm{B}_{yy} & \mathrm{B}_{yz} \\ \mathrm{B}_{zx} & \mathrm{B}_{zy} & \mathrm{B}_{zz} \end{bmatrix} \tag{16}$$

The anomalous *TMF* is:

$$TMF = \ \mathbf{B}.\hat{\boldsymbol{f}} = (B_x f_x + B_y f_y + B_z f_z) \tag{17}$$

where $\hat{\boldsymbol{f}}$ is the unit vector in direction of the Earth's magnetic field, and (f_x, f_y, f_z) are its direction cosines. $\mathbf{B} = \boldsymbol{\nabla}\mathrm{U} = \ (B_x, B_y, B_z)$ is the anomalous magnetic vector. U is the magnetic potential.

The only magnetic data at our disposal was *TMF*; to obtain the magnetic aspects (or functionals), i.e., **B** and **MGT** components, we needed to use the Fourier domain, through which the derivation process of the magnetic aspects becomes much more straightforward. Firstly, the vertical component (B_z) of the *TMF* is attained. Then, B_x and B_y are calculated. Afterwards, the components of **MGT** are derived. To do this, we follow the procedure introduced in Blakely (1995)[1].

The relationship between B_z (the vertical component of the anomalous TMF) and TMF in the Fourier domain is:

$$\mathcal{F}(B_z) = \ \mathcal{F}(\psi_z)\ \ \mathcal{F}(\mathrm{TMF}) \tag{18}$$

Where $\mathcal{F}$ is Fourier transform, $\mathcal{F}(\psi_z) = \frac{1}{\theta_f} = \frac{1}{f_z + i\frac{f_x k_x + f_y k_x}{|k|}}$, is the vertical component operator, $\theta_f = f_z + i\frac{f_x k_x + f_y k_x}{|k|}$, is the phase factor of TMF, (k_x, k_y) are wave numbers in $\hat{x}$ and $\hat{y}$ directions, $|k| = \sqrt{{k_x}^2 + {k_y}^2}$, and '$i$' is an imaginary unit.

Considering that we are not in low magnetic latitudes to envisage any instabilities, we can take the inverse Fourier transform from relation (15) to obtain B_z. So, we have:

$$B_z = \mathcal{F}^{-1}\big(\mathcal{F}(\psi_z)\ \ \mathcal{F}(\mathrm{TMF})\big) \tag{19}$$

where $\mathcal{F}^{-1}$ is inverse Fourier transform.

Now from B_z, the horizontal components of **B**, i.e., (B_x and B_y) are calculated. The horizontal and vertical derivatives of magnetic potential, U, are Hilbert transforming pairs [69]:

$$\begin{cases} \dfrac{\partial U}{\partial z} = \mathcal{H}\ (\nabla_H U) \\ \mathcal{F}\left(\dfrac{\partial U}{\partial z}\right) = -i\ \dfrac{k_x}{|k|}\ \mathcal{F}\left(\dfrac{\partial U}{\partial x}\right) - i\ \dfrac{k_y}{|k|}\ \mathcal{F}\left(\dfrac{\partial U}{\partial y}\right) \end{cases} \tag{20}$$

where $\mathcal{H}$ is Hilbert transform operator, and $\nabla_H = \frac{\partial}{\partial x}\hat{x} + \frac{\partial}{\partial y}\hat{y}$

Using inverse of equation (20) we have:

$$\begin{cases} B_x = \dfrac{\partial U}{\partial x} = \ \mathcal{F}^{-1}\left(i\ \dfrac{k_x}{|k|}\dfrac{\partial U}{\partial z}\right) = \mathcal{F}^{-1}\left(i\ \dfrac{k_x}{|k|}B_z\right) \\ B_y = \dfrac{\partial U}{\partial y} = \ \mathcal{F}^{-1}\left(i\ \dfrac{k_y}{|k|}\dfrac{\partial U}{\partial z}\right) = \mathcal{F}^{-1}\left(i\ \dfrac{k_y}{|k|}B_z\right) \end{cases} \tag{21}$$

If we take the directional derivatives from B_x, B_y, and B_z, we can compose the MGT:

Following this, the first derivatives of these three components are computed in different directions.

$$B_{hl} = \mathcal{F}^{-1}[\ ik_h\ \left(\mathcal{F}(B_l)\right)\ ] \tag{22}$$

where $\begin{cases} h = x, y, z \\ l = x, y, z \end{cases}$ are the components in three orthogonal directions.

3.5 Reduction to the pole transformation (RTP) Using Fourier Domain:

In the case of a positive gravity anomaly, the peak value occurs over the mass concentration. This is not true for magnetic anomalies when the magnetization and induced field are not vertical. Reduction to the pole transformation (*RTP*) gives us the magnetic anomaly data as if it lied in the magnetic pole, thereby the horizontal coordinates of the maximum signal coincide with the horizontal location of the magnetic body.

The relation between Fourier transforms of *RTP* field and the field in any other place on the Earth is [1]:

$$\mathcal{F}(RTP) = \ \mathcal{F}(\psi_{\mathrm{RTP}})\ \ \mathcal{F}(TMF) \tag{23}$$

where $\mathcal{F}(\psi_{\mathrm{RTP}})$ and $\mathcal{F}(\mathrm{TMF})$ are the Fourier transformation of RTP operator and TMF, respectively.

$$\mathcal{F}(\psi_{\mathrm{RTP}}) = \frac{1}{\theta_m \theta_f} \tag{24}$$

in which $\theta_m = m_z + i\frac{m_x k_x + m_y k_x}{|k|}$ and $\theta_f = f_z + i\frac{f_x k_x + f_y k_x}{|k|}$. θ_m is phase factor of magnetization, m, and θ_f is phase factor of TMF. Taking inverse Fourier transform:

$$RTP = \mathcal{F}^{-1}\left(\mathcal{F}(\psi_{\mathrm{RTP}})\ \ \mathcal{F}(TMF)\right) \quad (25)$$

3.6 Calculation of Upward and Downward Continuations Through Fourier Domain:

The relationship between the continued upward and downward field with the measured field is [1]:

For magnetic field:

$$\mathcal{F}(TMF_{up}) = \mathcal{F}(\psi_{\mathrm{up}})\ \ \mathcal{F}(TMF) \quad (26)$$

$$\mathcal{F}(TMF_{down}) = \mathcal{F}(\psi_{\mathrm{down}})\ \ \mathcal{F}(TMF) \quad (27)$$

Where the subscripts "up" and "down" stand for continued upward and downward field, respectively.

The upward continuation filter in Fourier domain is [1]:

$$\mathcal{F}(\psi_{\mathrm{up}}) = e^{-\Delta z|k|}, \Delta z > 0 \quad (28)$$

And the downward continuation filter is [1]:

$$\mathcal{F}(\psi_{\mathrm{up}}) = e^{\Delta z|k|}, \Delta z > 0 \quad (29)$$

Now, the resulting continued upward or downward field is:

$$TMF_{up\,(down)} = \mathcal{F}^{-1}\left[e^{(\mp)\,\Delta z|k|}\ \mathcal{F}(TMF)\right], \Delta z > 0 \quad (30)$$

Similarly, for the gravity field ($\delta g_{up\,(down)}$):

$$\delta g_{up\,(down)} = \mathcal{F}^{-1}\left[e^{(\mp)\,\Delta z|k|}\ \mathcal{F}(\delta g)\right] \quad (31)$$

3.7 Properties of GGT and MGT components

In LNOF, the GGT and MGT components and their compositions relate to a crustal material-specific density/ magnetization distribution, and have the following properties:

Γ_{zz}, B_{zz} :

These components are the first vertical derivative of the vertical gradient of the gravity potential (Γ_{zz}) and magnetic potential (B_{zz}). Γ_{zz} and B_{zz}, are essentially, high frequency amplifying parameters with a strengthening property of the signals from high frequency/ shallow anomalous structures. They have the strongest signal to noise ratios among all GGT and MGT components [51].

Γ_{xz}, Γ_{yz}:

The horizontal derivatives of the vertical gradient of the gravity potential in $\hat{x}$ and $\hat{y}$ directions ($\frac{\partial g_z}{\partial x}, \frac{\partial g_z}{\partial y}$). Γ_{xz}, Γ_{yz} delineate the edges of the anomalous density structures or contact areas as total horizontal gradient ($gravity - THG = \sqrt{{\Gamma_{xz}}^2 + {\Gamma_{yz}}^2}$, which is invariant about the $\hat{\boldsymbol{z}}$ axis. When the contact dip between contrasting density volumes is vertical, gravity-THG indicates a clear edge

structure, while in the case of gentle slopes, the magnitude of this parameter decreases towards the noise level [51].

B_{xz}, B_{yz}:

The horizontal derivatives of the vertical the vertical component of *TMF* in $\hat{x}$ and $\hat{y}$ directions ($\frac{\partial B_z}{\partial x}, \frac{\partial B_z}{\partial y}$). B_{xz}, B_{yz} delineate the edges of the anomalous magnetic structures or contact areas as magnetic-total horizontal gradient ($magnetic - \mathrm{THG} = \sqrt{\mathrm{B_{xz}}^2 + \mathrm{B_{yz}}^2}$), which is invariant about the $\hat{\boldsymbol{z}}$ axis. When the contact dip between contrasting magnetization is vertical, magnetic-THG indicates a clear edge structure, while in the case of gentle slopes, the magnitude of this parameter decreases towards the noise level [51].

3.8 Gravity and Magnetic-Tilt Angles

In contrast to the components of Marussi tensor and MGT that amplify the shallow signals, tile angle could detect the signals from different depths. It is defined as [39]:

$$gravity - TA = tan^{-1}\left(\frac{\Gamma_{zz}}{\mathrm{gravity-THG}}\right) = tan^{-1}\left(\frac{\Gamma_{zz}}{\sqrt{{\Gamma_{xz}}^2+{\Gamma_{yz}}^2}}\right) \quad (32)$$

$$magnetic - TA = tan^{-1}\left(\frac{\mathrm{B}_{zz}}{\mathrm{magnetic-THG}}\right) = tan^{-1}\left(\frac{\mathrm{B}_{zz}}{\sqrt{{\mathrm{B}_{xz}}^2+{\mathrm{B}_{yz}}^2}}\right) \quad (33)$$

3.9 Gravity and Magnetic-Logistic-Total-Horizontal-Gradients

Logistic Total Horizontal Gradient (LTHG) is a filter to mark the boundaries of geological structures at different depths, where the density/ magnetization properties changes. LTHG is defined as follows [39]:

$$LTHG = \left[1 + exp\left(\frac{\left(\frac{\partial}{\partial z}(THG)\right)}{\sqrt{\left(\frac{\partial}{\partial x}(THG)\right)^2+\left(\frac{\partial}{\partial y}(THG)\right)^2}}\right)\right]^{-\propto} \quad (34)$$

where THG could be either gravity-THG and magnetic-THG, and $2 \leq \propto \leq 10$.

3.10 GGT Invariants

The tensor **Γ** has three invariants I_0, I_1 and I_2, meaning that under any coordinate rotation, their values do not change [13]:

$$I_0 = Trace(\Gamma) = \sum_{i=1}^{3} \Gamma_{ii} = 0 \quad (35)$$

$$I_1 = \frac{1}{2}((Trace\ (\Gamma))^2 - Trace(\Gamma^2)) = \Gamma_{ii}\Gamma_{jj} + \Gamma_{ii}\Gamma_{kk} + \Gamma_{jj}\Gamma_{kk} - {\Gamma_{ij}}^2 - {\Gamma_{jk}}^2 - {\Gamma_{ik}}^2 \quad (36)$$

$$I_2 = det(\Gamma) = \Gamma_{ii}\left(\Gamma_{jj}\Gamma_{kk} - \Gamma_{jk}\Gamma_{kj}\right) + \Gamma_{ij}\left(\Gamma_{jk}\Gamma_{ki} - \Gamma_{ji}\Gamma_{kk}\right) + \Gamma_{ik}\left(\Gamma_{ji}\Gamma_{kj} - \Gamma_{jj}\Gamma_{ki}\right) \quad (37)$$

where *i, j, k* are the components of the coordinates system. Since **Γ** is a symmetric matrix, its eigenvectors and eigenvalues should be perpendicular and real, respectively. From this condition, it follows that[13]:

$$0 \le I = -\frac{(I_2/2)^2}{(I_1/2)^3} \le 1 \qquad (38)$$

This implies that $I_1 < 0$ in any case.

I_1 and I_2 are two high pass filters amplifying the sources near the measurement point (surface) with units of s^{-4} and s^{-6}, respectively. For example, for a point source [13] $I_1 = -3\frac{(Gm)^2}{r^6}$ and $I_2 = -2\frac{(Gm)^3}{r^9}$. Compared with $T_{zz} = \frac{Gm}{r^2}$, the strength of the filters in passing the high frequency signals are $I_2 > I_1 > \Gamma_{zz}$. This means that, increasing the distance, the I_2 weakens the deep anomalous sources faster than I_1, and I_1 faster than Γ_{zz}. The I_1 quantity is different from the other two in that this parameter cannot distinguish the negative sources from the positive ones. In other words, both positive and negative signals are boosted without showing their signs (I_1 is always negative). So, this feature could be regarded as a disadvantage. On the other hand, Γ_{zz} and I_2 maintain the signs of the anomalies. These high pass filters should be treated with caution because they are more susceptible to noise as the power of " r " rises.

I is called a "dimensionality indicator" [5] whose "zero" value shows a pure 2D distributed density, and value approaching "one" signifies a density distributed in 3D. A pure 2D body is a body in which one horizontal dimension goes to physical infinity and becomes much larger than the other horizontal dimension. In a pure 3D mass, the two horizontal dimensions of the body are exactly equal; the vertical dimension could be smaller or larger. It should be noted, however, that although a causative body is 3D, the determinant of GGT (I_2) and I might be zero at some points of the measurement plane. Therefore, the zero value of I for the 2D state is a necessary condition but not sufficient. In other words, a 2D mass has a zero value of I, but a zero value of I does not necessarily mean that the mass is 2D. In contrast, I=1 always signifies 3D state.

There is no distinct criterion for separation between 2 and 3-dimensionality. Some consider I=0.3 [22] and others consider I=0.5 [5] as a threshold for differentiating 2D from 3D bodies. The closer I is to unity, the closer the mass is to a pure 3D body like a sphere. A closer amount to zero could represent 2-dimensionality for cases when the determinant of GGT is zero. Take, for example, a long horizontal cylinder along the x axis (2D) in the LNOF. In such a case, the first row and column of $\mathbf{\Gamma}$ are zero (relation (39)), and $I = I_2 = det(\Gamma) = 0$.

$$\mathbf{\Gamma} = \begin{bmatrix} 0 & 0 & 0 \\ 0 & \mathbf{\Gamma}_{yy} & \mathbf{\Gamma}_{yz} \\ 0 & \mathbf{\Gamma}_{yz} & \mathbf{\Gamma}_{zz} \end{bmatrix} \qquad (39)$$

Note that 3 or 2-dimensionality also depends on the measurement point distance from the underground causative body as well as the grid data points. For instance, an anomalous structure such as the oceanic-continental plate boundary might seem 2D from a far measurement point (for example, at h=50 km from the reference ellipsoid), while it appears 3D if we conduct airborne gravimetry at h=2 km with a grid network of $100\ m \times 100\ m$.

2.12 Strike Alignment (strike direction)

Strike Alignment (SA) is a direction along which the gravitational response of a geological construct is constant. The strike direction could be parallel to the weakness in the configurational structure of rocks and masses, such as fault and schistosity direction, or parallel to fold axis.

Consider the long horizontal cylinder in the previous section. When its alignment does not coincide with the ***i*** axis, the coordinate system should be rotated around the ***k*** axis in such an angle that in a least

square sense, the rotated axis ($\boldsymbol{i''}$) fits the strike direction of the body. This rotation angle yields the strike direction of the body [13]. In the rotated coordinate system (i'', j'', k''):

$$\boldsymbol{\Gamma''} = \begin{bmatrix} \Gamma''_{ii} & \Gamma''_{ij} & \Gamma''_{ik} \\ \Gamma''_{ij} & \Gamma''_{jj} & \Gamma''_{jk} \\ \Gamma''_{ik} & \Gamma''_{jk} & \Gamma''_{kk} \end{bmatrix} \tag{40}$$

To find the strike direction, θ_s, the objective function, $Q = {\Gamma''_{ii}}^2 + {\Gamma''_{ij}}^2 + {\Gamma''_{ik}}^2$, should be minimal with respect to θ_s (modified from Pedersen and Rasmussen, 1990)[13]:

$$\frac{\partial Q}{\partial \theta_s} = \frac{\partial}{\partial \theta_s}[{\Gamma''_{ii}}^2 + {\Gamma''_{ij}}^2 + {\Gamma''_{ik}}^2] = 0$$

$$\theta_s = \frac{1}{2}\left\{tan^{-1}\left(2\,\frac{\Gamma_{ij}(\Gamma_{ii}+\Gamma_{jj})+\Gamma_{ik}\Gamma_{jk}}{{\Gamma_{ii}}^2-{\Gamma_{jj}}^2+{\Gamma_{ik}}^2-{\Gamma_{jk}}^2}\right)\right\} = \frac{1}{2}\left\{tan^{-1}\left(2\,\frac{-\Gamma_{ij}\Gamma_{kk}+\Gamma_{ik}\Gamma_{jk}}{{\Gamma_{ik}}^2-{\Gamma_{jk}}^2+\Gamma_{kk}((\Gamma_{ii}-\Gamma_{jj}))}\right)\right\} \tag{41}$$

Note that θ_s could be computed within a multiple of $\frac{\pi}{2}$, i.e., (…) gives an extreme value for Q. Thus, $Q(\theta_s)\ and\ Q(\theta_s + \frac{\pi}{2})$ at each data point should be calculated, and the minimum value gives the true strike direction, provided that *I* is small. The strike direction could also be derived from the direction of the eigenvectors corresponding to the minimum eigenvalues of the GGT tensor[5]. It is worth mentioning that the intended coordinate system for calculation of SA by Pederesen and Rasmussen (1990) [13] differs from the coordinate system that is utilized in this work. Consequently, equation (…) should be modified with respect to the adopted reference frame. We present the modified form after illustration of the various coordinate systems that are applied to this study.

The gravity vector in (*i, j, k*) coordinates is $\boldsymbol{g} = \begin{pmatrix} g_i \\ g_j \\ g_k \end{pmatrix}$, and its gradient is, $\nabla_{ijk} = \begin{pmatrix} \frac{\partial}{\partial i} \\ \frac{\partial}{\partial j} \\ \frac{\partial}{\partial k} \end{pmatrix}$. Here (*i, j, k*) could be any of (*e, n, z*), (*x, y, z*), (*x', y', z'*) and (*X, Y, Z*) coordinate systems.

$$\Gamma_{ijk} = \nabla_{ijk}\, g^T = \begin{bmatrix} \Gamma_{ii} & \Gamma_{ij} & \Gamma_{ik} \\ \Gamma_{ji} & \Gamma_{jj} & \Gamma_{jk} \\ \Gamma_{ki} & \Gamma_{kj} & \Gamma_{kk} \end{bmatrix} \tag{42}$$

The relationship between the (*enz*) and (*xyz*) coordinate systems is:

$$\mathrm{g}_{enz} = \tau\ \mathrm{g}_{xyz} \tag{43}$$

$$\nabla_{enz} = \tau\ \nabla_{xyz} \tag{44}$$

where τ is a rotational matrix around $\hat{\boldsymbol{z}}$ ($or\ \hat{\boldsymbol{r}}$) as much as $\theta = \frac{\pi}{2}$ [13]:

$$\tau = \begin{bmatrix} \cos(\frac{\pi}{2}) & \sin(\frac{\pi}{2}) & 0 \\ -\sin(\frac{\pi}{2}) & \cos(\frac{\pi}{2}) & 0 \\ 0 & 0 & 1 \end{bmatrix}$$

Similarly, for (*enz*) and (*XYZ*):

$$\mathrm{g}_{XYZ} = \Pi\ \mathrm{g}_{enz} \tag{45}$$

$$\nabla_{XYZ} = \Pi\ \nabla_{enz} \tag{46}$$

where Π is a transformation matrix between (*e, n, z*) and (*X, Y, Z*) [70]:

$$\Pi = \begin{bmatrix} -\sin(\lambda) & -\cos(\frac{\pi}{2}-\varphi)\cos(\lambda) & \sin(\frac{\pi}{2}-\varphi)\cos(\lambda) \\ cos(\lambda) & -\cos(\frac{\pi}{2}-\varphi)\sin(\lambda) & \sin(\frac{\pi}{2}-\varphi)\sin(\lambda) \\ 0 & \sin(\frac{\pi}{2}-\varphi) & \cos(\frac{\pi}{2}-\varphi) \end{bmatrix}$$

From equations (36) and (37):

$$\Gamma_{enz} = \tau \ \Gamma_{xyz} \ \tau^T \quad (47)$$

$$\Gamma_{XYZ} = \Pi \ \Gamma_{enz} \ \tau^T \quad (48)$$

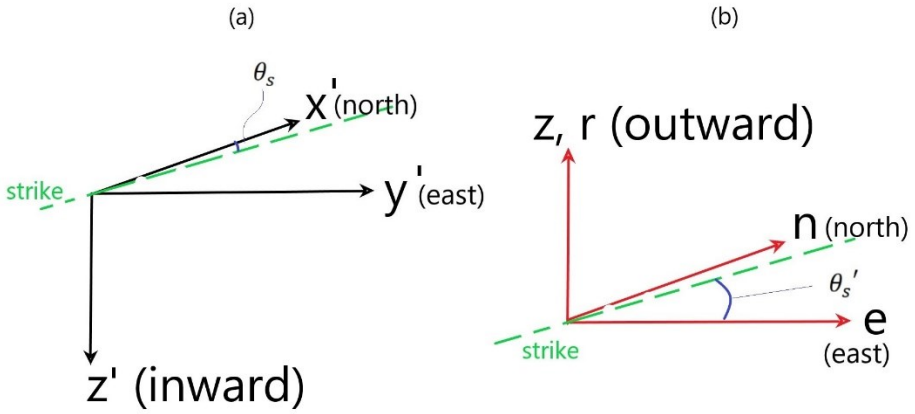

Figure 3.2: Relationships between the coordinate systems in the calculation of strike angles. (a) the coordinate system used by Pedersen and Rasmussen, (b), the coordinate system that we used.

In Pedersen and Rasmussen (1990)[13], the coordinate system is right-handed (figure 3.2a), with **x** pointing to the north, **y** pointing to the east, and **z** pointing downward, and the strike angle is defined as (equation 17 in their paper):

$$\tan(2\theta_s) = 2\,\frac{\Gamma_{x'y'}\left(\Gamma_{x'x'}+\Gamma_{y'y'}\right)+\Gamma_{x'z'}\Gamma_{y'z'}}{{\Gamma_{x'x'}}^2-{\Gamma_{y'y'}}^2+{\Gamma_{x'z'}}^2-{\Gamma_{y'z'}}^2} \quad (49)$$

where θ_s is the strike direction of a 2D structure with respect to the first component of the right-handed coordinate system, **x**'.

The Marussi tensor components in this work are calculated in LNOF[68]. The strike direction could also be computed in any other right-handed coordinate system that is gained from the rotation of LNOF. We worked with (e, n, z), instead of LNOF (see Figure 3.2b).

If the gravity vector in (*x',y',z'*) coordinates is $\boldsymbol{g} = \begin{pmatrix} g_{x'} \\ g_{y'} \\ g_{z'} \end{pmatrix}$ and in (*e, n, z*) is $\mathbf{g} = \begin{pmatrix} g_e \\ g_n \\ g_z \end{pmatrix}$, we can write:

$$g_{enz} = \tau' \ g_{x'y'z'} \quad (50)$$

$$\nabla_{enz} = \tau' \ \nabla_{x'y'z'} \quad (51)$$

$$\mathbf{\Gamma}_{enz} = \ \tau' \ \Gamma_{x'y'z'} \ \tau'^{\,T} \quad (52)$$

Where $\tau' = \begin{bmatrix} 0 & 1 & 0 \\ 1 & 0 & 0 \\ 0 & 0 & -1 \end{bmatrix}$, and

$$\Gamma_{ijk} = \ \nabla_{ijk} \ g_{ijk}{}^{T} = \begin{bmatrix} \Gamma_{ii} & \Gamma_{ij} & \Gamma_{ik} \\ \Gamma_{ji} & \Gamma_{jj} & \Gamma_{jk} \\ \Gamma_{ki} & \Gamma_{kj} & \Gamma_{kk} \end{bmatrix},$$

Where (i, j, k) could be any of (e, n, z) or (x', y', z')

From (52), $\mathbf{\Gamma}_{enz}$ in terms of $\mathbf{\Gamma}_{x'y'z'}$ is:

$$\mathbf{\Gamma}_{enz} = \begin{bmatrix} \Gamma_{ee} = \Gamma_{y'y'} & \Gamma_{en} = \Gamma_{x'y'} & \Gamma_{ez} = -\Gamma_{y'z'} \\ \Gamma_{en} = \Gamma_{x'y'} & \Gamma_{nn} = \Gamma_{x'x'} & \Gamma_{nz} = -\Gamma_{x'z'} \\ \Gamma_{ez} = -\Gamma_{y'z'} & \Gamma_{nz} = -\Gamma_{x'z'} & \Gamma_{zz} = \Gamma_{z'z'} \end{bmatrix} \quad (53)$$

Now, the angle that the strike creates with the east axis ($\theta_s{}'$) is obtained from (Figure 3.2b):

$$\tan(2\theta_s{}') = 2\,\frac{\Gamma_{en}(\Gamma_{ee}+\Gamma_{nn})+\Gamma_{ez}\Gamma_{nz}}{\Gamma_{ee}{}^{2}-\Gamma_{nn}{}^{2}+\Gamma_{ez}{}^{2}-\Gamma_{nz}{}^{2}} = 2\,\frac{\Gamma_{x'y'}\left(\Gamma_{y'y'}+\Gamma_{x'x'}\right)+\left(\left(-\Gamma_{y'z'}\right)\left(-\Gamma_{x'z'}\right)\right)}{\Gamma_{y'y'}{}^{2}-\Gamma_{x'x'}{}^{2}+\Gamma_{y'z'}{}^{2}-\Gamma_{x'z'}{}^{2}} = -\tan(2\theta_s) \quad (54)$$

$\theta_s$is the angle that the strike constructs with the *x'* axis (Figure 3.2a) From (54), it is concluded that:

$$\theta_s{}' = n\frac{\pi}{2} - \theta_s \quad (55)$$

It should be noted here that Pedersen and Rasmussen (1990)[13] worked with θ_s, but we work with $\theta_s{}'$, which is complementary to θ_s.

3.13 Comb Factor

CF [53] is a tool to show how aligned the SA vectors are. In fact, the direction of θ angle at each data point is sketched by a horizontal unit vector. A sliding square window is devised to include 9 (or 25) adjacent data points. The arithmetic-mean of the scalar products between a vector in the center of the window with its 8 (or 24) neighboring vectors is calculated and the result is attributed to that central point. Then the window is slid to encompass the next 9 (or 24)-member array. If the cosine of the angle of two neighboring vectors approaches 1 (~0-degree angle between the unit vectors), alignment is the maximum. In opposite, when the scalar product of these vectors is close to zero, the neighboring vectors are misaligned to maximum degree, close to perpendicular to each other. As a threshold, CF > 0.98 is selected for indicating a good alignment characteristic, and CF < 0.98 is adopted to showing no alignment.

Chapter 4

Distribution of water phase near the poles of the Moon from gravity aspects - Article 1

Distribution of Water Near the Poles of the Moon from Gravity Aspects

Gunther Kletetschka [1, 2*], Jaroslav Klokočník [3], Nicholas Hasson [2, 4] Jan Kostelecký [5, 6], Aleš Bezděk [3, 7], and Kurosh Karimi [1]

[1] Institute of Hydrogeology, Engineering Geology and Applied Geophysics, Faculty of Science, Charles University, Prague 12843, Czech Republic.

[2] Geophysical Institute, University of Alaska - Fairbanks, AK 99709 Fairbanks 903 N Koyukuk Drive, AK, USA

[3] Astronomical Institute, Czech Academy of Sciences, CZ 251 65 Ondřejov, Fričova 298, Czech Republic

[4] Water and Environmental Research Center, Institute of Northern Engineering, University of Alaska Fairbanks - Fairbanks, AK 99775 1764 Tanana Loop AK, USA

[5] Research Institute of Geodesy, Topography and Cartography, CZ 250 66 Zdiby 98, Czech Republic

[6] Faculty of Mining and Geology, VSB-TU Ostrava, CZ 708 33 Ostrava, Czech Republic

[7] Faculty of Civil Engineering, Czech Technical University in Prague, CZ 166 29 Praha 6, Czech Republic

Abstract

Our Moon periodically moves through the magnetic tail of the Earth that contains terrestrial ions of hydrogen and oxygen. A possible density contrast might have been discovered that could be consistent with the presence of water phase of potential terrestrial origin. Using novel gravity aspects (descriptors) derived from harmonic potential coefficients of gravity field of the Moon, we discovered gravity strike angle anomalies that point to water phase locations in the polar regions of the Moon. Our analysis suggests that impact cratering processes were responsible for specific pore space network that were subsequently filled with the water phase filling volumes of permafrost in the lunar subsurface. In this work, we suggest the accumulation of up to ~ 3000 km^3 of terrestrial water phase (Earth's atmospheric escape) now filling the pore spaced regolith, portion of which is distributed along impact zones of the polar regions of the Moon. These unique locations serve as potential resource utilization sites for future landing exploration and habitats (e.g., NASA Artemis Plan objectives).

4.1 Introduction

NASA's return to the lunar surface (i.e. Artemis Plan) requires mission planning for near surface water phase resources [71]. The lunar surface regolith is coupled with ion-magnetohydrodynamical processes that may have contributed to the deposition of water phase on its surface. This is because the lunar environment is exposed for five days of each Earth orbit period to a magnetic field tail extending all the way from the Earth's geomagnetic field [72]. Recent measurements from the Kaguya lunar orbiter (JAXA) have revealed significant numbers of oxygen ions during the time when the lunar orbit was inside the geomagnetic field [72]. This provided the necessary evidence that oxygen ions were not coming from the intrinsic solar winds. This is because the high temperature of the solar corona allows for only multi-charged oxygen ions (O5+, O6+, O7+ and O8+) as observed by Advanced Composition Explorer (ACE) space satellite with O+ in negligible amounts [73]. However, 1–10 keV O+ ions were observed to populate the Moon's environment during the transition through the plasma sheet that originated from the Earth's

ionosphere [72,74]. The terrestrial ion's flux density during the Moon's passage through the magnetotail was estimated between 2.1×10^4 cm^2 s^{-1} and 2.6×10^4 cm^{-2} s^{-1} [72,75].

This process of Earth-lunar geoionic O+ accumulation fluctuated over the history of the earth for several reasons: Initially (1), when the geomagnetic field may have not been well developed or even absent in ancient times the O+ accumulation was more intense. When applying this possibility from the Earth to Mars, where the global magnetic field is absent [47,76], there, an ionospheric plasma sheet develops in absence of the global magnetic field and transfers ion, mostly oxygen, down the plasma sheet as observed by Mars Atmosphere and Volatile Evolution (MAVEN) spacecraft [77]. The second source (2) of ion enhancement has to do with the increasing distance between the Earth and the Moon in their history [78]. The third source (3) of ion variability is an episodical increase of the solar activity observed by MAVEN mission [79]. Evidence of such ion transfer mechanisms [77] supports a hypothesis that a part of the terrestrial atmosphere that was lost in the past is now likely preserved within the surface of lunar polar regolith. For this hypothesis there is a support from observation of nitrogen and noble gases isotopes [80]. The recent advancements in Earth's atmospheric escape warrants new analysis of water phase deposits on the Moon. We apply our novel gravity aspects (descriptors) derived from harmonic potential coefficients of gravity field of the Moon by considering these novel ionic transfer mechanisms on depositional history of water phase formation, from which gravity strike anomalies appear.

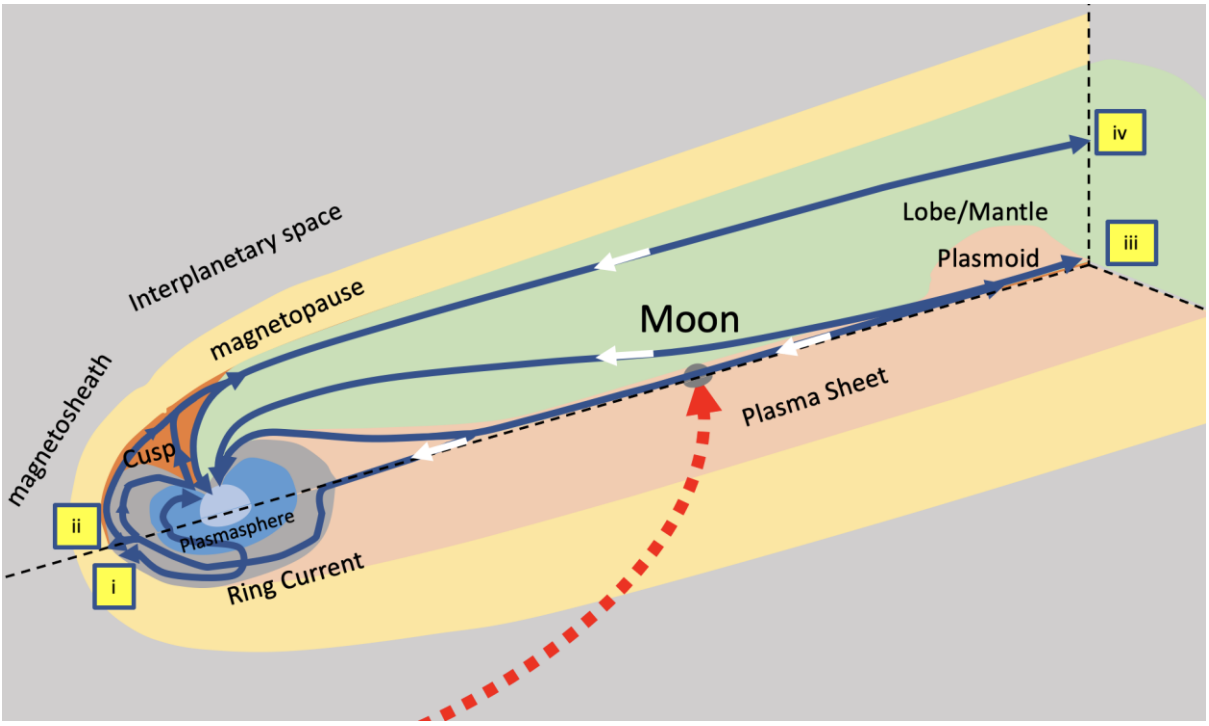

Figure 4.1 Sketch showing three-dimensional cutaway of Earth's magnetosphere. The blue and white arrows are motion pathways of ions (for details see Seki et al.5) illustrating the mechanism for oxygen/hydrogen ions transfer to the Moon. Red dotted line with the arrow shows motion of the Moon into the magnetospheric tail. Escape locations into the interplanetary space is marked by locations i, ii, iii, iv. Image was drown using Microsoft PowerPoint for Mac Version 16.55.

While the loss of the ions from the atmospheres of terrestrial planets depends on processes at the atmosphere-surface interface, there are significant loss mechanisms occurring in the upper atmosphere. For example, the ionosphere's loss of ions due to space plasma acceleration can dynamically control

the evolution of the atmosphere [75]. The geomagnetic field creates an obstacle to the solar wind preventing a direct abrasion of terrestrial neutral ions (oxygens, hydrogens) via thermal and non-thermal activities [81]. Four main pathways of terrestrial ions constitute of (i) magnetopause escape, (ii) magnetopause ring current dayside escape, (iii) anti-sunward flow escape, and (iv) lobe/mantle escape (Fig. 4.1). When ions are escaping via these pathways [75,82,83], they can be returned towards the Earth and be added back to the atmosphere [75]. This occurs when the collision-less path distance becomes small enough that plasma on this length scale dissipates and the geomagnetic field lines and plasma field lines become reconnected [84]. Independently, ion outflow (including mostly H+, O+) from the uppermost terrestrial polar ionosphere has a time dependent typical thermal energies of 0.3 eV [84]. This terrestrial polar wind outflow is on the order of 10^{25} ions s^{-1} during the solar maximum activity, having average flow rates across the solar minimum and maximum of $\sim 5 \times 10^{24}$ ions s^{-1}, caused by electric field disturbance due to charge difference between the ions and faster moving electrons [84]. Prior work has shown, during the dark sky conditions of lunar eclipses, that the differential effects of these energetic H+/O+ ionic species strike the Moon's surface when engulfed by magnetotail transit. This observation suggested that omnipresent exospheric sources are augmented by these variable plasma impact sources in the solar wind reconnection with Earth's magnetotail [85]. There is one order of magnitude difference between the estimates of the polar outflow and the four ion escape routes [75]. Here we consider this unknown loss of ions may account for volume of ions deposited on the Moon.

We note that the solar wind plasma separation of the electrons from the heavy ions is possible when the neutral plasma is obscured by an airless obstacle (asteroids, the whole Moon in this case) [86]. Plasma expands into the void behind the obstacle and creates an electron rich (ion free) volume behind the obstacle [87]. This mechanism was considered for the Lunar dust levitation [88]. The electrons are lighter and therefore they diffuse more efficiently into the shadow behind the Moon while the heavier positive ions continue further distances along the Moon's shadow boundary (an analogy with the electrostatic signature present at permanently shadowed craters [86]. Note that laboratory experiments tried to model electrostatic accumulation due to shadow obstacle processes [89]. They considered shadows as a cause of an electrostatic lofting of the dust on airless bodies, the process that plays role in surface evolution. This may well relate to unexplained observations of dust ponding on asteroids. These dust ponds are accumulation of dust formed in craters on 433 EROS [90–92]. Similar observations were made on comet 67P [93]. Even at Saturn's icy moon Atlas, where the unusually smooth surface may have been modified by electrostatic field. Thus, there must be a distance at which the Moon's electrostatically charged tail may contribute to the reconnection events in the Earth's geomagnetic tail (Fig. S10). Each time when the electrostatically charged tail from the Moon enters the geomagnetic plasma sheet, it may interfere with any ions present in the plasma sheet and modify their trajectories. Such disturbance in particle motion may result in the collision-less path distance of the plasma becoming significantly smaller and this could significantly increase the probability of magnetic flux lines' reconnection.

Earth's atmospheric escape warrants important considerations as potential life support pathways on the Moon [94–96]. We calculate a rough estimation of volumetric water phase that has likely deposited and transformed the Moon's regolith over millennia: during the intersecting 5-day interaction of Earth's magnetosphere with the Moon, if we assume only 1% of the average ion flow per second (5×10^{24} ions s^{-1}) of the O+/water molecules are deposited into the Moon's regolith, this volumetric time transfer equates to 1 million × 24 h × 5 days × 12 months × 5×10^{22} water molecules × 2.7^{-29} m^3/millions of years (MY) is ~ 1 km^3 per MY (This calculation assumed 0.3 nm size of the water molecule, thus 0.027 $nm^3 = 2.7^{-29}$ m^3 water phase volume). If we assume this process occurring from the period of Late Large Bombardment ~ 3.5 billion years (BY) ago, based on the above calculations, we estimate the accumulation of ~ 3500 km^3 of terrestrial water phase, filling the pore spaced regolith, for which novel gravity strike signals would appear. This amount may be two to three fold different, due to smaller Moon-Earth distance in the history [78], but not different by more than order of magnitude. For example, this volume, of ~ 3500 km^3 would be similar to the ~ 5400 km^3 volume of lake Vostok in Antarctica [95].

Ionic flow is orientated both away from and towards the Earth, due to energetic escape processes of Earth's atmosphere. When the Moon enters and is exposed to Earth's ionic plasma sheet, this may capture ions and account for the missing portion of the ionic budget [75]. Impact gardening would then distribute these deposits across the whole Moon's surface. Most primitive basalts from the lunar surface contain considerable amounts of H_2O [97,98]. However, the solar radiation would evaporate the surface deposits and redistribute them towards the polar regions [99]. Larger amounts of such deposits would form a permafrost at the near surface polar regions of the Moon, while filling the pore space of the lunar regolith, and over time, compressing into the liquid phase boundary at depth [100]. Based on the pressure variation with depth on the Moon, we get into 1 atmosphere regolith overpressure at depth of 30 m [101]. The temperature near the Moon's poles is about 100 K and the regolith there has an increasing thermal gradient with depth of about 0.1–0.5 K/m [102]. From this gradient we estimate a depth between 100 and 2000 m, where the pressure and temperature would allow water in pores to exist in liquid state. We have prior experience with detecting subsurface water phase deposits on Earth. For that detection, we used gravity aspects and estimate potential locations of underground deposits of water phase and gas in Sahara Desert regions [36]. Here we apply these methods and locate potential deposits of water phase in the polar regions of the Moon.

4.2 Methodological theory on data

We use a novel method for detecting underground density anomalies via anomalous gravity signal. This method was developed for the study of various geological structures on the Earth: impact craters, subglacial volcanoes, lake basins, paleolakes or petroleum deposition sites globally. Notable, this has also been extended for the impact craters, maria and catenae on the Moon [33]. Typical gravity investigations employ the traditional gravity anomalies or second radial derivatives of the disturbing gravitational potential. This work uses a wider set of functions of the disturbing gravitational potential, we call them "*gravity aspects*". These are derivation operators acting on the *gravity anomalies* Δg, the *Marussi tensor* $(\mathbf{\Gamma})$, the second derivatives of the disturbing potential (T_{ij}), with the second radial component T_{zz}, two of the three *gravity invariants* (I_j), their *specific ratio* (I), the *strike angles* (θ) and the *virtual deformations* (*vd*). Our prior use revealed their diverse sensitivity to the underground density contrasts were due to causative bodies: these are computed to a high degree and order with sufficient numerical stability. It appears that such application extracts a finer and more complete detail of satellite gravity measurements. Theory of this approach was outlined in the book of Klokočník et al. [21]. Further examples and specific application of this method to the Moon is in the Supplementary material.

From Eq. (1) (see Supplementary material) we compute and plot the strike angles θ at the location of interest (here at the Moon's polar regions). Alignment indicates the aligned porosity, filled with contrasting density material (water phase/vacuum). The aligned θ regions suggest water phase deposits.

The first step of this detection method is a transformation: we use the difference in the gravity anomalies between its assumed deepest and shallowest location, then, to the difference in the vertical direction, allowing the maximum estimate where the object can be located, and how large/deep it might be. Several iterations are required to achieve this step. The second step is a use a topography data and the geographic positions of topographical sites, leading eventually to a fine-tuning of the level, extent, and shape of the water phase enriched objects.

4.2.1 Gravity data

The input data here uses harmonic potential coefficients of the spherical harmonic expansion to degree and order d/o of the perturbational gravitational potential (Stokes parameters). A set of these coefficients defines a global static gravitational field. We use the best models available based on satellite records [58,103]. This defines the limits of d/o = 1200 and 1500 for the models GRGM1200A [58] and GL1500E [103] respectively, with practically useful limit d/o = 600 (recommended by the authors of these models themselves). Application of these models allows for the theoretical ground resolution ~ 10 km. The

precision is about 10 mGal. For this paper we chose the GRGM1200A model (after tests concerning degradation of gravity aspects for different harmonic degree, order, and/or appearance of any artifacts).

4.2.2 Surface topography data

These are taken from a new lunar digital elevation model from measurements of the LOLA (Lunar Orbiter Laser Altimeter), an instrument on the payload of Lunar Reconnaissance Orbiter (LRO) spacecraft [60]. The height is given relative to the Moon's reference radius of 1737.4 km. A nominal precision of the LOLA altimeter is ~ 10 cm.

4.3 Results

We computed and plotted the gravity aspects, namely the strike angles θ and the second radial derivatives T_{zz} near the lunar poles—see Fig. 4.2A,B and Supplementary material. In Fig. 4.2A, we used three color modes to express the degree of alignment: yellow and greed as misaligned and red with high degree of alignment. The choice of contrasting alignments (i.e., aligned vs non-alignment), was chosen to be the most conservative, so that only areas with high Comb Factor (CF) values (0.99–1.00) were shown in Fig. 4.2A (see Supplement for CF definition). To demonstrate the robustness, we show more than one way of plotting these strike angle parameters, and represented by CF (Figs. 4.3, and 4.4, and Supplementary material). This shows how we outline areas for smaller alignment of strike angles (CF < 0.97) for each respective hemisphere. Figures S1–S8 show variations of strike angles for both polar regions of the Moon and for ratio $I < 0.3$ (representing 2D-like structures) and $I < 0.9$ (3D-like structures). The calculations resulted in areas of high degree alignment of CF. Hence, we outlined these areas by red vs green and yellow symbols in Fig. 4.2A. Note areas of significant alignment of the strike angles near the north and south poles of the Moon (Fig. 4.2A).

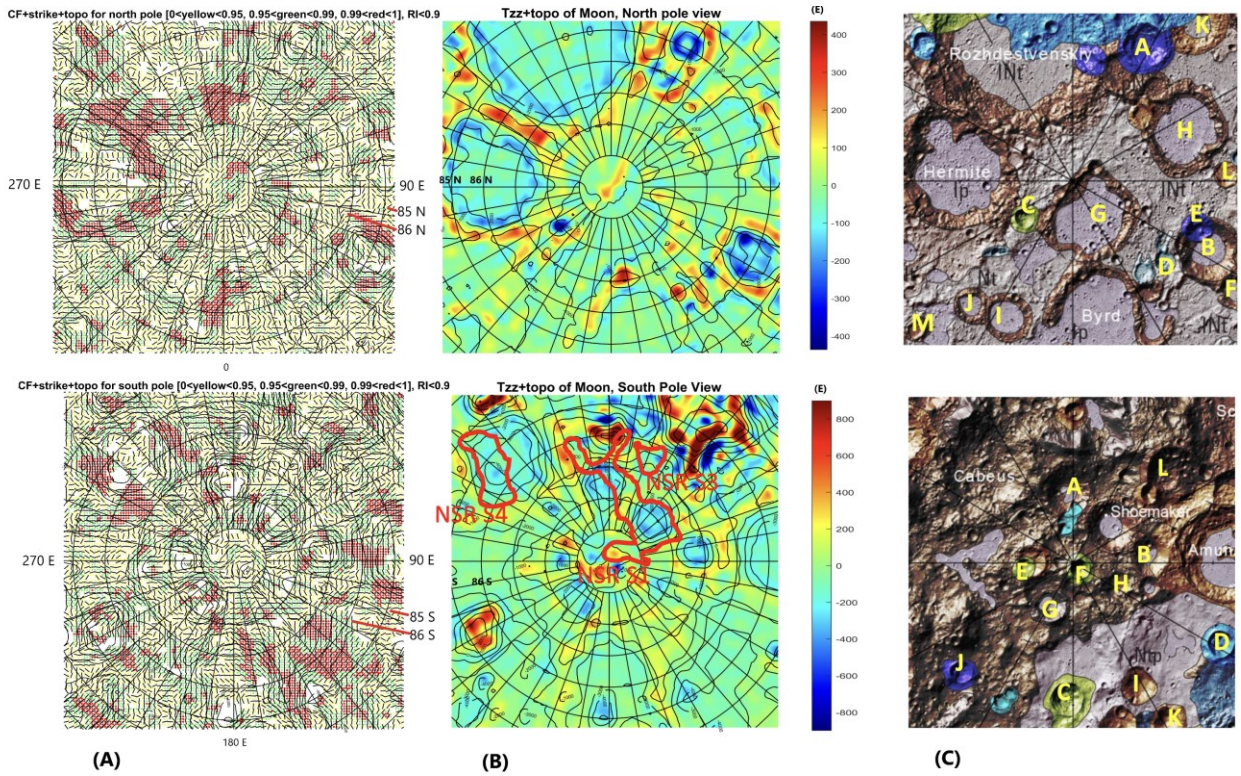

Figure 4.2: Geophysics, topography, and geological subunits of the Moons polar regions.
A. Gravity comb factor (CF) plotted for ratio $I < 0.9$ (see equation (2) and definition of CF in supplementary information). The color legend identifies degree of alignment of strike angles (also Figure 4.3, 4.4); B. Gravity second derivative T_{zz} [E] along with topography [m]. Three areas outlined by red lines and labelled with NSR S1, NSR S3, and NSR S4 are regions identified with a potential

water rich permafrost based on neutron suppression observations[34]; C. Geological map units, where in north pole panel significant craters are labelled by yellow letters as: A-Rozhdestvenskiy U, B-Nansen F, C-Hermite A, D-Porges A, E- Porges B, F-Nansen C, G-Peary, H-Rozhdestvenskiy W, I- Porges C, J- Porges D, K- Porges E, L- Porges F, M-McCoy A, and craters in south pole panel as: A-Haworth, B-Faustini, C-Wiechert J, D-Idel'son L, E-DeGerlache, F-Shackleton, G-Sverdrup, H-Slater, I-Wiechert P, J-Kocher, K-Wiechert U, and L-Nobile. ; Data in plots A. B. were produced by combination of MATLAB, Surfer7.0 and Microsoft PowerPoint. C. is a PowerPoint-modified Unified Geology Map of the Moon[44]

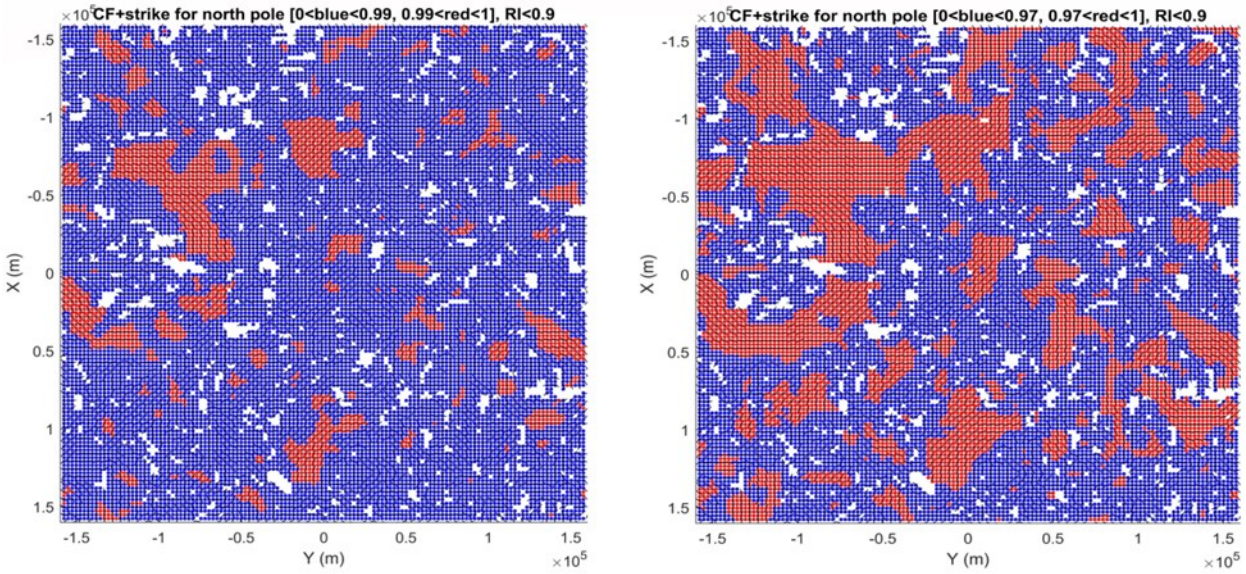

Figure 4.3: Stability of the comb factor (CF) within the area of north pole of the Moon. Dimensions are in meters. A, Left panel corresponds to the strike angle plot and its CF for the north pole in Figure 4.2A. The CF between 0.99 and 1.00 is in red color while the lower CF is in blue color. B. Right panel shows comb between 0.97 and 1.00 in red color while the lower CF is in blue (blue symbol is larger for contrast clarity). Both plots are strike angles for ratio I<0.9 (see equation 2), sensitive to weakness directions of the rocks in subsurface structures near the north pole of the Moon. Data were plotted using MATLAB software.

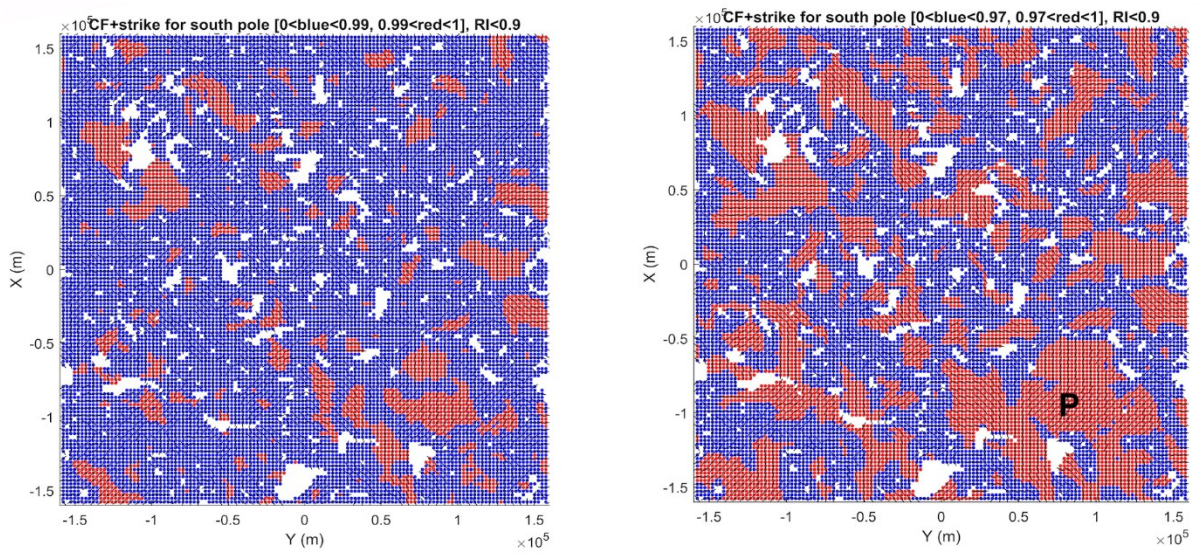

A. B.

Figure 4.4: Stability of the comb factor (CF) within the area of south pole of the Moon. Dimensions are in meters. A. Left panel corresponds to the strike angle plot and its CF for the south pole in Figure 4.2A. The CF between 0.99 and 1.00 is in red color while the lower CF is in blue color. B. Right panel shows comb between 0.97 and 1.00 in red color while the lower CF is in blue (blue symbol is larger for contrast clarity). Black letter P shows significant extent of CF-detected pores in the areas of Aitkin basin. Both plots are strike angles for ratio I<0.9 (see equation 2), sensitive to weakness directions of the rocks in subsurface structures near the north pole of the Moon. Data were plotted using MATLAB software.

Note that Fig. 4.2B shows how the T_{zz}, second derivative of the disturbing gravitational potential distributes near the polar regions of the Moon. The values are spread between − 300 E to 300 E near north pole and from − 600 E to 1100 E near south pole. In the north pole region, the low values are indicative of compressional regime; thus, near surface rocks are denser and spread near the inner ring of the two large impact structures in upper left corner of the Fig. 4.2B (upper north pole panel). Note, the minimum values of T_{zz} reside inside smaller impact craters are expressed both in topographic and the geological unit mapping (Fig. 4.2B,C, upper panel). While we observe these three craters (e.g., Rozhdestvenskiy, Hermite, and Bird), we find these topographic and geological units map to share similarities; the T_{zz} parameter shows that Byrd crater has missing low values within its inner rim structure (see Fig. S9 for delta g). This may relate to a larger difference in *delta g* indicating a variation in compression force inside the craters. The Bird crater is more gravity equilibrated than the Rozhdestvenskiy and Hermile craters. The large topographical relief also seems to generate low values in T_{zz} in other three smaller craters, labeled as A, B., and C. in the north pole geology map. To check the deeper extent of these impact structures we compare T_{zz} with Δg (Fig. 4.2 and Fig. S9) and see much larger contrast in Δg for Rozhdestvenskiy and B craters, followed by Hermite crater. Positive topographic relief shows consistently larger values in Δg value. Similarly, we obtained values for T_{zz} and Δg near the south pole (Fig. 4.2B, lower panel and Fig. S9). Note a larger span of T_{zz} values and association of T_{zz} minima with the interior of impact structures and topographic heights with the positive T_{zz} values (Fig. 4.2B).

4.4 Discussion

The strike angles θ derived in this work show sensitivity to the rock's anisotropy [85–88]. These fractured rocks' weakness and corresponding anisotropy, point to the directions of the strike angle θ and thus towards likely locations of volatile phases accumulations, including water phase. Our results in

Fig. 4.2 shows patchiness of the locations where water phase may have accumulated and this is consistent with the recent molecular water detection by SOFIA [104], where they observed at 6 μm emission feature at high lunar latitudes interpreted as patchy water phase enrichment, and as much as 100–400 μg/g of regolith [104].

The Moon's surface has been significantly modified with impact craters, energetical processes triggering structural extensions during the conversion of high impact kinetic energy into heat. The resulting explosive fractures splinter these regolith rock units and creates topographical indentation, producing a gravitational instability. The rocks in crater vicinity were dominantly compressed in a direction away from the crater center [105]. Such compression creates elongation and fracturing in perpendicular direction (parallel to crater perimeter) [15,106,107]. Many thrust faults are positioned in the subsurface near the perimeter of the crater, due to the impact energy forcing to remove the significant volume material from the inside of the crater [108]. With age, post craters collapse removes or diminish these topographical and gravitational reliefs [109]. The post crater collapse orientation (towards the middle) creates and magnifies the network of faults that are parallel to craters' perimeters [109]. Thus, both impact and post impact processes enhance the anisotropy of rocks along the perimeter of the crater, by forming networks of fault system containing planar weaknesses that include planar pores, oriented along the perimeter direction. On Earth, these pore-spaces (i.e., porosity) often become filled with fluids as water and/or oils. Similarly, we apply the gravity expression of the planar weaknesses of the Moon's impact craters. For this goal we apply a method of gravity detection of the planar network of weaknesses above the preexisting water-filled basins, which has allowed identification of paleolakes on Earth, now arid regions [21,36]. It appears that paleolakes hidden under thick layers in the Great Sand Sea of Western and Southern Egypt generate a special gravity aspect signature that we interpret to be related to the structural anisotropy of the sediment basin. Here we apply the same approach with the hypothesis that the structural weakness of impact craters can be recognized in the gravity aspects. In addition, the gravity aspect, namely the strike angle(s), can determine, where the pore space is likely to be filled with significant amounts of water phase. Once the fractures are filled with water phase, that is more mobile, compared with the host rock system, fractures become subjects of significant pore forces and subsequent anisotropy of the stress field detectable from the gravity potential aspects [32].

The Moons polar regions contain significant amount of water phase [100]. Our estimation (in the Introduction) when considering the forementioned reasonings, allow for theoretical calculations exceeding several thousand cubic kilometers of water phase. Such volume estimates require water phase enclosed in the pore containing rock units in the polar regions, which may cause structural extensions and fracturing. The network of pore fractures surrounding these impact craters is likely to develop due to regular impact crater structural degradation processes [110] and thus would be the most reasonable location for water phase deposits in the polar regions of the Moon. The aligned θ regions tend to be near the impact craters and the angles θ are parallel to craters' perimeters. For example, near the north pole we identified several highly aligned regions along the perimeter of the Rozhdestvenskiy crater and several such areas around the Hermite crater. This is a significant indication, that these two craters contain significant pore space structures that weaken the rock underneath the surface and create gravity strike anomalies. The identified regions of highly aligned strike angles (Fig. 4.2A,B) are thus likely to contain a significant amount of pores-filled water-phase at the subsurface pressure depths, and solid phase near surface (e.g. permafrost).

We observe similar analogies of the aligned strike angle detection of the water phase-filled pore space in rocks near the south pole of the Moon. Our invented Comb Factor (CF) parameter has anomalous values around the crater perimeters (Fig. 4.2A), pinpointing a significant potential for presence of the significant volume of pore space filled with water phase, thus generating anisotropy in the rocks' stress field. The porosity filled with water phase is the structural weakness that is being sensed by strike angle detection near the impact crater boundaries. This is consistent with formation of circular fault systems around the impact craters, where the porosity would form preferentially along the faults formed by impact process [110]. Note, that near the south pole, there is a large region of aligned CF values (labelled

"P" in Fig. 4.4), away from the conspicuously visible major impact craters or topographical relief areas. This "P" region is, however, on the boundary of much larger impact structure, south pole Aitken basin, that significantly modified the early Moon's crust [111], and such mega impact event, may have significantly modified the fracture and related pore space network that could be subsequently filled with the water phase, weakening the rocks modified already by impact even further.

The water phase has been shown to exist in the polar regions of the Moon [104,108,112]. Polar water phase has been proposed to come from the Sun [113]. However, most recently it was shown the oxygen ions entering the Moon's vicinity must source from Earth [114], when exposed to the magnetotail of Earth [72,74,75,85]. Earth's atmospheric escape would provide the supply of the water molecules to the Moon. The hydrogen cations and oxygen anions are free to react with each other, due to their electronegativity differences when they get close. Then, the chemical bonds re-form to make water molecules while an additional energy is released, which propagates the exothermic reaction further. Earth's atmospheric escape effect [82,115] serves as a potential source of unaccounted ions [75] escaping from the Earth into the plasma sheet, and when the Moon passes through this sheet, certain number of oxygen and hydrogen ions is trapped on the Moon. These proposed regions, both in the southern and northern hemispheres, may contain significant subsurface water phase deposits. While these regions were detected from the gravity field aspects, their detection is partially supported from the epithermal neutron emission made from LEND observations onboard LRO, where two out of three Neutron Suppression Regions in this area (NSR S1 and NSR S4) partly overlap with the regions with potentially volumetrically significant water phase detected ([100], e.g., their Figure 5). Detection of porosity through strike angles (Fig. 4.2) would reach depth of tens of kilometers and would not detect porosity distributed only few meters under the surface, whereas the neutron detection is sensitive only to the very top surface of the Moon (0.5 m) and thereby not detect any water in deeper subsurface. Despite this difference in detection depth, it is remarkable that there is an overlap of these two contrasting water phase detection approaches. At this point, our results coupled with those from prior observation of neutrons suppression regions (NSR) both point to the areas with potential volumes of water phased deposits. While NSR locations are not directly tied to the Lunar impact structures, alignments of strike angles clusters near the rims of large craters and this suggests that strike angle alignment analysis is a straightforward way how to detect remotely significant amounts of water phase on planets.

Our gravity aspect method revealed that strike angles are related to T_{zz} gravity aspects, the second derivative of vertical gravity disturbance, and sensitive to gravity signature of craters and faulting. However, we note that the gravity field can also be analyzed for horizontal gravity gradients (Andrews-Hanna et al., 2013) that can detect potential tabular dike features that are hidden under the surface damaged by impact cratering (Andrews-Hanna et al., 2013). This suggests evidence of extensional lithospheric processes at pre-Nectarian to Nectarian age. While our strike angle method was applied in areas very close to the poles (85–90), our vertical T_{zz} gravity aspects was most sensitive to vertical gradients, and we believe our method was not sufficiently sensitive to the linear tabular dikes, for example, detected by (Andrews-Hanna et al., 2013). In addition, the tabular dikes mentioned were mostly distributed further from the poles, where our analysis was restricted to 85°–90° from the poles.

4.5 Conclusion

The origin of the water phase on the Moon has not yet been uniquely identified. In this work, we apply recent observations that part of the Earth's atmosphere may have been transported to the Moon via the novel hydro-magnetospheric-plasma tail and exposing the Moon's surface with terrestrial H_2O. We proposed the Moon's interaction with the geomagnetic tail allows terrestrial ions capture that combine into water molecules and allows water phase deposits on the Moon. Crater impacts, forming structural extensions and fractures, allow suitable pore space networks for hosting large subsurface liquid water reservoirs. Back of envelope calculation suggested several thousands of cubic kilometers of water phase may have accumulated this way into the subsurface of the Moon over the past 3.5 billions of years.

We applied a new method for presenting the gravity aspects signature on the Moon, involving functions derived from gravitational potential, descriptors, and modeling the gravity field. This new method has sensitivity to the structural anisotropy of the Moon's regolith, especially near impact craters. The gravity aspects method detected specific regions near the north and south poles, which point to the likelihood of significant volume of water phase-filled pore space. It seems likely that identified regions in this work hold significant amounts of water phase, suitable for resource utilization plans of future planned missions (Artemis1).

Acknowledgements

GK was partially supported from the Czech Science Foundation 20-08294S, Ministry of Education, Youth and Sports LTAUSA 19141. This work was partly supported from the projects RVO #67985815 and #67985831 (Czech Academy of Sciences, Czech Republic), and the project LO 1506 (PUNTIS) and #LTT18011 from the Ministry of Education of the CR. We thank Dr. F. L. Lemoine (GSFC NASA) for his consultations. The input data—the harmonic potential coefficients (Stokes parameters), magnetic field parameters and surface topography of the Moon are generic. The data to our figures (in surfer program, png files) and our figures with high resolution can be received from J. Kostelecký on request.

Contributions

G.K., N.H. designed, interpreted and wrote the manuscript. J.Kl., J.K., A.B., and K.K. interpreted and provided data for the manuscript.

Corresponding author

Correspondence to Gunther Kletetschka.

Ethics declarations

Competing interests

The authors declare no competing interests.

Additional information

Publisher's note

Springer Nature remains neutral with regard to jurisdictional claims in published maps and institutional affiliations.

3.6 Supplementary Information

Supplementary Information.

Chapter 5

Comparison Between the Geological Features of Venus and Earth Based on Gravity Aspects – Article 2

Comparison Between the Geological Features of Venus and Earth Based on Gravity Aspects

Kurosh Karimi[1*], Gunther Kletetschka[1,2], Verena Meier[1]

[1] Institute of Hydrogeology, Engineering Geology and Applied Geophysics, Faculty of Science, Charles University, Prague 12843, Czech Republic.

[2] Geophysical Institute, University of Alaska - Fairbanks, AK 99709 Fairbanks 903 N Koyukuk Drive, AK, USA

* Corresponding author: Kurosh Karimi (karimik@natur.cuni.cz)

Abstract

We probe the gravitational properties of two neighboring planets, Earth and Venus. To justify a comparison between gravity models of the two planets, spherical harmonic series were considered up to a degree and order of 100. The topography and gravity aspects, including Γ_{zz} (vertical derivative of the vertical component of the gravity field), strike alignment (SA), comb factor (CF), and I_2 invariant derived from the Marussi tensor, were calculated for the two planets at specifically selected zones that provided sufficient resolution. From Γ_{zz} we discovered that the N-NW edge of Lakshmi Planum does not show any subduction-like features. Its Γ_{zz} signature resembles passive continental margins on Earth, like those surrounding the Indian Peninsula. Moreover, according to SA and CF, the Pacific and Philippine-North American Contact Zone on Earth indicates significantly higher level of deformation due to convergent motion of the plates, whereas the deformation level on Venus is significantly smaller and local, when considering an equatorial rifting zone (ERZ) of Venus (between Atla-Beta Regios) as diverging boundaries. The strain mode on the East African Rift system is smaller in comparison with ERZ as its Venusian analog.

The topography-I_2 analysis suggests a complicated nature of the topographic rise on Beta Regio. We show that specific regions in this volcanic rise are in incipient stages of upward motion, with denser mantle material approaching the surface and thinning the crust, whereas some risen districts show molten and less dense underlying crustal materials. Other elevated districts appear to be due to mantle plumes and local volcanic activities with large density of underlying material.

Key Words: Marussi tensor - Γ_{zz} - I_2 invariant - strike alignment - comb factor

5.1 Introduction

The gravity aspects [21,22,32,34] including the gravity disturbance δg, components of the Marussi tensor or gravity gradient tensor (the second directional derivatives of the gravity potential Γ_{ij} and the invariants of the Marussi tensor I_0, I_1, I_2), strike alignment (SA), and comb factor (CF), have been employed for detection of local petroleum, metal, diamond, groundwater[5,8,13,16,50,117,118], and regional exploration of the Earth's crust [22,32,34,35,45]. While models from gravity measurements are gaining increasingly higher resolution, they are being explored for remote derivation of planet's material properties on a global scale not only on Earth but also on other celestial bodies. Each of the gravity aspects has its own special characteristics. The traditional δg (gravity disturbance) is often used to detect the regional isostatic conditions, elastic thickness, and density variations of the crustal materials [49]. The Γ_{zz} component and

I_2 invariant of the Marussi tensor are two parameters, amplifying higher frequency signals. This allows their use for specification of the depth related properties of the shallower density anomalies. The components Γ_{ij} allow detection of the edges of anomalous density structures and contact areas [51]. The possible structural weaknesses, deformational status of the crust and its extent, could be shown through the SA and CF parameters, under special conditions. These special properties are discussed in the paper in relation to specific geological origin. More detailed information and mathematical derivations are presented in the Appendix.

Similarly to the analysis of the gravity field, the magnetic field can also be considered via its magnetic gradient tensor (MGT), its eigenvector properties, eigenvalues, and invariants[11,13,31]. However, the MGT application is not as practical as gravity gradient tensor (GGT), due to the complicated nature of the magnetic field. Despite this complication, the MGT tensor has a high frequency amplifying property, and could be used as a complement to the Marussi tensor in the potential field analysis.

Here we compare the geological features of Venus and Earth based on their gravity aspects. While the masses of Venus and Earth are similar, the mobility of the Venus surface and its tectonic activity are not well resolved [119]. We want to fill this gap with a comparative analysis of the gravitational anomalies of these two planets in terms of the gravity aspects. Specifically, this work focuses on the gravity aspects of purposely selected areas and examines their geological properties. The gravity aspects were analyzed based on respective gravity field datasets attained from the EIGEN 6C4 (Earth) and Shgi180ua01 (Venus) models.

For Earth, we used the combined gravity field model EIGEN-6C4 [62]. This model was generated with help of satellite gravity data from the entire GOCE mission (November 2009 until October 2013). This model has a maximum spherical degree and order of 2190. EIGEN 6C4 reaches a half wavelength resolution of 5×5 arcmin (approximately 9 km) on the Earth's surface. In this study, however, we purposely degrade this high resolution in order to compare it with the lower resolution achievable for Venus (truncated to a degree and order of 100).

The gravity model of Venus, Shgi180ua01[65], is the latest model gained from the Magellan spacecraft (1997) to an attainable maximum spherical degree and order of about 100, with a half wavelength resolution of ~ 1.8×1.8 degrees (~ 190 km) over the Venus' surface. It is the maximum resolution achievable with the available data at its equator. However, in some regions, the resolution decreases to degrees as low as 40. It is expected that a new gravity model of a consistent higher resolution will be provided by the proposed VERITAS mission to Venus [66].

The initial full resolutions of the Shgi180ua01 and EIGEN 6C4 gravity models are substantially different (~ 108 arcmin versus 5 arc min, respectively). Thus, considering 1.8×1.8 degree grid resolution of Venus (N_{max}=100), EIGEN 6C4 for Earth is degraded to this resolution for the purpose of comparison.

5.1.1 Previous geological and gravitational studies of Venus

The crust of terrestrial planets is one of the key elements for better understanding of dynamic processes on both surface and mantle. It provides a direct indication of the partial melting of the mantle which is crucial to study petrology and geodynamics of a planet.

The Magellan mission to Venus in 1989-1994 provided a global coverage of the planet and could unravel more details relative to previous missions. It revealed that radially symmetrical geological features (coronae) are dispersed over the planet in linear zones. Whether these are locations of mantle upwelling or downwelling was unclear. A detection of long rift zones (thousands of kilometers) connected highlands with their major volcanoes. However, there were no observations of convergent plate boundaries and oceanic spreading on Venus, a planet approximately the same size as the Earth[120].

Shield volcanoes and vast volcanic plains are significant geological features on a global scale, and the composition of Venus' mantle is assumed to be peridotite [121]. Igneous rocks on the Venus' surface are primarily basaltic. Shield volcanoes show shallow slopes, comparable to terrestrial basaltic shields, while Venus' lava plains are analog to extensive flows of basaltic fluid lava. Only some small volcanic constructs could possibly be composed of more silicic lavas [122].

The Magellan mission supported previous findings about the paucity of the impact craters. Their number has been estimated at ~1000 (this figure compares with ~200 terrestrial impact structures). Such a scarcity leads to the estimation of a relatively young average age of ~750 m.y. for the crust on Venus compared to much older surface features on Mars and our Moon [123]. In addition, the homogeneous distribution of the density of impact craters and similar crater degradation characteristics means that geological units are of similar age. Therefore, it was suggested that the surface must have been catastrophically produced in the last hundreds of millions of years, with slight changes since then [119]. It was further found that the craters are randomly distributed across the Venus' surface but are not randomly distributed with respect to geology. Regions of volcanic shields, flow fields, coronae, and rift systems show a lower crater density, which indicates recent or ongoing resurfacing in those areas [124].

The Venus' convective cells have been suggested to be around 600–900 km wide [125]. Its lithospheric and crustal thickness have been estimated differently; from 100 km to 500 km for lithosphere, and from 8 km to 60 km for the crust [126].

The elevated zones on Venus are deemed to be due to either tectonic thickening of the crust above mantle downwelling [127,128], or due to upwelled mantle plumes [129]. One of the elevated zones is western Ishtar Terra, which covers an elliptical area of 1800-2700 km and includes the 3.5-4.5 km high Lakshmi Planum plateau. The plateau is surrounded by the highest folded mountain ranges on Venus with elevations / altitudes of 6-12 km. Due to the presence of mountain belts, its general topographic shape, and the absence of major rift systems, Lakshmi differs from other plateau-like highlands on Venus [130]. Further, with its dimensions and geomorphology, Lakshmi resembles the Tibetan Plateau and Himalaya Mountain complex on Earth [131,132]. The radar image and Bouguer anomaly of Magellan [19,20] indicate thrust faulting, folding, and transcurrent and transpressional shear zones comprising Lakshmi Planum which acts like a rigid craton-like body thrusting into its surroundings.

The massive volcanic highlands on Venus include Beta Regio with a complex geologic history and several volcanic and tectonic stages. It is an elliptically rock-dominated structure [133]. Beta Regio probably formed due to uplifting and shows mantle heterogeneities [134]. The altitude in Beta Regio exceeds 5 km at Theia Mons and 4.7 km on Rhea Mons [133]. The area is cut by the deep Devana Chasma rift valley, formed during a phase of extensional tectonics, and coincides with the N-S axis of the Beta rise [135].

Rift zones in general are widespread over the surface of Venus and are predominantly situated in the equatorial region. They are often associated with large volcanos and lava plains [136]. They were found to intersect all structural and material units except for the youngest lava plains. Two structural facies can be distinguished: rift valleys and graben belts. A close association between dome-shaped rises and rift valleys can be observed. They extend from the top of such rises and are generally associated with volcanic edifices. On the contrary, graben belts, which are more widespread on Venus, occur far from rises and volcanic edifices are absent in their spatial association[137]. However, both types represent zones of extensional tectonics which formed in the late times of the planet's geological history [138]. Cracking of the lithosphere above upwelling mantle diapirs is considered as the likeliest rift-forming mechanism [139].

Another key question concerns the mobility of the Venus' surface and the planet's tectonic activity. Several studies have shown that currently there is no clear evidence of modern plate tectonic activity like on Earth. Harris and Bédard (2014, 2015)[19,20] probed the mechanisms generating shear zones with a stagnant lid mode due to mantle plumes. A recent new scenario is a horizontal traction on the root of

the continents [135–138]. It was found that the active mantle convection upwelling is required for observations made on gravity and topography beneath large volcanic provinces such as the Atla Regio and Beta Regio, as well as the Devana Chasma rift [140,141].

While recent surface motion on Venus is limited, a large degree of lithospheric mobility in the earlier history of Venus is preserved in the planet's geological record. Some indications are the extensive crustal thickening that forms Lakshmi Planum, which implies 2000-3000 km of crustal convergence or even more to explain the mountain belts, as well as the lateral transport and assembly of three distinct tesserae blocks to form the Tellus Regio [142]. Byrne et al., (2021)[143] reported on a recent finding about a globally distributed set of crustal blocks in the lowlands of Venus, showing evidence of rotation and lateral movement relative to each other. They proved that lithospheric stresses are sufficient to drive a brittle failure in the upper crust. This confirms that the interior convective motion is capable of driving deformation at the Venus' surface [143]. Those results provide a concept of the Earth´s mobile-lid tectonics (modern plate tectonics) at the one end, the static stagnant-lid regime like on Mars and Moon at the other end, with being Venus in between. According to Weller and Kiefer (2020)[131] it is even possible that Venus is still in the transition phase from a mobile- to a stagnant-lid regime. This could be an indication that the mobile crustal blocks on Venus are the last remnants of a more global system of mobile plates on Venus.

Using the maximum eigenvalue of the horizontal gravity gradient, Andrews-Hanna (2016)[17] examined the gravity responses of equatorial Chasmata, Artemis Corona, and Ovda Regio.

We focus on the Γ_{zz} signal from both the Eurasian-Indian Contact Zone (EICZ) and the Lakshmi Planum-Akna Montes-Freyja Montes Contact Zone (LAFCZ) in this study. We employ SA and CF to examine the deformational extent over the planets' crust and analyze the potential magma plumes under Beta Regio using the I_2 parameter. The mathematical derivations are included in the Appendix.

5.2 Results

The Γ_{zz} parameter of EICZ is shown in Figure 5.1a with outstanding positive and negative NW-SE strips related to the uplifted northern and underlying southern plates, respectively (reaching more than $\pm$ 15 E at some locations). Γ_{zz} in the passive continental margins surrounding the Indian Peninsula barely reaches -5E. Figure 5.1b indicates Γ_{zz} of LAFCZ in Ishtar Terra on Venus. The positive narrow signal surrounding Lakshmi Planum is related to the mountain range. There is a slight negative Γ_{zz} signal surrounding the moat of the Akna Montes (AM) and Freyja Montes (FM) around Lakshmi Planum. The Γ_{zz} parameter in S and NW moats of FM, and E and W moats of AM is below -4 E. Allowing for the dimensions (elevation > 5 km) of these mountain ranges, their average Γ_{zz} signal is weak (~ 5 E) in comparison with the Himalayan area with an average elevation of more than 5 km and average Γ_{zz} about 10 E.

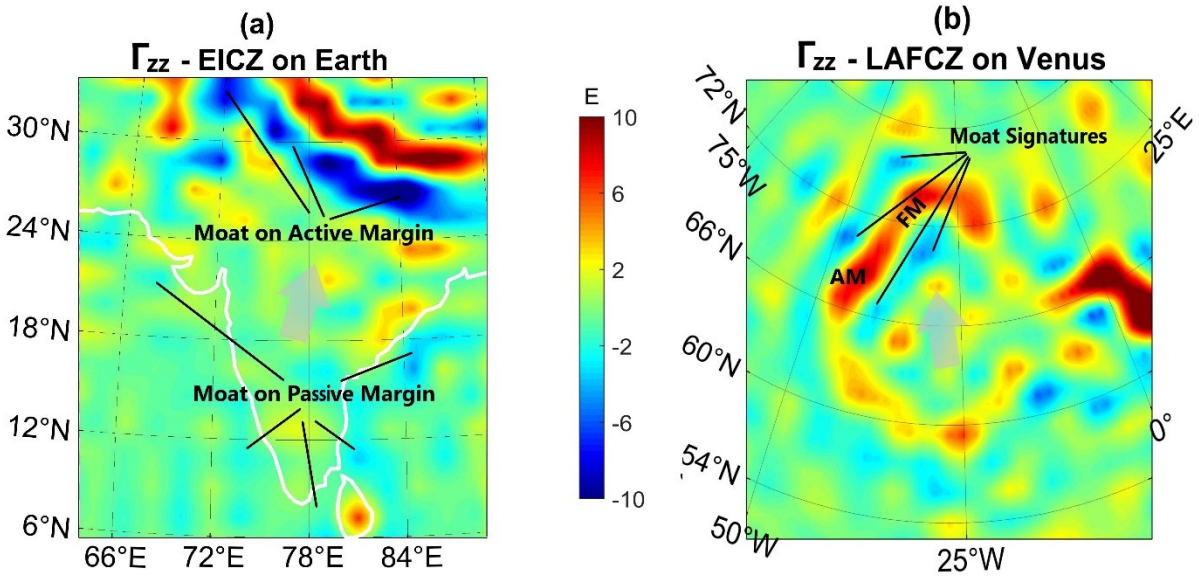

Figure 5.1: Γ_{zz} parameter of a) south of Eurasia and Indian Contact Zone (EICZ). Both positive and negative Γ_{zz} show strong signals and represent the overriding and underthrusting plates in the contact zone, respectively. In contrast, the passive margin of the Indian plate has low signals. b) Lakshmi Planum-Akna Montes-Freyja Montes Contact Zone (LAFCZ) within Ishtar Terra in the northern region of Venus. Γ_{zz} is weak for Akna Montes (AM) and Freyja Montes (FM) and their neighboring moat zone. The gray arrows show how the craton indents into its surroundings. The Γ_{zz} level of the moats around the southern margin of the Indian craton is comparable with the moat on the northern and north-western edge of the Lakshmi Planum.

The SA solution, fitted on the topography map on three sutured regions of the planets, is plotted in Figures 5.2a, 5.2c and 5.2e for $I < 0.5$ ($I < 0.5$ indicates semi-2-dimensional structures [5]). These three zones are Pacific plates and Philippine-North American Contact Zone (PPNCZ) on Earth, the Equatorial Rifting Zone (ERZ) - Hecates, Devana, Fea F, and NW part of Parga Chasmata - between Atla-Beta (AB) Regios on Venus, and the East African Rift (EAR) on Earth. The reason for selection of $I < 0.5$ is that values greater than 0.5 may not depict the true strike alignment of 2-dimensional structures (rift/trench/moat/fold) and their extent (for more information see the Appendix). To sketch the SA at each data point, we drew a small black line pointing to a direction along which the gravity parameter is most stable. This stability indicates the strike of the structures built due to the stresses exerted on the planets. The three areas of the planets are also analyzed in terms of their CF (Figure 5.2b, 5.2d and 5.2f). CF shows the degree of alignment of the SA solutions in and around the planes of faults, folds, and moats. CF lies between 0 and 1. CF=0 applies for the condition with the most non-aligned SA solutions while CF=1 for those perfectly aligned. To see how CF is calculated, refer to the appendix, and also Kletetschka et al. (2022)[53]. The strike directions in the PPNCZ are parallel to a great extent. This alignment coincides with the trenches and neighboring uplifted plates over the volcanic islands and outer rise on both sides. On the planetary scale, SA usually indicates the structural weakness provided that $\Gamma_{zz} < 0$. Of course, the geology of the area under investigation is crucially important in the interpretation of this parameter. SA with $\Gamma_{zz} > 0$ may point to the structural weakness under special conditions, e.g., when intrusive igneous materials fill the faults and fractures of sedimentary layers. The combed zones of the Earth's trenches in the PPNCZ appear to be wide and long (red dots in Figure 5.2b). Red dots indicate high CF values, > 0.98, whereas the blue dots indicate CF < 0.98 (Figures 5.2b, 5.2d and 5.2f). Regarding ERZ on Venus, the parallel SA solutions (CF > 0.98) are limited to small regions. The CF spread is sparser and more limited than the trenching zone on Earth (Figure 5.2c and 5.2d). Aside from the rifting zone, the parallel strike directions and high CF in the right part of Figures 5.2c and 5.2d (longitude = [105° W, 90° W], latitude = [15° N, 40° N]) correspond to the interior valleys

and moats around the western margin of Beta Regio. EAR is shown in terms of SA and CF in Figures 5.2e and 5.2f, respectively. The ovals drawn in these Figures encircle the rifting system. Comparison of the high CF values (red dots) in Figures 5.2d and 5.2f over ERZ and EAR reveals that the rifting system on Venus is wider and sparser.

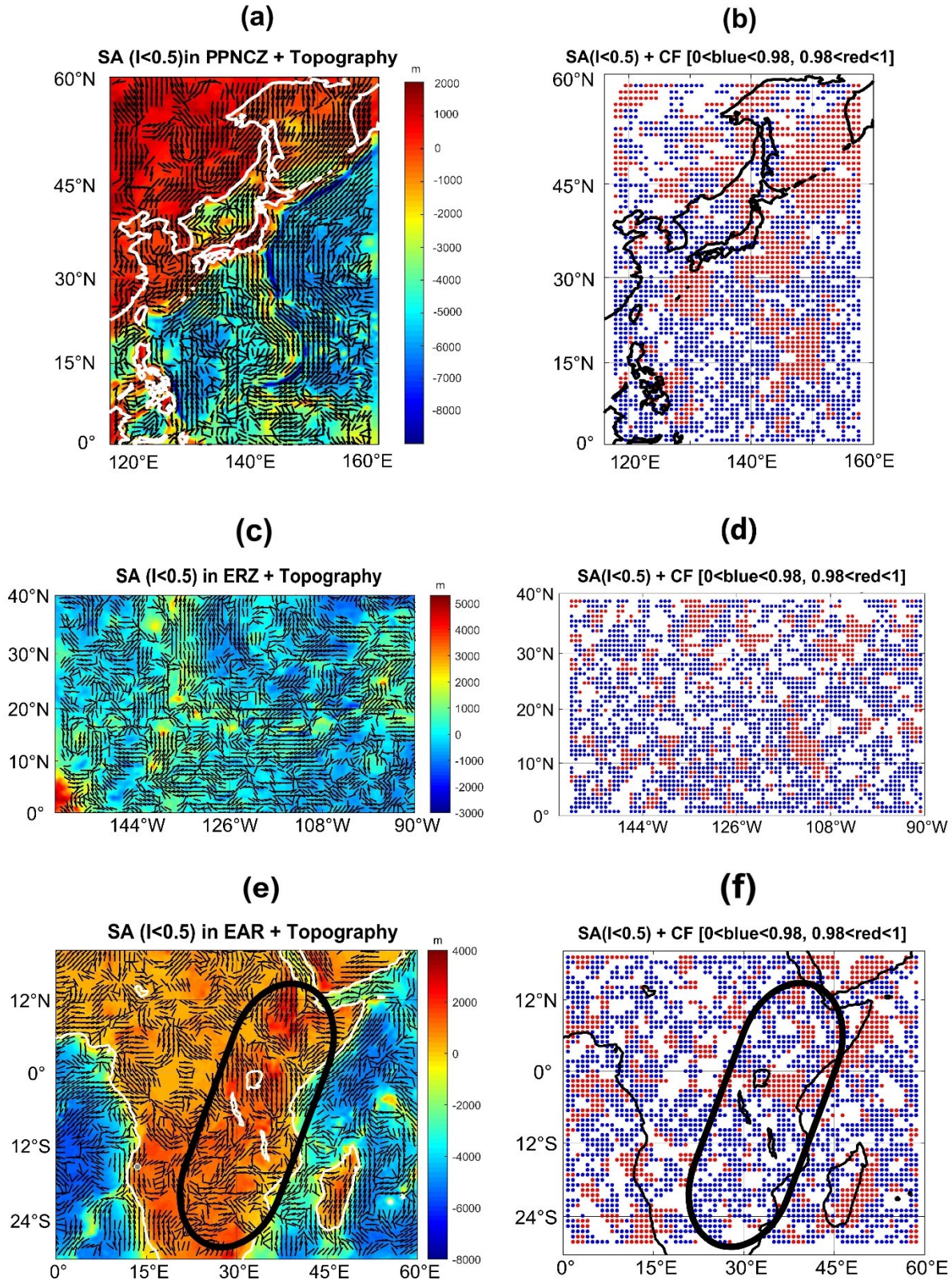

Figure 5.2: Selected zones with strike Alignments (SA) plotted on topography for a) Earth in the Pacific plates and Philippine-North American Contact Zone (PPNCZ); c) Venus in the equatorial rifting zone (ERZ) between Atla-Beta (AB) Regios; e) Earth in East African Rift (EAR). The comb factor (CF) for b) Earth in PPNCZ; d) Venus in ERZ; and f) Earth in EAR. CF is indicative of the strained regions affected by the convergent and divergent stresses. The ovals in (e) and (f) show the East African Rift area. The margins of the continents on Earth are plotted in black or white.

We utilized I_2 parameter to amplify the highest frequency/shallowest signals and inferred the density distributions and variations in Beta Regio on Venus (Figure 5.3). We divided Beta Regio into certain sectors, encircled and labelled as A, B, C, D, E, F, G, H, I, J, K, L, M, N, and P (Figure 5.3). These areas are categorized into 3 groups. In group 1, including B, D, G, northern I, and central J, the I_2 parameter is small (less than 30 S^{-6}) whereas the elevation is high. In group 2 (like A, E, western H, K, western L, M, eastern P and N), the opposite condition holds true, i.e., the I_2 signal is large despite the rather small positive elevation. Group 3 comprises areas where the topography and I_2 correlate well: eastern P, M, central C, western F, eastern H, central I, and the other central and eastern areas of the map with a large I_2 parameter that are not encircled.

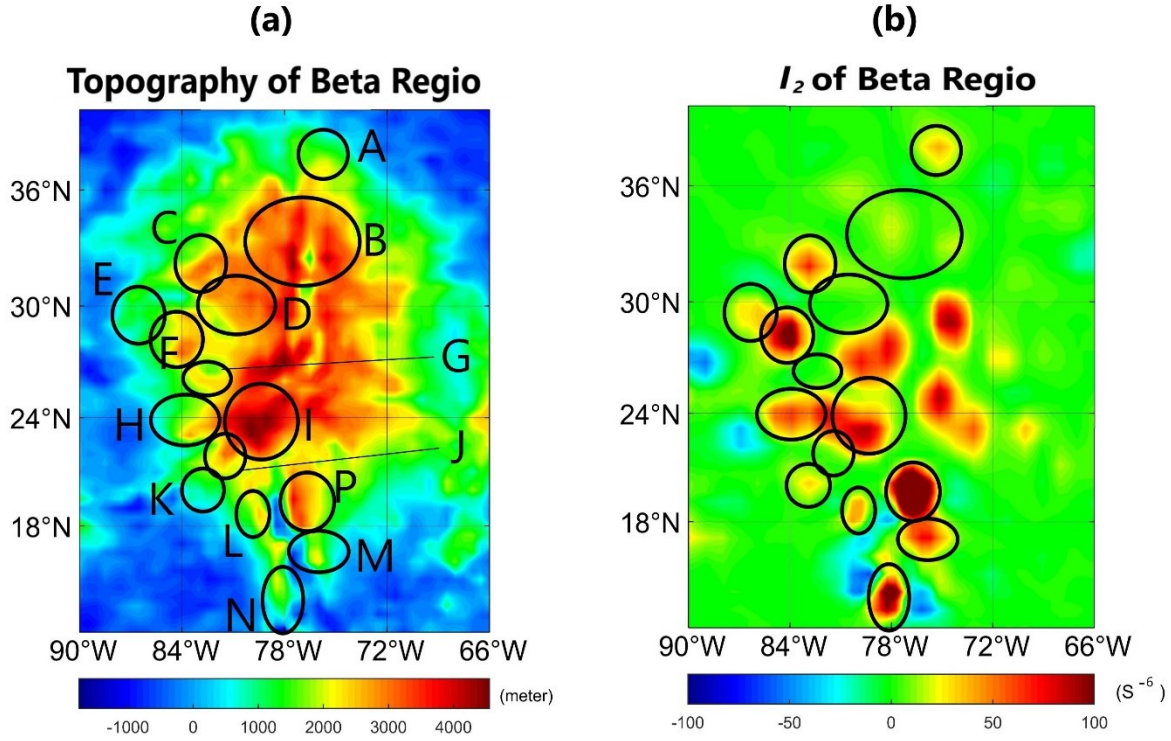

Figure 5.3 a) topography; b) I_2 maps of Beta Regio. The topography and I_2 parameters are not consistent in many areas. Detailed information is in the text.

5.3 Discussion

The Γ_{zz} map of Earth (Figure 5.1a) in EICZ reveals elongated areas of maxima and minima that coincide with plate boundaries, the areas with active orogenesis. This zone is a variation of the subduction process, whereby the subduction zone is destroyed, resulting in an orogenesis where two continental plates are sutured together. Along these stretched patterns, Γ_{zz} indicates subduction of one plate beneath

the other, with $\Gamma_{zz} < 0$ and $\Gamma_{zz} > 0$, respectively. The overriding crust (Himalayas) in this condition has been folded and elevated ($\Gamma_{zz} > 0$)[144]. Generally, the main difference between Γ_{zz} signature of the active and passive boundaries on Earth is that the positive-negative strips over the active boundaries are about an order of magnitude larger than over the passive ones (Figure 5.1a). Another discrepancy is that, in case of destructive borders, island arcs and related volcanism emerge on the overriding plate, increasing the level of gravity and Γ_{zz} thereof. These parameters in the boundaries are also intensely influenced by the existing vertical stresses between the contacting plates, which cause the margins to interact, thereby aggravating the isostatic disequilibrium. This is the case at EICZ, where the Γ_{zz} parameter rises (~ +15 E) and drops (~ -15 E) at the northern and southern edges, respectively (Figure 5.1a). Hence, the intensity of Γ_{zz} can be considered for discrimination between passive and active plate boundaries.

Because of the excessive mass deficiency over the moat basin in EICZ, the gravity is negative. This effect is related to the downward stress caused by the overriding plate which pushes the dense mantle material away. Consequently Γ_{zz}, which is sensitive to these shallow mass variations, has a strong negative signal in this region. As to the depressed zones of the passive margins, this mass deficit is smaller because these troughs are shallower and subsequently filled with low density sedimentary deposits. Moreover, the lithospheric stress is much smaller in these regions and thus the passive margins around the Indian Peninsula are characterized by weaker negative Γ_{zz} (from -2 to -5 E) (Figures 5.1a).

The negative Γ_{zz} anomalous zones on Venus are mainly associated with rift valleys and moats around the mountains. Previous studies on the formation of Lakshmi Planum resulted in two models. The first, divergent model considers Lakshmi to result from mantle upwelling or rather the rising and subsequent collapse of a mantle diapir [145]. The other model explains its formation by mantle downwelling, convergence, under-thrusting and possible subduction, whereby the mountain ranges, the high topography, and the volcanic centers in the middle are considered as key features [146,147]. From the analysis of Γ_{zz} in LAFCZ and EICZ (Figure 5.1), both Lakshmi planum and the Indian Peninsula show similar features. They exhibit low values and smooth variations of Γ_{zz}, indicating much smoother topographic/mass variations with respect to their margins (Figure 5.1). This supports the fact that these two craton-like slabs are probably older than the folded and faulted suture zones embracing them [134]. Nonetheless, there is a fundamental difference. The negative value of Γ_{zz} in the northern and western moats of Lakshmi Planum barely reaches -5 E, which is comparable in magnitude with Γ_{zz} values of passive plate boundaries on Earth like those surrounding Indian craton, not the EICZ (Figure 5.1). Such a weak signal could be related to mild flexure of the crust creating moats on the foothills of FM and AM.

Furthermore, the poorer Γ_{zz} response of FM and AM with respect to Himalayas, despite having more or less the same dimensions, may point to the hypothesis that FM and AM lack the agents that cause larger value of Γ_{zz} over these highlands. These gravity raising factors on Earth are the vertically upward stress from the under-thrusting plate, higher density of the subducting lithosphere with reference to its surrounding mantle, and petrological changes leading to larger density in the subduction zone [3]. Γ_{zz} analyses show no clear evidence for subduction at Lakshmi Planum; the presence of an ancient craton-like tessera massif in the core of Lakshmi is also not consistent with mantle diapir models. Additionally, the absence of a rift system, which is the natural consequence of surface growth due to diapiric rise, the apparent migration of volcanic activities towards its center and the abrupt termination of mountain range ridges at the edge of Lakshmi are contradictory to divergent model predictions, whereas convergence models are consistent with geological and tectonic observations [130]. Those findings strengthen the assumption of a more active tectonic regime with elements of modern plate tectonics in the very beginning of Venus´ geological history when Lakshmi Planum may have formed. Nonetheless, our calculated Γ_{zz} parameters indicate that the indentation of Lakshmi Planum is probably not accompanied with a subduction on the scale of subductions on Earth, and that mechanisms of plate tectonics were significantly restricted, probably not forming a global system like on Earth.

Although we considered Γ_{zz} for some other areas on Venus like the Artemis Corona in the southern part of Ovda Regio, it has not been discussed because of the very low resolution of the gravity model (N< 60) in this area and disruption along the observed satellite track lines.

SA and CF solutions show strain regime variations for two discrepant types of tectonics (convergent plates on Earth and divergent plates on Earth and Venus). The EAR system, the largest rifting system on Earth, is much smaller than those on Venus, and its SA and CF do not reveal a stress-strain regime comparable to those on Venus, on the scale of this study (Figures 5.2c, 5.2d, 5.2e and 5.2f). The SA solution for the PPNCZ on Earth coincides with the trench plane and its neighboring ocean-ward and land-ward linear elevated areas on either side (Figure 5.2a). The wide and large combed area (CF > 0.98) in the proximity of subduction zones in PPNCZ implies that the governing stresses by virtue of converging motions of the plates influence the crust to a very large scale. The resulting strain extends up to hundreds of kilometers from the trench over the volcanic highlands, as well as to the outer rise on the ocean-ward side of the trench. Hence, the SA and CF solutions are used as tools to demonstrate the crustal susceptibility and vulnerability against the exerted stresses (Figures 5.2a and 5.2b). Oppositely, the combed zones on Venus within ERZ (with an opposing tectonic regime) and its proximity are smaller and more variable. This is a characteristic feature of divergent boundaries, where the stresses are much smaller than those on the convergent boundaries. Figure 5.2c shows that SA in ERZ on Venus are shorter and narrower. The zigzag pattern of the SA solution in this area indicates that, unlike the subduction zone on Earth, the stress direction and its spread is more local and variable (Figures 5.2c and 5.2d). SA and CF are even more insignificant for EAR on Earth, implying that the deformational process is weaker throughout the diverging boundaries on Earth than on Venus (Figures 5.2e and 5.2f). Generally, the high CF areas on Earth are in linear and curvilinear arrangements along folded and faulted mountain chains and plate boundaries, while on Venus, large values of CF (> 0.98) surround volcanic constructs in the moats around them in a circular pattern and along the rifted zones, where the crust is thermally uplifted[135].

Topography and I_2 parameters for Beta Regio are plotted in Figures 5.3a and 5.3b, respectively. From I_2 it is possible to detect the shallowest and/or densest anomalies. As I_2 is extracted from the free air gravity parameter, it is highly influenced by topography. Therefore, it is expected to see the largest topographic features in I_2 maps, unless the underlying mass is so small that it counteracts the gravity signal due to the topography. Because of the I_2 nature, the highlands and lowlands should indicate the strongest positive and negative signals, respectively. If the dimensions of individual topographic features are comparable, only under the condition of having different densities, I_2 signatures are different. Thus, for topographic districts with similar dimensions, the higher the density, the stronger the I_2 signal (vice versa in case of low-density areas).

The nature of topography and the complex interrelation of volcanism and tectonism of Beta Regio implies that it was not formed by simple updoming but by a combination of dynamic support of topography together with variations in crustal thickness. The mantle plume model was found to account best for the observed geology in this area [135,148]. Based on the theory of active mantle plumes beneath Beta Regio, we interpreted our results as follows. Group 1 areas show two different phenomena: a rise in topography and partial melting of the lithospheric crust. As the lithosphere is in a molten and hot stage, its density is reduced compared to cold solid lithosphere. This causes the observed pattern of low I_2 signals, i.e., low density, despite the elevated topography. Group 2 areas represent the first stage in the updoming process, in which the mantle starts to rise and gets closer to the surface, thereby causing crustal thinning and density anomalies due to higher densities in mantle material compared to densities of the lithospheric crust; despite that the actual updoming of the area, i.e., a topographic rise, is not yet visible. This relates to the observed low topography but high I_2 signals in respective areas. Areas belonging to group 3 represent zones in which a topographic rise due to ascending high-density mantle plumes is already noticeable. Therefore, both topography and the I_2 signal are high.

Our assumption also perfectly matches the regional distribution of groups 1 to 3 for Beta Regio. The area I comprises the Theia Mons volcano. Its SW part belongs to group 3 and shows a significant rise in altitude due to the underlying mantle plume. In the N part, however, the I_2 signal is low which indicates that hot magma of lower density is present (group 1). The area B (also belonging to group 1) is cut by the Devana Chasma Rift. It was found in previous studies[135,149] that the rift is the result of a hotspot in the northern segment (well visible in the area B) and another hotspot at its southern end in Phoebe Regio. Additionally, Kiefer and Swafford(2006)[149] reported that hot low-density material occurs in the mantle beneath Devana Chasma and the crust is thinned relative to its surrounding areas. This is also visible in our maps in respective areas and consistent with our theory. The area P shows a prominent example of group 3, indicating topographic rise due to the underlying high density mantle material. The area N, on the contrary, perfectly shows the presence of a dense mantle plume which has not yet caused a significant rise in topography. Other areas such as F, H, and K show minor effects of the above stated phenomena in peripheral regions of the mantle plume and volcano.
Geophysical three-dimensional modeling of the lithosphere suggests that the uplift is still active at present day [150], which indicates that plume activity and dome-formation process are still ongoing. The regional plains in the north and the area west of the rise are considered to be unaffected by the plume [135]. This is also consistent with the findings of our study (see Figure 5.3).

5.4 Concluding Remarks

We applied four parameters - Γ_{zz}, strike alignment (SA), comb factor (CF), and I_2, derived from Marussi tensor, to interpret and compare geology of selected zones on Earth and Venus. To make this comparison reasonable, we degraded the resolution of the gravity model of Earth to that of Venus with spherical harmonic degree and order of 100.

The boundaries on the Indian-Eurasian Contact Zone (EICZ) and Lakshmi Planum-Akna Montes-Freyja Montes Contact Zone (LAFCZ) show elongated Γ_{zz} patterns. In these cases, isostatic disequilibrium and petrological changes could be the cause of an elevated Γ_{zz} level in EICZ. On passive margins of the Indian Peninsula, due to lack of these factors, the Γ_{zz} level is low. Comparison between Γ_{zz} of LAFCZ and EICZ indicates that although Lakshmi has been proposed to indent into its northern district, it does not show any overriding-underthrusting behavior, but rather its Γ_{zz} signature resembles that of passive margins around the Indian Peninsula.

SA and CF of destructive margins for Earth and constructive boundaries for Earth and Venus were analyzed to show the level of deformation in the areas inspected. According to these parameters, the Pacific and Philippine-North American contact zone on Earth indicates robust deformation due to a convergent motion of the plates, whereas the strain is quite small and local in the equatorial rifting zone on Venus when considered as constructive margins. The strain-stress regime is even weaker for the East African Rift zone on Earth. This suggests that the deformational process for divergent boundaries on Earth is weaker than on Venus.

The topography-I_2 analysis shows the complicated nature of topographic rise on Beta Regio. According to our study, some regions are in incipient stages of upwelling, where the denser mantle material approaches the surface and thins out the crust, while some uplifted districts have their underlying crustal materials molten and less dense. Finally, some elevated districts with higher density may have been caused by mantle plumes and volcanic activities.

5.5 Availability of Data and Materials

The datasets generated and/or analysed during the present study are available in the [Planetary Data System (PDS)] repository, [https://pds-geosciences.wustl.edu/]. Matlab-based Graflab software was

used for calculation of the Marussi tensor derivatives [68]. I_2, SA and CF were calculated using Matlab programming software.

Acknowledgments: We thank Jeff Andrews Hanna and Jaroslav Klokočník for discussion, and their advice. We also thank Jiri Mizera for his revision, and two anonymous reviewers for their valuable comments on the paper.

Author contributions

K.K. wrote the main manuscript text, processed the data and prepared figures. G.K. wrote the main manuscript text. V.M. wrote the main manuscript text. All authors reviewed the manuscript.

Competing interests

The authors declare no competing interests.

5.6 Additional information

Supplementary Information The online version contains supplementary material available at https://doi.org/ 10.1038/s41598-023-39100-x.

Correspondence and requests for materials should be addressed to K.K.

Reprints and permissions information is available at www.nature.com/reprints.

Publisher's note Springer Nature remains neutral with regard to jurisdictional claims in published maps and institutional affiliations.

Chapter 6

Formation of Australasian tektites from gravity and magnetic indicators – Article 3

Formation of Australasian tektites from gravity and magnetic indicators

Kurosh Karimi[1]*, Gunther Kletetschka[1,2], Jiří Mizera[3,4], Verena Meier[1], Vladimír Strunga[3]

[1] Institute of Hydrogeology, Engineering Geology and Applied Geophysics, Faculty of Science, Charles University in Prague, Albertov 6, 128 43 Praha 2, Czech Republic

[2] Geophysical Institute, University of Alaska - Fairbanks, AK 99709 Fairbanks 903 N Koyukuk Drive, AK, USA

[3] Czech Academy of Sciences, Nuclear Physics Institute, Hlavní 130, 250 68 Husinec-Řež, Czech Republic
[4] Czech Academy of Sciences, Institute of Rock Structure and Mechanics, V Holešovičkách 41, 182 09 Praha 8, Czech Republic

Corresponding author: Kurosh Karimi (karimik@natur.cuni.cz)

Abstract

The parent impact crater of Australasian tektites has not been discovered so far, but a consensus has been accepted on its location in a wider area of Indochina. Recently, an alternative location has been suggested in the Badain Jaran Desert (BJD), Northwest China. Employing gravity and magnetic data derived from satellites, possible presence of an impact structure in BJD is investigated. The gravity parameters include the free air gravity disturbance, its vertical derivative component and total horizontal gradient (THG), strike alignment (SA), and Bouguer anomaly with its first vertical derivative and tilt angle. The magnetic parameters include the anomalous total magnetic field (TMF), its reduced to the pole transformation (RTP), the first vertical derivative of the TMF vertical component (B_{zz}), tilt angle (TA), and logistic total horizontal gradient (LTHG). Both the gravity and magnetic indicators support the presence of the impact structure. Gravity parameters display typical annular gravity highs circumscribing a gravity low. SA analysis reveals preferred parallel directions, implying the susceptibility of special zones to the impact shock waves, both within and beyond the rim. TMF reveals a large magnetic anomaly in the southern part of the proposed crater, and RTP displaces and restricts it further into the rim. B_{zz} weakens the long wavelength anomalies, amplifies the superficial ones, and separates them horizontally. TA and LTHG delineate the deep-seated and shallow magnetic signals related to the peak and border magnetization, respectively.

Key words: Australasian tektites, Badain Jaran Desert, gravity anomaly, total magnetic field, strike alignment

6.1 Introduction

Melting of the target materials from the Earth's surface in an impact of a massive extraterrestrial object can, under conditions not yet clearly understood, lead to formation of natural glasses called "tektites". Classified as distal ejecta, tektites are transported to a strewn field quite distant from a parent impact structure (crater). Four major tektite strewn fields associated with separate impact structures are recognized: Central European (moldavites), Australasian (indochinites, philippinites, australites, etc.), North American (georgiaites and bediasites), and West African - Ivory Coast (ivorites) [151,152]. Recently, Belize impact glass strewn field has been paired with the Pantasma crater in Nicaragua [153], although the final assignment is still questioned [151]. There are several other groups of tektite-like glasses of undoubtedly impact origin, which however miss some characteristic tektite properties, e.g., a sufficient distance from the parent crater [151,152]. While three of the main tektite strewn fields have unequivocally

been paired with their parent impact craters, the largest one, the Australasian tektite strewn field formed at 0.79 Ma and covering up to a sixth of the Earth's surface, is still missing discovery of its parent impact structure. Since the paper by Stauffer [154], the search of a parent crater for Australasian tektites (AAT), has been focused almost solely to Southeast Asia - Indochina, close to the densest occurrence of AAT. The consensus location of the AAT impact in Indochina has been criticized in a series of papers [46,152,155], the most recent one questioning the location at the Bolaven volcanic field in Southern Laos proposed recently by Sieh et al. [156]. The general criticism has particularly been based on the geochemical inconvenience of AAT composition, pointing to low chemical weathering of source materials, with much more weathered sedimentary targets in Indochina. Also, an Indochina impact location misses analogy with other major tektite strewn fields, where the parent craters are never situated inside the strewn field major area.

As an alternative to the criticized consensus location of the AAT impact in Indochina, Mizera et al. [46,152] proposed a more plausible location in the arid area of Northwest China, most probably in the Badain Jaran Desert (BJD; see the map in Fig. 6.1), supported by multiple lines of evidence as follows:

1) Suitability and sufficient supply of pre-impact BJD sediments as an AAT source material, anticipated from close geochemical match between AAT and Chinese loess, and from paleoenvironmental proxies observed in the WEDP02 drill core at the edge of the supposed impact structure. 2) Ideal conditions for crater burial under Holocene sand megadunes, and relatively small ecological consequence of the AAT impact consistent with the oblique impact into a vast desert area surrounded downrange by mountains. 3) Gravity data indicating the existence of anomalous mass within the megadune-lake area in BJD. 4) Specific features of the suggested BJD location possibly attributable to post-impact effects including formation and maintenance of megadunes and lakes, with signs of hydrothermal activity. 5) Presence of possible products of the impactor ablation and other impact-related features in Chinese loess layer recently re-dated to the AAT event. 6) Consistency with principles of distal ejecta ballistic transport, including distribution of various morphological and constitutional AAT types.

Gravity and magnetic anomalies belong to the most apparent geophysical signatures of terrestrial impact structures [15]; see Appendix B in the Supplementary File for more details. Satellite and airborne potential field data serve as useful tools for detecting surface and subsurface large-scale structures on Earth. These datasets have been extensively utilized in numerous studies documented in the literature, showcasing their effectiveness in various applications. For instance, magnetic anomalies associated with the Yallalie impact structure were successfully identified using airborne magnetic data [157]. In a study by Beiki and Pedersen [13], eigenvector analysis of gravity gradient tensor data provided valuable insights into the strike and depth to the anomalous structures in the Vredefort impact structure. Saada et al. [158] utilized satellite potential data to investigate the tectonic features of the Red Sea rift. Furthermore, Pham et al. [37] employed these datasets to detect ridge locations within the Vredefort impact structure. Additional examples include studies by Hamimi et al. [159], who analyzed potential field data to unveil the geological structures of the Nubian Shield, and Urrutia-Fucugauchi et al. [160], who conducted a comprehensive airborne potential field analysis of the Chicxulub impact structure. These studies demonstrate the wide-ranging applications and significance of satellite and airborne potential field data in the detection and characterization of Earth's large-scale structures.

Preliminary inspection of the gravity data in the hypothetical impact area in BJD indicated the existence of a roughly circular structure centered at 39.7°N, 102.2°E, within the area of sand megadunes and lakes [46]. The structure was characterized by a pronounced negative gravity anomaly with a diameter ~50 km, surrounded by a ~100 km rim with a positive gravity anomaly. The observed gravity features were compared with analogous data for the Popigai impact structure, and were consistent with published ground gravity survey data [161]. The present paper continues investigation of the gravity signature of the proposed impact structure in BJD with detailed analysis and interpretation of the free air and Bouguer anomaly functionals both in grid and profile format, and complements it with investigation of magnetic anomaly indicators. The results, interpretation and conclusion presented in this study are not conclusive;

Based on the potential field data, we show that the explored area has the characteristics of an impact structure. However, more investigation is needed to confirm this hypothesis.

6.1.1 Geological setting

The following description has been modified from Mizera et al. [46], and references therein, mainly [162]. BJD, being the second largest desert in China with an area of 49,000 km^2, is situated in the western part of the Alxa Plateau and in the southeastern part of the Badain Jaran Basin in northwest/north-central China, Inner Mongolia Autonomous Region, Gansu province (Fig. 6.1), at an elevation of 900–1500 m a.s.l. Boundaries of BJD are formed by the Mongolian Plateau to the north (N), foothills of Qilian Mts to the south (S), Yabulai (Yabrai) Mts and Zongnai Mts to the east (E), and Bei Mts to the west (W). The Mesozoic and Cenozoic red strata are developed discontinuously in the basin, mainly Cretaceous sandstones and conglomerates, which partially project under the Holocene dune field. The basement is constituted by Proterozoic metamorphic rocks followed by Permian tectonic activity. Several active faults occur south and south-east of BJD – Heli Shan Fault (HLSF), Beida Shan Fault (BSF), Ayouqi Fault (AYQF), and Yabrai Fault (YBF), from W to E (see Fig. 6.4b) – whose Cenozoic tectono-geomorphic evolution may have affected topographic formation and evolution of mountains and deserts of NW China [163]. A detailed geological map of the area can be found online [164], for geological maps and geologic profiles across BJD see also [162,165,166]. The hypothetical AAT impact structure is situated in the SE part of BJD, where up to 480 m high and 3-5 km long sand dunes, interspersed with hypo- to hypersaline and alkaline lakes, are found (Fig. 6.1). BJD belongs to the major source areas of Chinese loess. At the SW edge of the proposed impact area, the Kaxiutata skarn-type iron deposit is located (39.5°N, 101.5°E). The deposit developed near the contact zone between gabbro and Sinian epi-metamorphic rocks. The major mineral is magnetite, minor ones include niccolite, pyrrhotite, safflorite, cobaltite, chalcopyrite, sphalerite, and pyrite [167,168].

Figure 6.1 (a) Satellite image of the Badain Jaran Desert (BJD) and its proximity. The hypothetical crater and its center are marked with a red circle and a cross symbol, respectively. The white rectangle indicates the area analyzed in terms of gravity and magnetic parameters.

6.2 Results

Fig. 6.2a shows the topography of the area comprising the hypothetical crater location (39.7°N, 102.2°E; [46]), shown by a circle and a cross sign in its center. The elevation in the SW of the map is more than 4500 m a.s.l., decreasing to about 1400 m in the middle, and drops to less than 1000 m in the N area. The Beida, Dongda and Yabulai Mts are situated SW, S, and E of the circle, respectively (Fig. 6.1). The topography variation in the profile A_1A_2 (Fig. 6.2a), going through the crater center from S to N, is presented in Fig. 6.3a. The elevation from ~1700 m a.s.l. over the S rim of the hypothetical crater drops to less than ~1300 m on the N rim. The general morphology of the area does not unravel clearly an impact basin. Nevertheless, the gravity parameters indicate a circular pattern with low values in the center and an annular larger value surrounding it. The value in the central zone reaches -100 mGal for δg and -30 E for T_{zz}. These quantities rise from the center in all directions; at the potential crater rim δg averages -40 mGal on the N and E sides and -50 mGal in S. The A_1A_2 profile indicates two δg highs (~ -40 mGal) on the S and N rims and a low (~ -100 mGal) in the center (Fig. 6.3b). Subtraction of the linear regional gravity field (a line in Fig. 6.3b) from δg yields a clearer signature of the residual δg attributed to the shallower layers (Figs. 6.2c, 6.3c). T_{zz}, the vertical derivative of δg, is about zero on average along the rim, with slightly positive values at several locations. The large values of δg and T_{zz}

in the S and SW corner of the map are consistent with the high topography in those areas (Figs. 6.2a, 5.2d). The total horizontal gradient (THG; Fig. 6.2e), sensitive to horizontal variations of the gravity disturbance, demonstrates low values over the crater rim (< 5 mGal m^{-1} on average), and high annular values on the inner flank of the suggested rim. Closer to the crater center, THG is low.

The complete Bouguer anomaly (BA), residual BA, tilt angle (TA), and vertical derivative of BA (g_{zz}) are shown in Figs. 6.2f–i. The average BA values are ~ -95 mGal in W, N, and E parts of the potential rim, and ~ -115 in the S and SW parts. Over the hypothetical cavity, BA decreases to -125 mGal. The long wavelength regional trend of BA slopes from N to S. The A_1A_2 profile on the BA map (Figs. 6.2f, g) is plotted in Fig. 6.3d. To consider a BA signature of the shallower layers, we removed a linear regional field and attained a residual BA (Figs. 6.2g, 6.3e), where the rim coincides with higher values (~10-15 mGal) and the cavity fits a central low (-18 mGal). The TA parameter is consistent with BA, with emphasis on deep and shallow signals. An annular high and a central low are also observed in this parameter (Fig. 6.2h). Fig. 6.2i presents the first vertical derivative of BA (g_{zz}). To remove the very shallow noisy signals and emphasize the crystalline bedrock, the g_{zz} parameter was continued upward (UPC-g_{zz}) to 2 km.

To pinpoint the rim structure according to the UPC-g_{zz} parameter (at h=2 km), we employed the ridge detection theory by Blakely and Simpson [6]. Fig. 6.4a refers to points where g_{zz} peaks within a sliding square window with 9 points. The small white circles, obtained for the solutions with significance values N between 2 and 4, characterize the points over the hypothetical crater rim in the intended area. Although the resolution of the data is not high enough to locate all the faults and fractures in the proximity of the proposed crater, several truncated traces in the g_{zz} map (at h=0) could be observed in Fig. 6.4b. These major fault structures are marked by black rectangles in Fig. 6.4b.

Strike alignment (SA), fitted on topography, for FA and BA types of gravity are plotted in Figs. 6.4c and 4d, respectively. The SA points to the exact elongation of the anomalous mass at each data point, whether it is, for example, the wall of the rim or slump, strike slipping or thrust faulting plane. The overall orientation of SA reveals a roughly circular pattern surrounding the rim for both FA and BA gravity maps. This pattern is a typical response of the crater rim. The SA solutions around the crater are consistent with the lineation of topography and faulted structures. The rose diagrams of the strike angles (calculated with reference to the east axis) are plotted in Figs. 6.4e and 6.4f, restricted to 0°–180°. Each bin in the angular histogram indicates a 4° interval. The strike angles between 120° and 180° are dominant.

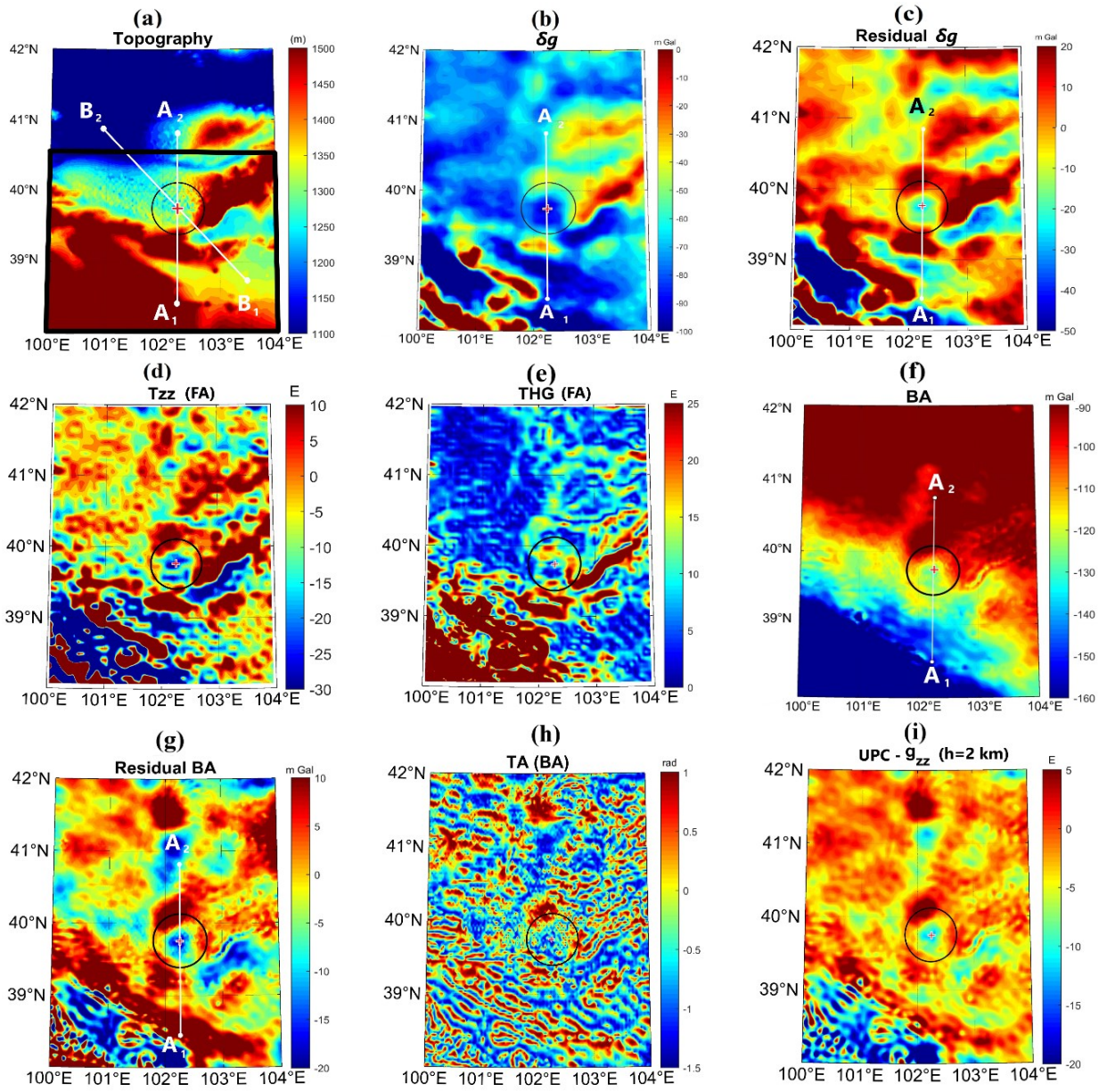

Figure 6.2 (a) Topography. (b) Free air gravity disturbance, δg. (c) Residual δg. (d) Derivative of δg vertical component, T_{zz} . (e) Total horizontal gradient, THG. (f) Bouguer anomaly, BA. (g) Residual BA. (h) Tilt angle, TA. (i) Continued upward vertical derivative of BA, UPC-g_{zz}. Black circle marks the potential crater, the red cross its center. The A_1A_2 and B_1B_2 profiles are used in Fig. 6.3 and Fig. 6.6, respectively. The thick black trapezoid in (a) is the exploration area for strike solutions in Fig. 6.4. The free air (FA) anomalies are shown in (b)-(e), the Bouguer type (BA) anomalies in (f)-(i).

Fig. 6.5 shows the magnetic parameter on a grid, and Fig. 6.6 draws a SE-NW profile (B_1B_2, Figs. 6.2a, 6.5a–c) over the grid map. The magnetic data indicate a significant positive anomaly in the S and SE parts of the intended area. The anomalous total magnetic field (TMF; Figs. 6.5a, 6.6b) reaches its maximum (~300 nT) over the hypothetical S rim. There is a mild linear structure of positive value (~40 nT on average) trending SW-NE to N of the center cross point. In the center, TMF is about -30 nT, stretching parallel to its N and S anomalous neighbors. The magnetic pattern partly coincides with the higher topography in S and SW of the crater, whereas this does not hold for the E, NE, and SE districts of the potential crater. The magnetic highs are typically related to ferromagnetic, (ultra)basic–(ultra)mafic rocks, while the magnetic lows indicate acidic–felsic, and most sedimentary rocks. The black arrow in Figure 6.5a points to the Kaxiutata iron deposit (see the Geological setting). Figs. 6.6a, b

demonstrate the topography and TMF along the B_1B_2 profile from SE to NW crossing the potential crater and perpendicular to the magnetic lineation. TMF magnitude on the SE rim is quite high (~220 nT), but it amounts to weak signal on the NW rim (~30 nT).

Considering the magnetization is entirely induced by the geomagnetic field of the Earth (no remanent magnetization), reduced to pole transformation (RTP) is plotted in Fig. 6.5b, and its B_1B_2 profile in Fig. 6.6c. As observed in these plots, RTP dominant magnetic response is displaced interior to the crater. B_{zz} accentuates the shallow (high frequency) linear sources of magnetic properties (Fig. 6.5c). Fig. 6.6d displays the B_{zz} parameter along the B_1B_2 profile. The magnetic low and highs shown in RTP (Fig. 6.6c) have been amplified in the B_{zz} profile, which differentiates the superficially local anomalies. The TA, derived from THG of B_z, is almost consistent with B_{zz}. It delineates the surface faults and elevated areas. LTHG map (Fig. 6.5e) marks the border of the opposing magnetized rock units. The LTHG linear highs coincide with the edges of most of the faults in the S, SW, and W of the impact area.

6.1 **Discussion**

From the topography map (Fig. 6.2a), it is clear that the S edge of the suspected parent crater (indicated by a circle) is elevated due to the existence of a mountain range. However, the overall terrain does not show a typical morphology of an impact structure. Since δg (Fig. 6.2b) is a free air type quantity and the gravity induced by the buried impact related terrain affects the field value, δg is higher over the rim, and lower over the cavity. The density of material constituting the impact structure and its substrate also affect the magnitude of the field.

The residual δg high in the S, E and NE sides of the rim could be partly due to a higher elevation of the terrain. However, on the N, NW and W, the opposite is true, the topography drops, but the residual δg is still high, implying the existence of denser rocks in these areas. Comparing the topography, δg and residual δg of the A_1A_2 profile (Figs. 6.3a, b, c, respectively) conveys that the large δg value of the S rim may be owing to the Dongda Mts, where the larger mass of the mountains is partly compensated by the regional isostasy. Nonetheless, the flexural rigidity of the crust retains a portion of mass uncompensated whereby causing a higher δg value. The lack of mass due to excavation, existence of allochthonous and autochthonous breccia, fractured materials, and low density aeolian sand in the upper layer could result in a lower δg value within the potential cavity.

Considering that T_{zz} is amplifying higher frequency signals, the shallowest anomalous signals from each data point are amplified while the deeper ones are attenuated. In other words, the extra mass of the rim and the mass deficiency of the cavity, being closest to the measurement level, should be most boosted. On some points over the candidate rim (Fig. 6.2d), T_{zz} is higher, implying that there is an elevated anomalous mass of the rim or uplifted denser bedrock. If the suggested impact crater really exists, according to δg and T_{zz} parameters, its diameter would be ~100–120 km (Figs. 6.2b–d, and shaded area in Figs. 6.3b, c). Both δg and T_{zz} indicate a narrow band of a higher value in the center from W to NE (see Figs. 6.2c, 6.3c). This marginal variation could be due to shallowness of an anomalous mass. If the border of anomalous structure is steep, THG reaches a maximum on the border, with a narrow peak. However, if the margin's dip is gentle, THG grows from a low, reaches a maximum in the middle of the crater's flank with a broader peak value, and drops to a low again. Fig. 6.2e demonstrates a circular THG high inside the cavity, concentric with the rim. This pattern refers to the gentle slope of the inner flank of the crater. As the radius increases or decreases, THG drops, indicating the crest of the rim and flat floor of the cavity, respectively.

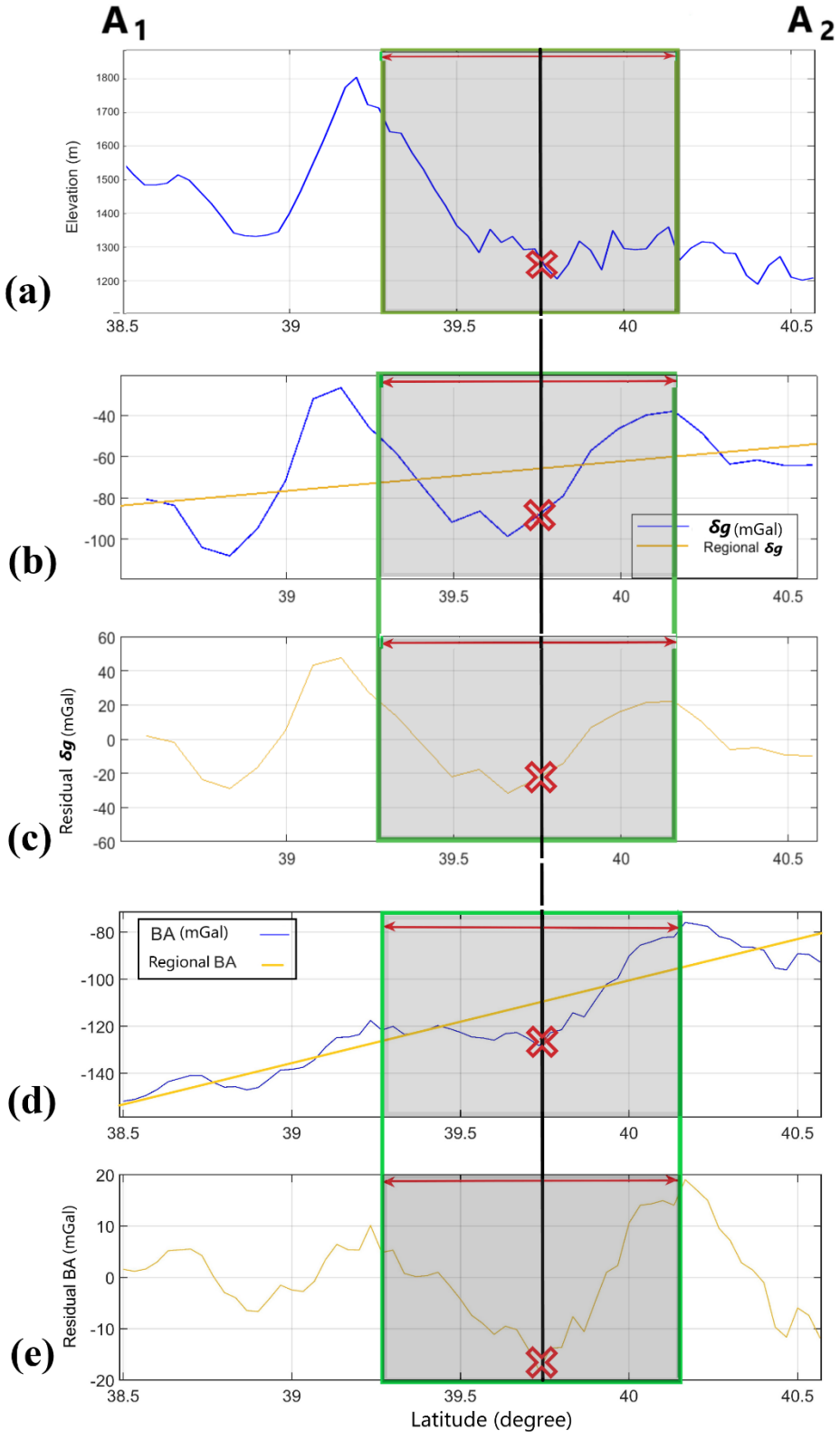

Figure 6.3 The A_1A_2 profile indicated in Fig. 6.2 for: (a) topography; (b) δg.; (c) residual δg; (d) Bouguer anomaly, BA; (e) residual BA. The red cross indicates the proposed crater center and the shaded area the horizontal dimension of the crater in the S-N direction.

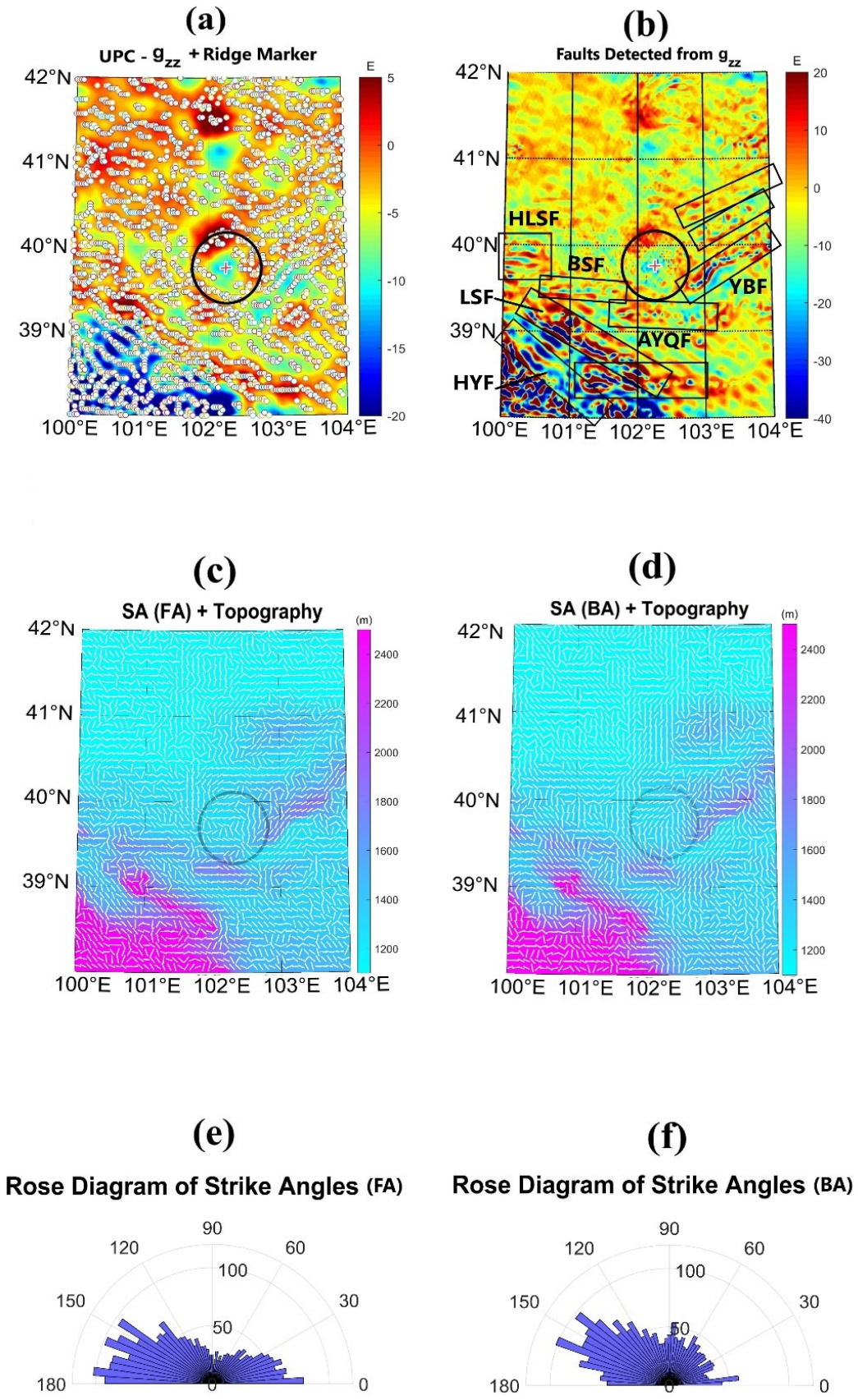

Figure 6.4 (a) Ridge markers (small white circles) fitted on UPC-g_{zz} map (at h=2 km). (b) Detected faults (delineated with black rectangles; HLSF – Heli Shan Fault, BSF – Beida Shan Fault, AYQF – Ayouqi Fault, YBF – Yabrai Fault, LSF – Longshou Shan Fault, HYF – Haiyuan Fault) with truncating

signatures of g_{zz} parameter. (c), (d) Strike alignment (SA) from free air gravity anomaly (FA) and from Bouguer gravity anomaly (BA), respectively. (e), (f) Rose diagram of strike angle distribution between 0° and 180° with respect to the east axis, with bin width of 4° for FA and for BA, respectively.

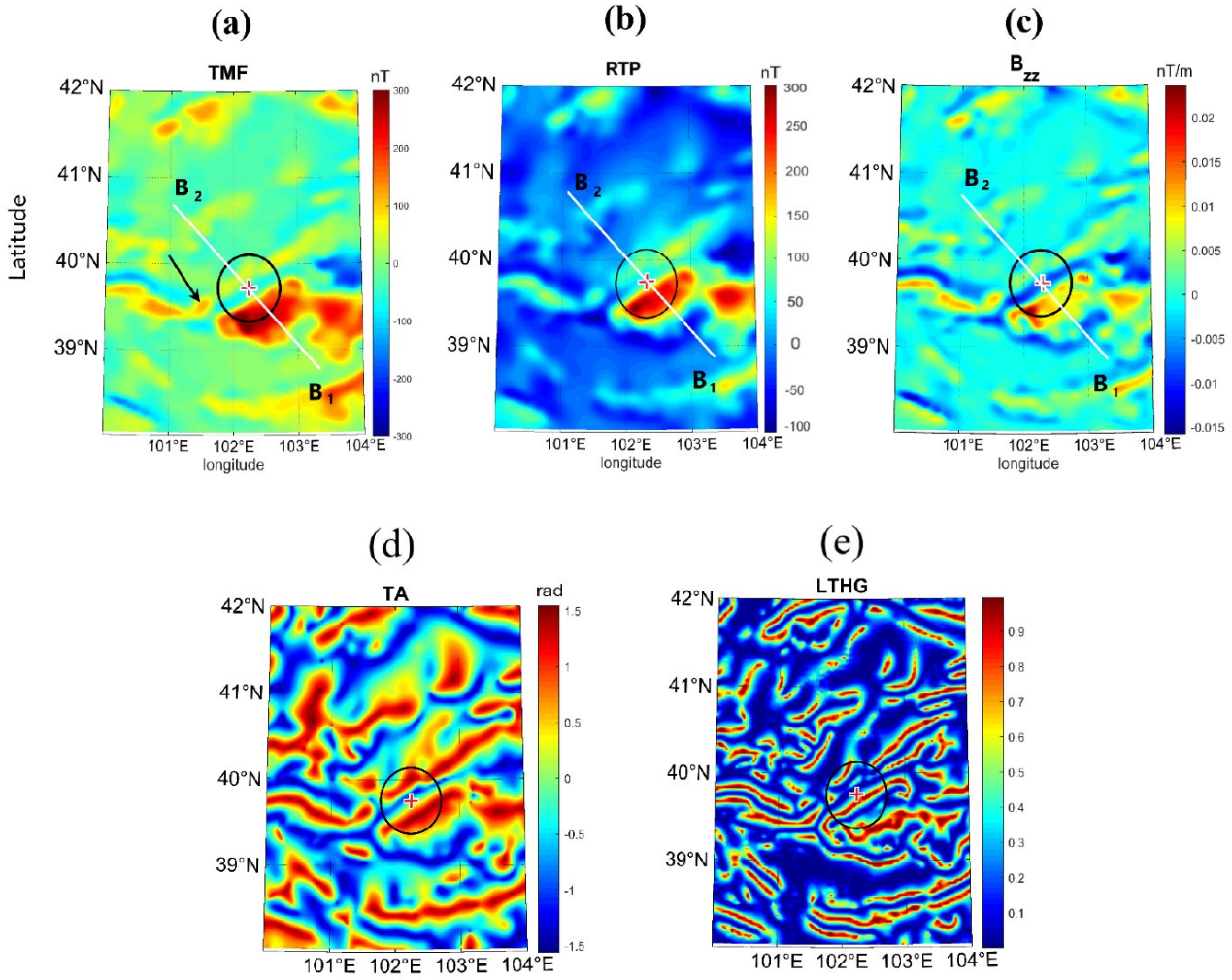

Figure 6.5 (a) Total magnetic field anomaly, TMF. (b) Reduced to pole transformation of TMF, RTP. (c) Vertical derivative of the vertical component of the TMF, B_{zz}. (d) Tilt angle, TA. (e) Logistic total horizontal gradient of B_z, LTHG. Black circle marks the potential crater, and the cross sign indicates its hypothetical center. The black arrow in (a) points to the Kaxiutata iron deposit. B_1B_2 profiles are plotted in Fig. 6.6.

The BA (Fig. 6.2f) is virtually consistent with the general BA pattern of the craters with diameter larger than 30 km, where the difference between the average BA values of the potential cavity and the rim reaches a plateau of -30 mGal [169]. The average difference in our maps is also about -30 mGal. Lower values of BA in the cavity may be due to post-impact sedimentary infillings. Holocene sediments in the basin mainly consist of thick (up to 500 m) layers of low-density sediments with variable proportion of sand and dust, with the majority of sedimentary infilling being made up of coarse aeolian sand. The desert sand is mainly derived from aeolian reworking of the surrounding mountains and marks the onset of the BJD formation at 1100 ka; approx. 300 ka before the impact [162]. Brecciation and fracturing related to the impact can also contribute to the observed low BA values. Conversely, the higher values of BA over the rim are likely caused by the uplifted denser material (the crystalline bedrock). Additionally, the rise in topography related to the onset of the adjacent orogen gets visible towards the S rim. Since the mountains consist of dense rock compared to low-density basin sediments, the rise in BA values

may also be partly related to the location of the crater close to the surrounding mountains on the S rim (Figs. 6.2f, 6.3d, 6.3e). Note that this interpretation is consistent with the results attained from the ground gravimetry by Yang et al. [161] to detect topography of bedrock beneath the sand dunes in BJD.

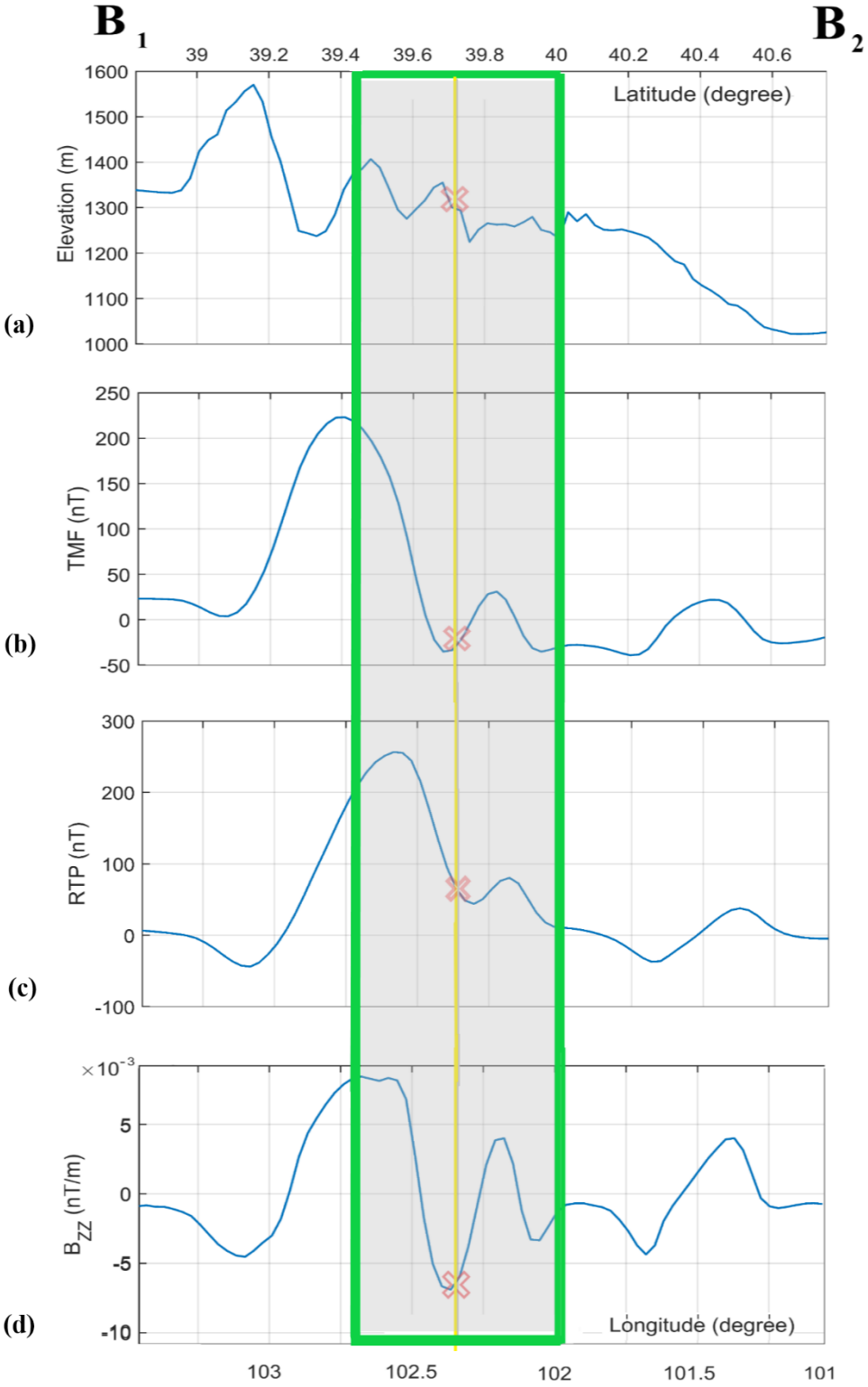

Figure 6.6 The B_1B_2 Profile for: (a) topography; (b) total magnetic field anomaly, TMF; (c) reduction to the pole transformation of TMF, RTP; (d) vertical derivative of the vertical component of TMF, B_{zz}. The red cross indicates the proposed crater center and the shaded area the horizontal dimension of the crater in NW-SE direction. The lower and upper axes indicate longitude and latitude, respectively.

Fig. 6.3d shows the decrease of BA from N to S over the A_1A_2 profile. This trend is due to the mountainous zone in the S part of the map (see Figs. 6.2a, 6.3e) where the highlands' root extends deeper into the mantle according to isostasy. The TA parameter has almost the same properties as g_{zz}; the difference is that unlike g_{zz}, accentuating the shallower signals, TA emphasizes the anomalous structures at different depths. A number of faults in the vicinity of the potential crater could be observed from the TA map (Fig. 6.2g). The UPC-g_{zz} is another parameter that, ignoring the morphology of the layering, can reveal a circular denser structure, comprising less dense rock units in the center (Fig. 6.2i).

From the ridge detection theory [6], we have plotted small white circles in Fig. 6.4a to show the points where UPC-g_{zz} (at h=2 km) is maximum with significance levels of 2, 3, and 4; in other words, each of these circles signifies the g_{zz} parameter larger than its neighbors in 2, 3 and 4 directions, respectively. The significance value, $N \geq 2$, gives acceptable results for the ridge detection [6]. These circles coincide with the presumed rim of the proposed crater. The g_{zz} at a zero elevation also has the capability of detecting discontinuities like faults. The faults, shown by black rectangles in Fig. 6.4b, truncate g_{zz} with low linear or curvilinear quantities, coinciding with their planes, and parallel highs on either side. The faults lie in the NE, S, SW and W of the crater. Considering the direction of impactite from NW to SE [46] and strike of the faults close to the rim (NE-SW and W-E), it seems that the crater truncates these faulting trends. That is, the faults run from NE, disappear in the middle (in location of the crater), and then reappear on the W margin of the crater. This could imply the younger age of the crater with respect to the faults in its proximity. Du et al. [163] reported on the Cenozoic tectono-geomorphic evolution of the Yabrai Fault (YBF) and its impacts on the landscape formation of BJD during the late Quaternary. YBF is characterized by left-lateral strike-slip faulting with normal faulting components neighbouring the E part of the proposed impact structure. A 500 m uplift of the YBF central segment created a topographic barrier separating BJD and the Tengger Desert (see Fig. 6.1), which may have played a key role in formation of the megadune-lake pattern. Dating of the onset of normal faulting to 5-2 Ma based on very scattered (U-Th)/He data and slip rates obtained from U-Th dating of calcite formation on fault striation and ^{10}Be exposure dating of river terraces and alluvial fans, both dated to the Late Pleistocene, is inconsistent with the abrupt change from the desert to lake environment in the Middle Pleistocene. The uplift process may have started much later and was much faster, consistent with the impact into the present megadune-lake area at the foothills of the Yabulai Mts at 0.79 Ma.

Typically, the rim and areas close to the impact crater could be affected by the impact energy discharge. The uplifted deformed rim and developed fracturing, slump and thrust faulting planes within the rim arrange in a roughly circular pattern, showing a high comb factor; the SA solutions seem to be combed in preferred directions (Figs. 6.4c, d) [32,33,53]. Additionally, beyond the crater rim, some zones with weaker structures may also be affected by the shock wave of the impact, thereby undergoing more intense deformation, fracturing, schistosity, and accumulation. Consequently, the impact zone would have some areas with parallel SA in its vicinity farther from the crater rim. For example, in the area under question, Figs. 6.4c, d demonstrate that there are some biased lineaments from 120° to 180° (Figs. 6.4e, f). These lineaments indicate the topography and fault system trends, which could not be due to the impact, but possibly, affected by it.

The typical magnetic signature in the area is different from gravity, indicating more complicated behavior of the magnetic property compared with the gravity. The TMF value (~300 nT) at the S rim is probably partly due to the mountainous structure of the granitic bedrock, where the measurement distance is smaller (4 km above the reference ellipsoid) (Figs. 6.2a, 6.5a). This large magnetic anomaly,

however, extends to W, where elevation drops. The shift of RTP towards the center of the potential crater is neither consistent with topography nor with the gravity anomaly. This strengthens the hypothesis in favor of the presence of a highly magnetic, but thin and wide layer under the sands of the S part of BJD. This broad anomaly could be a shallow thin melt sheet. Its positive signature implies an induced source of magnetization or re-magnetization at a time when geomagnetic field was of normal polarity, same as today. Stratigraphic positions of microtektite layers associated with the Australasian impact indicate that the impact happened 12–15 ka prior to the Matuyama-Brunhes geomagnetic reversal [170], at a time when geomagnetic field was about to change its polarity from reverse to normal. The melt sheet must have been above the Curie temperature thousands of years after the impact, and cooled below this temperature after the geomagnetic field underwent a polarity change from reverse to normal. Then the melt sheet acquired a positive remanent magnetization persisting to the present day. Such a scenario is consistent with models of cooling time of impact melts [171,172], as well as with the signs of hydrothermal activity observed in the proposed impact area in BJD. Formation of sublacustrine carbonate spring mounds in BJD lakes resembles the postimpact hydrothermal activity known from the Ries impact structure [46]. Recently reported "warm island effect" observed in the BJD megadune-lake area [173] may also support our hypothesis.

The positive and negative bands of B_{zz} strengthen the signals from to the most superficial or smallest scale anomalies. The stripping B_{zz} pattern throughout the whole map (Fig. 6.5c) outlines the extent of a magnetic carrier formation and suggests directionality from NW to SE. A narrow band of negative B_{zz} values around the large magnetic anomaly S of the crater (Fig. 6.5c) indicates the location where most of the momentum of the impactor was delivered and thus where most shock melting, and vaporization took place. Unlike B_{zz} which focuses on small or shallow structures, TA boosts the strongest signals from both deep and shallow structures (Fig. 6.5d). The TA marks some of the faults and crystalline rocks with distinct magnetic signatures. Except the Yabrai Fault (YBF), all other faults, and the boundary to the likely melt sheet inside the cavity detected from RTP, could be marked by the LTHG map (Fig. 6.5e).

6.4 Conclusions

We provide analysis and interpretation of satellite magnetic and gravity data in the SE part of the Badain Jaran Desert (BJD), Northwest China, to seek for a potential zone for finding the parent impact crater of Australasian tektites (AAT). Although differently, both gravity and magnetic data represent supportive evidence for the presence of a suitable large crater on the southern margin of BJD, buried under sand megadunes. The dynamic nature of the Earth's interior and atmosphere tend to eliminate the crater's trace; thus it is not surprising that the morphology of the area does not give any information in this regard.

From the gravity disturbance (δg) and Bouguer anomaly (BA) it can be concluded that there is a high-density ring-like structure encircling a low density cavity. The average difference between BA values over the likely cavity and rim (~ 30 mGal) supports the probability of the existence of a crater in the area. Both δg and BA highs over the rim may be owing to the impact related uplifted crystalline bedrock. On the contrary, lower δg and BA in the center could result from lack of mass due to excavation, brecciated and fractured infill materials, and Holocene low-density sediments (sand and dust).

The high frequency amplifying filters, T_{zz} and g_{zz}, reveal the shallow masses, the former with topography and the latter without it. A rim structure and cavity with larger and smaller densities, respectively, being the most surficial features, are detected by these two parameters. The tilt angle (TA) and g_{zz} exhibit the rim structure, the cavity, and several faults surrounding the crater. From the g_{zz} signature, the faults running from NE side of the crater to its W seem to have been truncated by the impact.

Due to the amount of energy discharged within the impact area, the rim structure is deformed and fractured. The strike alignment (SA) solutions could reveal the lineaments of the fractures and accumulation of material, which are along the perimeter of the rim. Farther from the rim, some zones are affected more by the impact energy, and the structural weakness prompts these zones to develop parallel SA and high comb factors.

The most prominent magnetic anomaly is situated in the S and SE of the potential crater, probably downrange the trajectory of the impactor motion from NW to SE. Assuming that the magnetization is solely induced by the ambient magnetic field, the reduced to the pole (RTP) map shifts this anomaly further into the crater, reinforcing its association with the crater itself. A comparison between the RTP and BA maps suggests that the magnetic anomaly within the crater is not likely to be thick or deep but rather thin, shallow, and extensive. This is supported by the absence of a corresponding significant mass anomaly, containing ferromagnetic material, in the BA map. The positive sign of the magnetic anomaly near the crater indicates induced magnetization or remagnetization of the large melt pool during a normal polarity phase.

While B_{zz} accentuates and differentiates the shallow sources of magnetism, TA delineates the deep-seated and shallow structures with distinct magnetic properties like faults and mountains. LTHG, on the other hand, marks the borders where the magnetization changes. Therefore, TA and LTHG can isolate the anomalous RTP, suggesting an existence of a large rock body shock-melted by the impact.

To summarize, the gravity and magnetic data support the assumption that the AAT parent crater may be present in the megadune-lake area of BJD.

6.5 Data and methodology

In this study, we employed the combined free air gravity field model EIGEN-6C4 [174], and a Bouguer model derived from it [175], the EMAG2 magnetic model [64], and the ETOPO1 topography model [63]. We derive free air gravity disturbance (δg) and its vertical component derivative (T_{zz}), strike angle (SA), Bouguer anomaly (BA), tilt angle (TA) and the first vertical derivative of BA (g_{zz}), total magnetic field anomaly (TMF), reduction to the pole transformation (RTP), the first vertical derivative of the vertical component of TMF (B_{zz}), and TA and logistic total horizontal gradient (LTHG) of RTP. The derivatives are calculated through the fast Fourier transform [1,12,31]. For details see Appendix A in the Supplementary file.

Acknowledgements

The authors thank two anonymous reviewers and the editor for their valuable comments.

Author contributions

K.K.: concept, calculations, production of figures, interpretations, writing, revision; G.K.: concept, interpretations, language, revision; J.M.: concept, interpretations, language and format editing, revision; V.M.: geological interpretations; V.S.: geological setting.

Competing interests

The authors declare no competing interests.

6.6 Data Availability

The data are available through Mendeley Data: https://doi.org/10.17632/g7jpg668wf.1.

Chapter 7

Subsurface Geology Detection from Application of the Gravity-Related Dimensionality Constraint - Article 4

Subsurface Geology Detection from Application of the Gravity-Related Dimensionality Constraint

Kurosh Karimi[1*], Gunther Kletetschka[1,2]

1 Institute of Hydrogeology, Engineering Geology and Applied Geophysics, Faculty of Science, Charles University, Prague 12843, Czech Republic.

2 Geophysical Institute, University of Alaska - Fairbanks, AK 99709 Fairbanks 903 N Koyukuk Drive, AK, USA

* Kurosh Karimi, kurosh.karimi@natur.cuni.cz, corresponding author

ORCID:

Kurosh Karimi: https://orcid.org/0000-0002-3496-8330,

Gunther Kletetschka: https: //orcid.org/0000-0002-0645-9037.

Abstract

Geophysics aims to locate bodies with varying density. We discovered an innovative approach for estimation of the location, in particular depth of a causative body, based on its relative horizontal dimensions, using a dimensionality indicator (*I*). The method divides the causative bodies into two types based on their horizontal spread: line of poles and point pole (LOP-PP) category, and line of poles and plane of poles (LOP-POP) category; such division allows for two distinct solutions. The method's depth estimate relates to the relative variations of the causative body's horizontal extent and leads to the solutions of the Euler Deconvolution method in specific cases. For causative bodies with limited and small depth extent, the estimated depth ($z^{\wedge}_0$) corresponds to the center of mass, while for those with a large depth extent, $z^{\wedge}_0$ relates to the center of top surface. Both the depth extent and the dimensionality of the causative body influence the depth estimates. As the depth extent increases, the influence of *I* on the estimated depth is more pronounced. Furthermore, the behavior of $z^{\wedge}_0$ exhibits lower errors for larger values of *I* in LOP-POP solutions compared with LOP-PP solutions. We tested several specific model scenarios, including isolated and interfering sources with and without artificial noise. We also tested our approach on real lunar data containing two substantial linear structures and their surrounding impact basins and compared our results with the Euler deconvolution method. The lunar results align well with geology, supporting the effectiveness of this approach. The only assumption in this method is that we should choose between whether the gravity signal originates from a body within the LOP-PP category or the LOP-POP category. The depth estimation requires just one data point. Moreover, the method excels in accurately estimating the depth of anomalous causative bodies across a broad spectrum of dimensionality, from 2D to 3D. Furthermore, this approach is mathematically straightforward and reliable. As a result, it provides an efficient means of depth estimation for anomalous bodies, delivering insights into subsurface structures applicable in both planetary and engineering domains.

7.1: Introduction

A primary objective of potential field survey is to locate geological bodies beneath the surface [1]. Depth estimation of causative bodies with contrasting magnetization and/or density ranges from a simple graphical approaches[7,14,176] to more sophisticated inverse problems[5,9,28,29,38,41,43,177–179]. In an influential paper, Thompson (1982)[28] introduced a location estimation technique based on Euler's homogeneity relationship, enabling the investigation of subsurface magnetic anomalies with varying shapes. The

location estimation of the gravity anomalies using Euler's homogeneity equation was later considered by others (e.g., Reid et al, 1990[29]). The advent of Marussi tensor (e.g., Pedersen and Rasmussen, 1990)[13], also known as the gravity gradient tensor (GGT), improved the depth and edge detection of gravitationally anomalous structures to a great extent. GGT extracts information from geologic bodies with contrasting density relative to their surroundings. This tensor, in itself, is a powerful tool to give quantitative information about the strike direction[5,32,53], horizontal dimensions[39], structural weakness[32,53], and locations[1,28] related to subsurface anomalous constructs. It applies in both engineering and planetary exploration, and has been extensively used for detecting local petroleum, metal, diamond, and groundwater [5–16], as well as for exploration of the Earth's crust[32,35,36,39,55], and celestial bodies[18,19,53,54]. Nowadays, the gravity data obtained from satellites have significantly improved in precision and ground resolution, enabling the GGT to explore planetary properties in more detail than ever before [62].

Pedersen and Rasmussen (1990)[13] conducted an in-depth study of GGT, including its invariants, eigenvalues, and eigenvectors, which was later expanded and used by Marson and Klingele (1993)[180], Zheng *et al.* (2000)[41], Mikhailov *et al.* (2007)[38], Beiki and Pedersen (2010)[5] and Zuo *et al.* (2017)[44] for depth estimation of gravity anomalies. Zhang *et al*. (2000)[41] and Mikhailov *et al.* (2007)[38] showed that, instead of the gravity anomaly, the components of the GGT can be used to improve the Euler deconvolution method. Beiki and Pedersen (2010)[5] developed a new technique to depth estimate of geological structures using the eigenvector analysis of the GGT. Wedge (2013)[181] created an algorithm, using an accumulation method to identify potential mass anomalies by casting lines through a volume based on GGT properties and accumulating votes. Local maxima in the volume, in his algorithm, correspond to mass anomalies. Zhou (2015)[42] extended the normalized imaging method to interpret GGT data and normalized directional analytic signals and calculated the salt dome structure's horizontal position and depth range. Zuo *et al*. (2017)[44] introduced a method using eigenvector analysis for locating the centroids and horizontal boundaries of geological structures from GGT. The method employed eigenvector analysis to extract source centroid information, differing from traditional potential field boundary detection. This discussed theoretical foundations and the physical significance of GGT eigenvector analysis and addressed challenges related to multiple sources and parameter identification. Yuan *et al.* (2020)[40] came with a novel depth estimation method based on the Chebyshev-Padé downward continuation technique, emphasizing stability and depth calculation; the research compared filter curves in the wave number domain between Tikhonov regularization and Chebyshev-Padé methods, highlighting the convergence of the latter's filter curve to zero, making it suitable for depth estimation. Zhou *et al.* (2021)[43] improved the normalization imaging method using the downward continuation method based on continued fractions, obtaining the source geometric parameters under the source distribution at different depths.

In parallel, the magnetic gradient tensor[31,182], extracted from the directional derivatives of the magnetic field anomaly has also been utilized by some workers. However, the magnetic gradient tensor is less informative than its gravity analogue, due to the complex nature of the magnetic anomaly field.

The dimensionality indicator (*I*), varying from zero to 1, is a quantitative index used to indicate the relative magnitudes of the horizontal dimensions of a causative body[13]. It is determined when formulating the characteristic equation to calculate the eigenvalues of the GGT. From a geophysical standpoint, a causative body can be categorized as pure 2-dimensional (2D), pure 3-dimensional (3D), or somewhere in between (2-3D). The dimensionality indicator for a pure 2D, pure 3D and 2-3D causative body is defined as follows[13]:

- Pure 2D (*I=0*): One horizontal dimension goes to physical infinity and becomes much larger than the other horizontal dimension in practice.
- Pure 3D (*I=1*): The two horizontal dimensions of the body are identical.

- 2-3D ($0 < I < 1$): One horizontal dimension is larger than the other, but the dimensions are still comparable.

The dimensionality classification strongly depends on the dimensions of the causative body, the measurement point distance from the body, and the resolution of the grid unit[54]. While the usage of *I* has been limited to constraining the relative horizontal dimensions of subsurface anomalous structures[5,38,183] to show whether it is 3D or 2D, we show in this research that further information could be extracted from this parameter. Though Mikhailov *et al.* (2007)[38] used *I* to calculate the depth of two simple-shaped gravity anomalies: the point pole (*I=1*) and the line of poles (*I=0*), they did not provide any solutions for cases where *I* is neither zero nor one. They considered the structural index (SI) in Euler deconvolution method as 1+ *I*, whereby set up SI=1 for a line of poles and SI=2 for a point pole. Here, we fill this research gap and outline a new method for detecting the depth of geological constructs with a spectrum of dimensionality indicator from zero to one. We test the effect of depth extent on the solutions and examine synthetic data with isolated and interfering different shape sources in the presence and absence of 5% random Gaussian noise. While this method can be applied in engineering domains, ranging from micro-gravimetry to ordinary ground and airborne gravimetry, we choose to demonstrate its application on real lunar data at a planetary scale. For this purpose, we use the Bouguer potential, obtained by subtracting the topographic gravity potential from the measured gravity potential, represented by spherical harmonic series (SHS). The applied gravity model for the Moon is "GRGM1200A"[58], truncated at d/o=600 and continued downward to an elevation of 5 km with respect to the reference ellipsoid. The truncation and continuation serve to minimize the artifacts due to frequency aliasing[58]. The grid resolution of GRGM1200A at d/o = 600 is approximately 10 km on the ground with a precision of around 10 mGal[19]. The utilized topographic gravity model "STU_MoonTopo720"[59], was truncated at a degree and order of 600 to be consistent with the measure gravity model. The Bouguer-type Γ components are extracted using Graflab software[68]. Our methodology, when applied to real data, is compared with the Euler deconvolution method, and our solutions fall within the range of solutions provided by Euler deconvolution.

An important point regarding the components of GGT is that (1) they can be directly calculated by taking the second directional derivatives of the gravity potential in the spatial domain, (2) they can be obtained by taking derivatives in the Fourier domain and then transforming back to the spatial domain, and (3) they can be measured directly by gradiometers, on board the ships, airplanes and on the ground. In the case of gradiometry, the error effect is even less significant because of directly measured (not computed) components of GGT[5].

7.2: Theory

We present a formula utilizing the components of GGT to estimate the distance to an unknown causative body underground (z_0). When the causative body has a limited depth extent, the estimated depth ($\hat{z}_0$) corresponds to the depth of the center of mass (COM); conversely, for vertically extended bodies, $\hat{z}_0$ represents an estimation of the center of top surface (COTS).

Due to the non-uniqueness of the gravity data, determining the precise geometry of a causative body that generates the gravity anomaly field is impossible [1]. In other words, numerous models can produce the same gravity response. Nonetheless, the lack of uniqueness can be addressed by considering hypotheses about the shape of the density transition. In fact, it is theoretically more advantageous to work with a generalized geophysical hypothesis and arrive at a single solution, rather than accepting a solution that could be significantly divergent from reality due to adherence to a purely mathematical criterion (as discussed in Sanso *et al*., 1986)[184]. Considering a priori known geometry, the horizontal extent of the body can also be inferred from the gravity data.

The GGT, $\mathbf{\Gamma}$, is defined as[13].

$$\mathbf{\Gamma} = \nabla(\mathbf{\nabla}\mathrm{T}) = \begin{bmatrix} \Gamma_{ii} & \Gamma_{ij} & \Gamma_{ik} \\ \Gamma_{ji} & \Gamma_{jj} & \Gamma_{jk} \\ \Gamma_{ki} & \Gamma_{kj} & \Gamma_{kk} \end{bmatrix} \quad (1)$$

where T is disturbing gravity potential, subscripts *ij* are two orthogonal components of the coordinate system (e.g., in Cartesian coordinates each of "*i*", "*j*" and "*k*" are x, y, z). The *ith* component of the gravity vector is $g_i = \frac{\partial T}{\partial i}$ and the second derivative components of the gravity potential are $\Gamma_{ij} = \frac{\partial}{\partial i}(g_j) = \frac{\partial}{\partial i}\left(\frac{\partial T}{\partial j}\right) = \frac{\partial^2 T}{\partial i\, \partial j} = \Gamma_{ji}$.

There are only five independent components in equation (1) for two reasons: (1) In a free source condition (that is when the measurement is conducted out of the gravitational source, from satellite, airplane or on the Earth surface), the Laplace equation holds, i.e., $\mathbf{\nabla}^2\,\mathrm{T} = 0\ and\ \Gamma_{kk} = -(\Gamma_{ii} + \Gamma_{jj})$, and (2) In as much as $\nabla \times \vec{g} = 0$, $\mathbf{\Gamma}$ is symmetric ($\Gamma_{ik} = \Gamma_{ki}, \Gamma_{ij} = \Gamma_{ji}, and\ \Gamma_{jk} = \Gamma_{kj}$).

$\mathbf{\Gamma}$ has three invariants I_0, I_1 and I_2, meaning that under any coordinate rotation, their values do not change[13]:

$$I_0 = Trace(\mathbf{\Gamma}) = \sum_{i=1}^{3} \Gamma_{ii} = 0$$

$$I_1 = \frac{1}{2}((Trace\ (\mathbf{\Gamma}))^2 - Trace(\mathbf{\Gamma}^2)) = \Gamma_{ii}\Gamma_{jj} + \Gamma_{ii}\Gamma_{kk} + \Gamma_{jj}\Gamma_{kk} - {\Gamma_{ij}}^2 - {\Gamma_{jk}}^2 - {\Gamma_{ik}}^2 \quad (2)$$

$$I_2 = det(\mathbf{\Gamma}) = \Gamma_{ii}\left(\Gamma_{jj}\Gamma_{kk} - \Gamma_{jk}\Gamma_{kj}\right) + \Gamma_{ij}\left(\Gamma_{jk}\Gamma_{ki} - \Gamma_{ji}\Gamma_{kk}\right) + \Gamma_{ik}\left(\Gamma_{ji}\Gamma_{kj} - \Gamma_{jj}\Gamma_{ki}\right) \quad (3)$$

Since $\mathbf{\Gamma}$ is a symmetric matrix, its eigenvectors and eigenvalues should be perpendicular and real, respectively. Thus, it follows that the dimensionality indicator (*I*) be[13]:

$$0 \le I = -\frac{(I_2/2)^2}{(I_1/2)^3} \le 1 \quad (4)$$

Γ_{zz}, I_1, and I_2 are three parameters that amplify the anomalous sources that are near the surface and/or small. In other words, the signals from geological structures, whether deep or broad, are attenuated by these parameters. The unit of Γ_{zz} is acceleration divided by distance ($(m/s^2)/m = s^{-2}$). According to relations (2) and (3), the units of I_1 and I_2 are s^{-4} and s^{-6}, respectively.

In potential field data, the signal from the causative body falls off as a function of the inverse of its distance from the observation point[1]. That is, the signal from the upper parts is stronger than the lower parts of the body in g_z parameter. Additionally, the signals arising from the shallow parts are amplified by Γ_{zz} (This is because Γ_{zz} is obtained by the multiplication of wavenumber in g_z in the Fourier domain, gaining higher weights by increasing wave number or getting closer to the surface). Since in estimating the depth of anomalous structures, we employ g_z and Γ_{zz}, it stands to reason that the upper parts have a major contribution to the received signals. Therefore, depending on the depth extent of the body, the $z\hat{}_0$ could represent the COM in the case of limited and small depth extent, or the COTS if the depth extent is extended.

Here, we consider prismatic bodies as models, which can represent various geological features. We explore two types of models, those that lie between a line of poles and a point pole (LOP-PP) (Figure 7.1a), and those that lie between a line of poles and a plane of poles (LOP-POP) (Figure 7.1b). Depending on the horizontal extent of the anomalous mass, the user can choose between the two categories of solutions explained further in the next sections.

7.2.1: Simulated Data

2-3D Models

When dealing with a causative body that does not maintain a balance between its horizontal dimensions, implying it is 2-3D in nature, it can be effectively modelled using a rectangular prism. This prism is characterized by dimensions $\Delta x = x_2 - x_1, \Delta y = y_2 - y_1,$ and $\Delta z = z_2 - z_1$. The disturbing gravity vector, $\mathbf{g} = \begin{bmatrix} g_x \\ g_y \\ g_z \end{bmatrix}$, of this prismatic construct in a Cartesian coordinates system is[185]:

$$(g_x)_{2-3D} = GM \sum_{i=1}^{2}\sum_{j=0}^{2}\sum_{k=0}^{2} \mu_{ijk} \left[X \arctan\left(\frac{Z\,Y}{X\;R_{ijk}}\right) - \; Z \ln\left(R_{ijk} + Y\right) - \; Y \ln\left(R_{ijk} + Z\right)\right]$$

$$\left(g_y\right)_{2-3D} = GM \sum_{i=1}^{2}\sum_{j=0}^{2}\sum_{k=0}^{2} \mu_{ijk} \left[Y \arctan\left(\frac{X\,Z}{Y\;R_{ijk}}\right) - \; X \ln\left(R_{ijk} + Z\right) - \; Z \ln\left(R_{ijk} + X\right) \right]$$

$$(g_z)_{2-3D} = GM \sum_{i=1}^{2}\sum_{j=0}^{2}\sum_{k=0}^{2} \mu_{ijk} \left[Z \arctan\left(\frac{X\,Y}{Z\;R_{ijk}}\right) - \; X \ln\left(R_{ijk} + Y\right) - \; Y \ln\left(R_{ijk} + X\right) \right] \quad (5)$$

where $X = (x - x_i),\ Y = \left(y - y_j\right),\ Z = (z - z_k)$, *i, j, k* are 1 and 2

$$R_{ijk} = \sqrt{(x - x_i)^2 + \left(y - y_j\right)^2 + (z - z_k)^2} \text{ and } \mu_{ijk} = (-1)^i\,(-1)^j\,(-1)^k$$

As for the components of GGT for this 2-3D prismatic body, one can directly take directional derivatives of the components above in the spatial domain. An alternative way which is mathematically less cumbersome is employing Fourier domain for calculation of the derivatives and then transforming the results back to the spatial domain.

7.2.2: Depth Constraint

Having an a priori depth to the COM (z_0), we define a parameter,f, over the COM of a prismatic body, (x_0, y_0). The horizontal location of the COM (we call it target) could be attained from Γ_{zz} in the case of LOP-PP category[5,13], and from the logistic total horizontal gradient LTHG filter[39] for the LOP-POP category. In fact, LTHG peaks over the edges of a POP. Therefore, based on the margins, the target could be marked. In this event, any point inside the horizontal trace of the POP, far from the edges, could be considered as the target.

$$f \; = z_0 \left[\frac{\Gamma_{zz}}{g_z}\right]_{(x_0,y_0)} \quad (6)$$

Then two categories of models_ LOP-PP and LOP-POP _ are considered (Figure 7.1a and 7.1b).

Depending on the assumed model, f_{LOP-PP} and $f_{LOP-POP}$ are defined as:

$$(f)_{LOP-PP} = (z_0)_{LOP-PP} \left[\frac{\Gamma_{zz}}{g_z}\right]_{(x_0,y_0)} \quad (7)$$

$$(f)_{LOP-POP} = (z_0)_{LOP-POP} \left[\frac{\Gamma_{zz}}{g_z}\right]_{(x_0,y_0)} \quad (8)$$

f at (x_0, y_0) is observed to vary from 1 to 2 for different models within LOP-PP category, and from 1 to 0.2 for various models within LOP-POP category.

At the same time, *I* for LOP-PP, and LOP-POP categories vary from 0 to 1 at the target. We examined the variations of f obtained from (7) and (8) with respect to *I* for the two groups of models (Figures

7.1c and 7.1d). When the body changes from LOP with *I=0* to PP with *I=1* (Figure 7.1a), f increases from 1 to 2 non-linearly (Figure 7.1c). In contrasts, when the body changes from an LOP with *I=0* to a POP with *I=1* (Figure 7.1b), f decreases from 1 to 0.2 non-linearly (Figure 7.1d). The variations of f with respect to *I* is independent of the depth of the causative body and its real horizontal geometrical shape for each category. Therefore, if we gain the mathematical relation between f and *I*, the depth of body from relations (7) and (8) could be estimated. Fitting 10th order polynomials to f in f-*I* curves in Figures 7.1c and 7.1d, two categories of f over the target at (x_0, y_0) are attained:

$$f_{LOP-PP} = \sum_{i=0}^{10} (P_i)_{LOP-PP}\ I(x_0, y_0)^{10-i} \qquad (9)$$

where P_{LOP-PP} = [2103.18992684381, -9631.96402211124, 18577.6251289147, -19588.2995049138, 12248.4374659662, -4593.09200836508, 983.430010323201, -99.9187201174857, 0.120606818475533, 1.40856361966959, 1.01450450959620]

$$f_{LOP-POP} = \sum_{i=0}^{10} (P_i)_{LOP-POP}\ I(x_0, y_0)^{10-i} \qquad (10)$$

where $P_{LOP-POP}$ = [6848.67493381295, -36658.5991267149, 84416.3911603620, -109383.131515810, 87587.6244287788, -44828.8689194104, 14673.1097375456, -2993.63766093542, 361.752513427095, -24.3068510461594, 1.20590372220942]

The Root Mean Square (RMS) error for f_{LOP-PP} and $f_{LOP-POP}$ in Figures 7.1c and 7.1d are, respectively, 0.004 and 0.010. Although the higher order of polynomials gives more precise estimations of f, the 10th degree is precise enough to solve for the depth in this study.

Consequently, from relations (7) and (8), the depth of the anomalous mass could be estimated as:

$$\left(\hat{z}_0\right)_{LOP-PP} = (f)_{LOP-PP} \left[\frac{g_z}{\Gamma_{zz}}\right] \qquad (11)$$

$$\left(\hat{z}_0\right)_{LOP-POP} = (f)_{LOP-POP} \left[\frac{g_z}{\Gamma_{zz}}\right] \qquad (12)$$

Three endmembers of the models- LOP, PP and POP- are, respectively:

$$f = 1 \rightarrow \left(\hat{z}_0\right)_{LOP} = (1) \left[\frac{g_z}{\Gamma_{zz}}\right] \qquad (13)$$

$$f = 2 \rightarrow \left(\hat{z}_0\right)_{PP} = (2) \left[\frac{g_z}{\Gamma_{zz}}\right] \qquad (14)$$

$$f = 0.2 \rightarrow \left(\hat{z}_0\right)_{POP} = (0.2) \left[\frac{g_z}{\Gamma_{zz}}\right] \qquad (15)$$

From relations (13), (14) and (15), the coefficients 1, 2, and 0.2 are the same structural index, appeared in the final solutions of Euler deconvolution method[28]. Although structural index for POP is considered 0.5 in Euler method[28], 0.2 seems to be a more precise measure in an extreme case of a 3D POP, where the horizontal dimensions of the body are large enough. Note that Euler deconvolution only considers the extreme cases, i.e., LOP, PP, and POP. Depending on *I*, our methodology, however, derives a spectrum of solutions where transitions between extreme shapes occur, meaning that the causative body is not limited to pure 2D or pure 3D but can also be 2-3D.

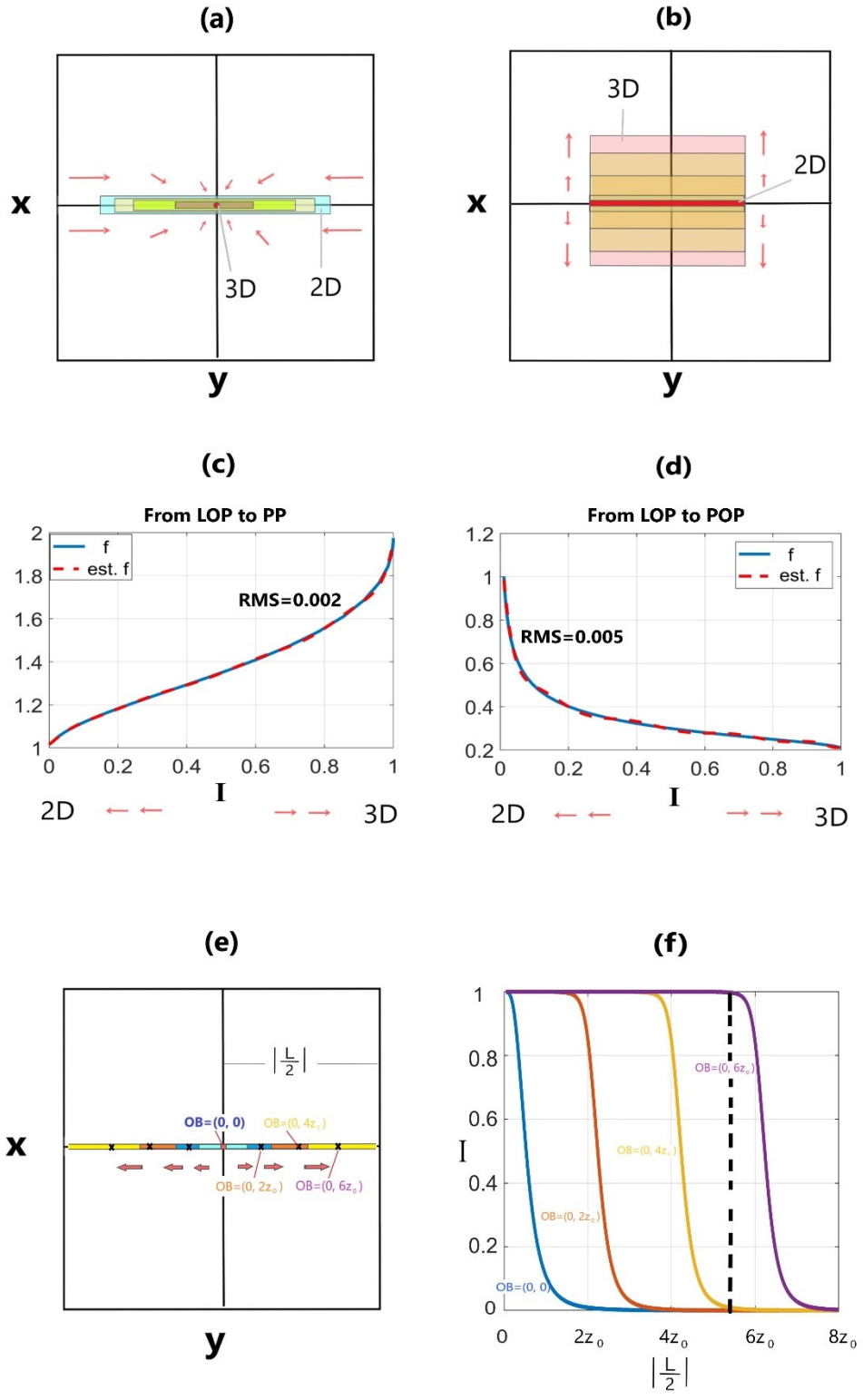

Figure 7.1: variations of a causative body (a) from line of poles (LOP) (pure 2D) to point pole (PP) (pure 3D); (b) from line of poles to plane of poles (POP) (pure 3D); variations of f with respect to I when the body changes from (c) LOP to PP; (d) from LOP to POP. The red dashed lines in "c" and "d" are 10th order polynomial, estimating f in terms of I. (e) variations from LOP to PP with observation points (OB) with (x, y) coordinates at (0, 0), (0, $2z_0$), (0, $4z_0$), and (0, $6z_0$) where z_0 is the depth of the causative body (y is in terms of depth); (f) variations of I at different observation points when the length

changes from zero to physical infinity ($|\frac{L}{2}| = 8z_0$). The dashed black line in Figure f demonstrates the condition in which the length of the LOP is fixed but the observation point changes.

We examined the behavior of I with respect to half-length $|\frac{\Delta y}{2}| = |\frac{L}{2}|$ along the strike when the observation point (OB) is on the y axis but shifts from the center to the sides of the LOP (Figure 7.1e). At the center, OB = (0, 0), when $L \to 0$, $I \to 1$. Increasing the length of the source $|\frac{L}{2}|$, I drops. Where $|\frac{L}{2}|$ goes to physical infinity (here to $8z_0$), I approaches zero (Figure 7.1f, blue curve). In the meantime, $f(I)$ falls from 2 to 1 as illustrated in Figure 7.1c (blue curve). When the observation point is at $(x = 0,\ y = 2z_0)$ (Figure 7.1e), and $|\frac{L}{2}|$ grows from zero to $8z_0$, the body appears to be 2-3D for observation points $(x = 0,\ y \text{ close to } 2z_0)$ (Figure 7.1f, red curve). Increasing $|\frac{L}{2}|$, I decreases to zero, implying the observer sees the body as a 2D structure. For farther observational points from the center, say, $(x = 0,\ y = 4z_0)$, the transition from pure 3D to pure 2D occurs at $(x = 0,\ y \text{ close to } 4z_0)$ (Figure 7.2b, yellow curve). The purple curve shows the observation point at $(x = 0,\ y = 6z_0)$. The dashed black line in Figure 7.1f demonstrates a fixed value for the half-length of the LOP (5.5 z_0), but variable observation points. This means that if the half-length of LOP ($\frac{L}{2}$) equals $5.5z_0$, the observer at $(x = 0,\ y = 6z_0)$ calculates $I \approx 1$, while the other observers calculate $I \approx 0$. As a result, the observation point affects the calculation of I, thereby f and $\hat{z_0}$. It is of note that our methodology mandates the observation point to be within the horizontal extent of the body and far from the edges if the horizontal extent is wide.

7.2.3 The Effect of Depth Extent on the Depth Solutions

In the previous section, we derived a general formula for depth estimation of two different types of causative bodies, LOP-PP and LOP-POP, with small depth extents. In such cases, the estimated depth represented the depth to the center of mass.

We further investigated the impact of varying depth extent of the anomalous mass and the dimensionality indicator (I) on $\hat{z_0}$ using relations (11) and (12), assuming that the top surface is buried at z_0 (Figure 7.2). When the LOP-PP category is extremely thin (depth extent=0.02 z_0), the estimated depth appears to be independent of variations in I (Figure 7.2a). However, as depth extent increases, the $\hat{z_0}$ becomes more reliant on I. Furthermore, Figure 7.2a demonstrates that increasing depth extent also influences the average $\hat{z_0}$. As depth extent approaches physical infinity (approximately 7.5 z_0), the $\hat{z_0}$ converges to ~1.75 z_0.

For the LOP-POP category, we examined $\hat{z_0}$ with varying depth extent and I, and the results are depicted in Figure 7.2b. Similarly to the LOP-PP solutions, the $\hat{z_0}$ for the LOP-POP category is dependent on I. However, the errors for LOP-POP solutions with larger I are smaller compared to the errors of LOP-PP solutions. As depth extent increases toward physical infinity, the average $\hat{z_0}$ for LOP-POP solutions converges to ~1.25 z_0.

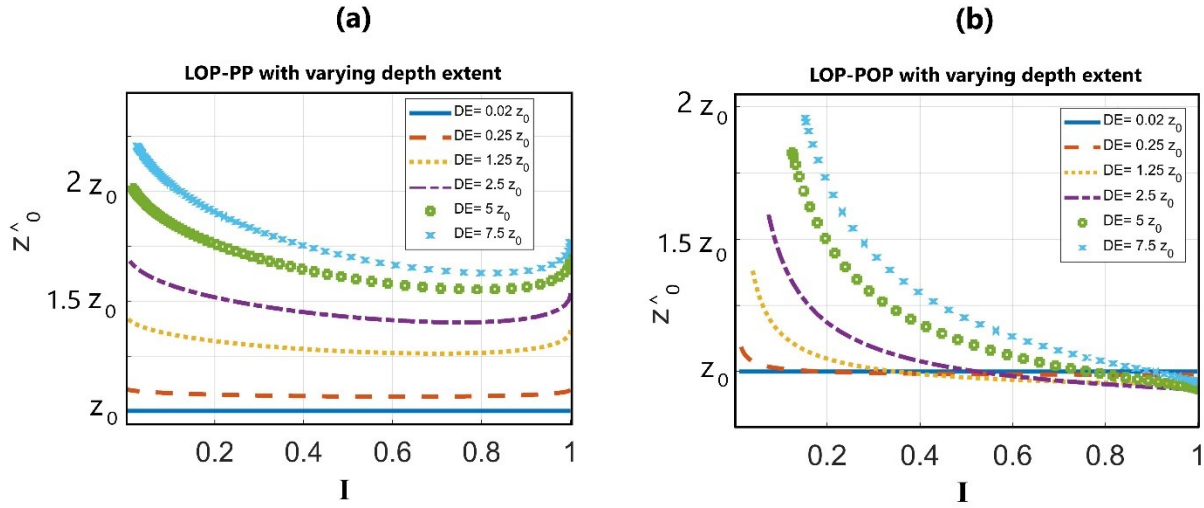

Figure 7.2: Variations of estimated depth ($\hat{z}_0$) with respect to *I* and depth extent (DE) for (a) LOP-PP category, and (b) LOP-POP category.

7.2.4 Simulated Models in the Absence and Presence of Noise

Here we consider simulated isolated and interfering pure 2D, pure 3D and 2-3D sources without and with 5% random Gaussian noise. The specification of the models and their positions are introduced in Figure 7.3 and in Tables 7.1 and 7.2. At each case, we calculated the Normalized Root Mean Square Error (NRMSE) of the estimated location (Tables 6.1 and 6.2).

The NRMSE is defined as follows[31]:

$$NRMSE = \frac{1}{z_0}\sqrt{\frac{(\hat{x}_0-x_0)^2+(\hat{y}_0-y_0)^2+(\hat{z}_0-z_0)^2}{N}} \times 100 \qquad (16)$$

Where $\hat{r}_0 = (\hat{x}_0, \hat{y}_0, \hat{z}_0)$ and $r_0 = (x_0, y_0, z_0)$ are the estimated COM/COTS (depending on the depth extent) and real position of the COM/COTS, respectively. *N* is the number of elements considered in relation (16). Exploring on a grid map requires *N=3* (for x, y, and z components), and on a profile, *N = 2*.

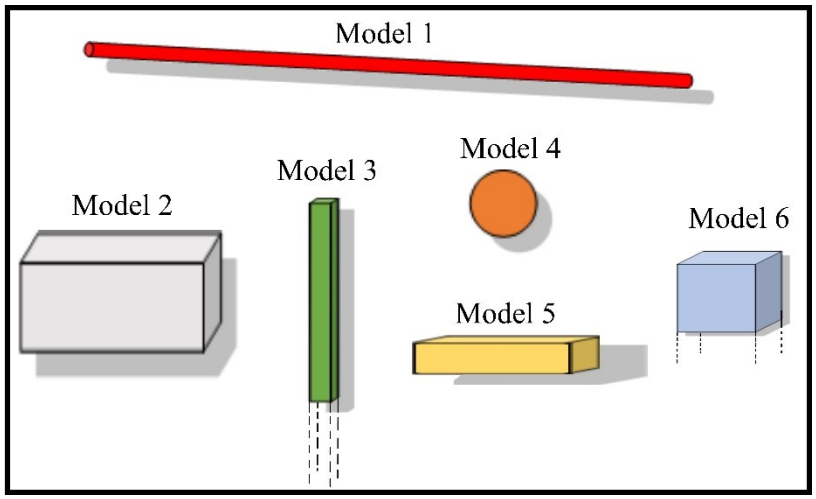

Figure 7.3: Model 1: Line of poles with Length of 40; Model 2: prismatic body with Width = 2, Length = 8, Depth extent = 4; Model 3 prismatic body with Width and Length = 1, Depth extent = 20; Model 4, point pole with radius 2, Model 5 prismatic body with Width=1, Length=6 and Depth extent = 2; Model 6 prismatic body with Width and Length = 40 and Depth extent = 60. The units for bodies' dimensions are meter. The apparent size of

the bodies is not representative of their real dimensions relative to each other. See Table 7.1 for information about the estimated model positions and I.

Table 6.1 presents an overview of various isolated models and their associated parameters, specifically focusing on the estimation of a COM and COTS, denoted as "$\hat{r_0}$". It investigates how the accuracy of these estimations varies under different noise conditions. The dimensions and distances in Table 6.1 are in meter.

Model 1: Line of Poles (LOP) with length of 40 m, and COM coordinates at (0, 0, z = 5m). Under noise-free condition, Model 1 exhibits a remarkably accurate estimation of " $\hat{r_0}$" with a low NRMSE of 0.1. However, when noise is introduced, the NRMSE increases to 10.29%, indicating a reduction in estimation accuracy. *I* in both conditions indicates an almost pure 2D body.

Model 2: Prismatic body with Length=8m, Width=2m, Depth extent=4m, and COM coordinates at (0, 0, z = 6m). *I* with and without noise are, respectively, 0.77 and 0.87, implying that the model is a 2-3D body. Although the effect of large depth extent in model 2 may reduce the accuracy of the solutions, they are still reasonable estimates of COM.

Model 3: Prismatic body with Length=1m, Width=1m, Depth extent=20m, and COTS coordinates at (0, 0, z = 2m). Despite a significant depth extent, the solutions estimate the COTS in this model well ((0,0, 3.72m) in noise-free condition versus (0,0, 2.88m) in noisy condition).

Model 5: Prismatic body with Length=6m, Width=1m, Depth extent=2m, and COM coordinates at (0, 0, z = 3m). The depth estimations in noisy and noise-free states are quite close (2.53m against 2.77m, respectively). Similarly, *I* values are calculated 0.64 and 0.65, in the order.

Model 6: a prismatic body with dimensions of Length=40m, Width=40m, Depth extent=60m, representing a Plane of Poles with physically infinite depth extent (60 m). The coordinates of the COTS are (0, 0, z = 3m). *I* decreases from 1 in noise-free state to 0.73 in noisy state. Though in presence of noise the NRMSE increases notably from 30.80% to 154.4%, one should notice that a major contribution to this error comes from the horizontal components of the estimated COTS, (-4.6m, -6.3m , z = 4.87m).

Table 7.1: Specifications of the isolated models along with their respective solutions. L is length, W is width and DE is depth extent, COM is center of mass, and COTS is center of top surface of a causative body. Grid unit is 0.1m by 0.1 m, the model dimension and distances are in meter, and GM=1 $N.m^2.kg^{-1}$.

Model	**Dimensions (L,W,DE)**	**r_0(m)**	**Noise=0**			**Noise=5%**		
			r_0^{est} (m)	***I***	**NRMSE (%)**	**r_0^{est} (m)**	***I***	**NRMSE (%)**
Model 1	(40,0,0)	(0, 0, z_{COM} = 5)	(0, 0,5)	0.02	0.1	(0, 0.6, 4.57)	0. 019	10.29
Model 2	(8,2,4)	(0, 0, z_{COM} = 6)	(0, 0, 5.54)	0.87	4.38	(0.3,0.4, 4.55)	0.77	14.74
Model 3	(1,1,20)	(0, 0, z_{COTS} = 2)	(0, 0, 3.72)	1	49.0	(0,0, 2.88)	0.83	25.42
Model 5	(6,1,2)	(0,0, z_{COM} = 3)	(0,0, 2.77)	0.65	4.33	(0.5,0, 2.53)	0.64	13.19
Model 6	(40,40,60)	(0,0, z_{COTS} = 3)	(0,0, 4.60)	1	30.80	(-4.6, -6.3, 4.87)	0.73	154.4

[1].

Table 6.2 provides an overview of different scenarios involving three interfering "Model 4" configurations (see Figure 7.3). It evaluates the estimation of the parameters I and $\hat{r}_0$ under two noise conditions, specifically no noise and 5% noise.

Three Interfering Model 4 with Equal Densities and Depths:

For this set of scenarios with equal densities (GM = 1 $N.m^2.kg^{-1}$) and equal depths (z_{COM}=3m), the $\hat{r}_0$ values under Noise=0 are relatively close and exhibit low NRMSE values. In presence of noise, however, the solutions become more inaccurate with NRMSE of about 12% for individual bodies.

Three Interfering Model 4 with Equal Densities but Different Depths:

In this case, GM = 1 $N.m^2.kg^{-1}$ for all three interfering bodies but the z_{COM} are different (3m, 2m, 4m). The $\hat{r}_0$ values under Noise=5% lose their great accuracy in comparison with the noise-free condition. Consequently, NRMSE values increase in noisy state, but the estimated depths still show a reasonable level of accuracy.

Three Interfering Model 4 with Different Densities and Depths:

These scenarios involve both different densities GM = 1, 1.5, and 2 $N.m^2.kg^{-1}$ and different depths, z_{COM} = 3m, 2m, 4m. Although in this state the depths and densities are variable, the solutions yield acceptable results, with NRMSE values comparable with the previous states.

Figure 7.4 indicates g_z, Γ_{zz}, and I for the three interfering configurations mentioned above in presence of 5% random Gaussian noise. Γ_{zz}, pinpoints the target, and I at the target points delineates the dimensionality of the interfering spherical sources. One can see that the interference of the bodies distorts the I signature significantly in the vicinity of the targets. Nevertheless, I values are safe from this distortion exactly at the targets. It is deduced from Figure 7.4 that determination of the target points is of paramount importance, and I values farther from the target points can make significant errors in our methodology.

Table 7.2: Specifications of the interfering model 4 along with their respective solutions. Grid unit=0.1 m by 0.1 m, the model dimension and distances are in meter, and the radius of individual model 4's is 2meter.

Model	**GM** ($N.m^2.kg^{-1}$)	r_0(m)	**Noise=0**			**Noise=5%**		
			r_0^{est} (m)	I	NRMSE (%)	r_0^{est} (m)	I	NRMSE (%)
Three interfering Model 4, with equal densities and depths	1	(-5,-5, z_{COM}=3)	(-5, -5, 2.96)	0.97	0.60	(-4.9, -5.2, 2.39)	0.80	12.35
		(0, 0, z_{COM}= 3)	(0,0, 2.95)	0.92	0.90	(0, 0.1, 2.35)	0.72	12.55
		(5, 5, z_{COM}= 3)	(5, 5, 2.96)	0.97	0.6	(5.1, 4.9, 2.41)	0.76	11.58
Three interfering Model 4 With equal densities and different depths	1	(-5,-5, z_{COM}=3)	(-5, -5, 3.06)	0.99	1.17	(-5, -5, 2.53)	0.92	9.04
		(-5, 5, z_{COM}=2)	(-5, 5,1.99)	0.99	0.04	(-5.1, 5, 1.45)	0.73	16.09
		(5, 0, z_{COM}=4)	(5,0,4.03)	0.98	0.5	(4.8,0.3, 2.75)	0.78	18.69
Three interfering Model 4 with different densities and depths	1	(-5 -5,z_{COM}=3)	(-5, -5, 3.14)	0.99	2.74	(-5.1,-5.3, 2.22)	0.76	16.06
	1.5	(-5, 5,z_{COM}=2)	(-5, 5, 1.99)	0.99	0.07	(-5.2, 4.9, 1.49)	0.82	16.02
	2	(5, 0, z_{COM}=4)	(5, 0, 4.01)	0.99	0.23	(4.8, 0.2, 2.91)	0.82	16.2

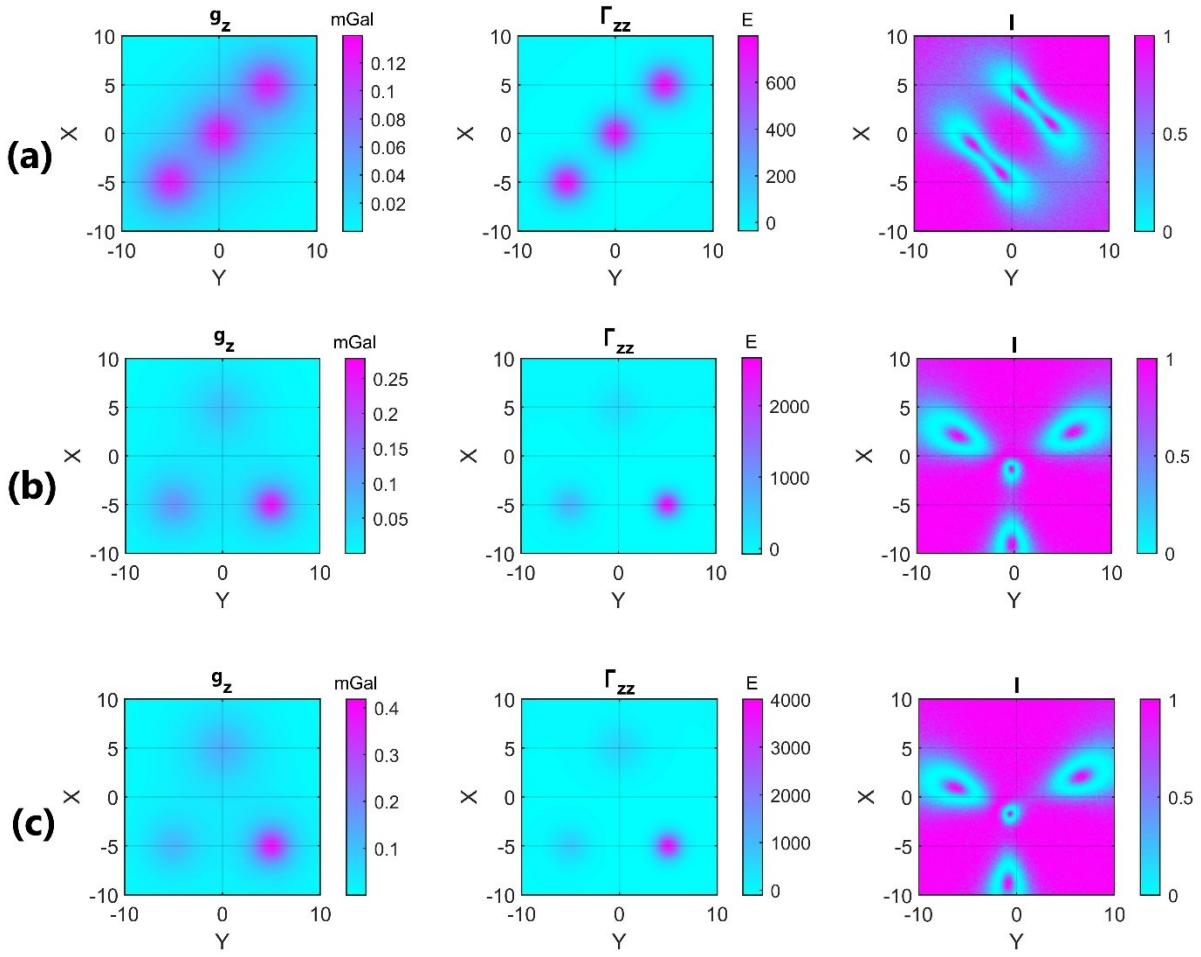

Figure 7.4: From left to right: g_z, Γ_{zz}, I in presence of 5% random Gaussian noise for (a) three interfering model 4 with equal densities (GM = 1 N.m^2.kg^{-1}) and depths (z_{COM} = 3 m); (b): three interfering model 4 with equal densities (GM = 1 N.m^2.kg^{-1}), but different depths (z_{COM} = 3, 2, 4m); and (c) three interfering model 4 with different densities (GM = 1, 1.5, 2 N.m^2.kg^{-1}) and different depths (z_{COM} = 3, 2, 4m). For more information about the models see Table 7.2.

7.3: Workflow

1. The gravity anomaly (g_z) and GGT components and invariants are calculated. Note that the units of g_z and Γ_{zz} are usually milligal and Eotvos, respectively. Therefore, they should be converted to their SI units for the subsequent analysis. 1milligal = 10^{-5} m/s^2 in SI, and 1 Eotvos =10^{-9} s^{-2} in SI.

2. The regional field should be eliminated from g_z. Usually, this could be done by subtraction of a fitting polynomial to g_z map, in xy plane. The order of the polynomial is set by the user.

3. For the target delineation in LOP-PP category, maximum of Γ_{zz} is marked.

4. For the target delineation in LOP-POP category, the points interiors of the causative body, far from the edges are used. The edges could be delineated from LTHG filter.

5. The dimensionality indicator ($I = -\frac{(I_2/2)^2}{(I_1/2)^3}$) is calculated for the target.

6. Based on the horizontal extent, derived from gravity parameters, in steps "3" and "4", either f_{LOP-PP} or $f_{LOP-POP}$ is considered at the target from equation (16) or (17).

7. From relations (18) or (19), the depth is calculated.

7.4: Application to real data

The efficiency of our proposed method was probed and compared with the Euler deconvolution method on the lunar surface. The calculation of the Bouguer anomaly involves considering a rock density of 2560 kg/m^3 pertaining to the upper crust[18,59]. To obtain the residual gravity field, we conducted a subtraction of a 3rd order polynomial, that was fitted to the Bouguer anomaly, from the Bouguer anomaly data itself. The choice of the fitted polynomial is subjective; usually, when the exploration area is large enough to comprise numerous positive and negative anomalous structures with an undulating and non-planar regional field trend, opting for higher orders, i.e., 2 or 3, of the polynomial yields a more realistic estimation of the individual anomalies.

Due to the abundance of impact craters on the Moon, its earliest history (~ the first 700 million years) is barely preserved[186]. However, the Bouguer anomaly and its derivatives with the employed resolution can reveal numerous subsurface structures. Andrew-Hanna *et al*. (2013)[18] identified a number of huge linear gravity anomalies as pre-Nectarian to Nectarian intrusive dike-like structures, which originate from both magmatism and lithospheric extension on the planet. In addition to the large-scale linear constructs, **Γ** components demonstrate some other structures that are related to impact basins, as well as composition and porosity variations over the lunar crust.

Figure 7.5 illustrates, from left to right, I, Γ_{zz}, and $\hat{z}_0$ overlain on the elevation map, for two regions on the Moon. I and Γ_{zz} in Figures 7.5a and 7.5b show enormous linear structures that are attributed with mafic igneous intrusions rising from the upper mantle with higher average density than their vicinities[18]. I in location of these structures is close to zero (indicating 2-dimensionality). Γ_{zz} depicts large linear values although this parameter in Figure 7.5a is much broader than in Figure 7.5b. The estimated solutions for these features could be credited to their top depth because of their likely large depth extent. We classified the depth solutions into 6 intervals from zero (over the reference ellipsoid) to 35 km. The average $\hat{z}_0$ is higher for the solutions occurring over the dike-like structures (> 10 km). This is more pronounced for Figure 7.5b, where the average depth to the top surface was estimated around 26 km by Andrew-Hanna *et al*. (2013)[18]. The solutions over the impact basins and other areas, having composition and/or porosity variation signatures, are shown to be shallower (< 10km). In case of large impact basins, this could be because of mantle upwarps and/or brecciation which occur nearer to the surface. However, in the case of small impact basins and areas with composition/porosity variations, the impact gardening, brecciation and superficial faulting and fracturing are more likely agents. As a result, it is reasonable for the solutions in these areas to be shallower. It is necessary to see if these solutions could be validated by other methodologies; Thus, we implemented the well-known Euler deconvolution method in the explored areas shown in Figure 7.5 to see if our solutions are consistent with them or not.

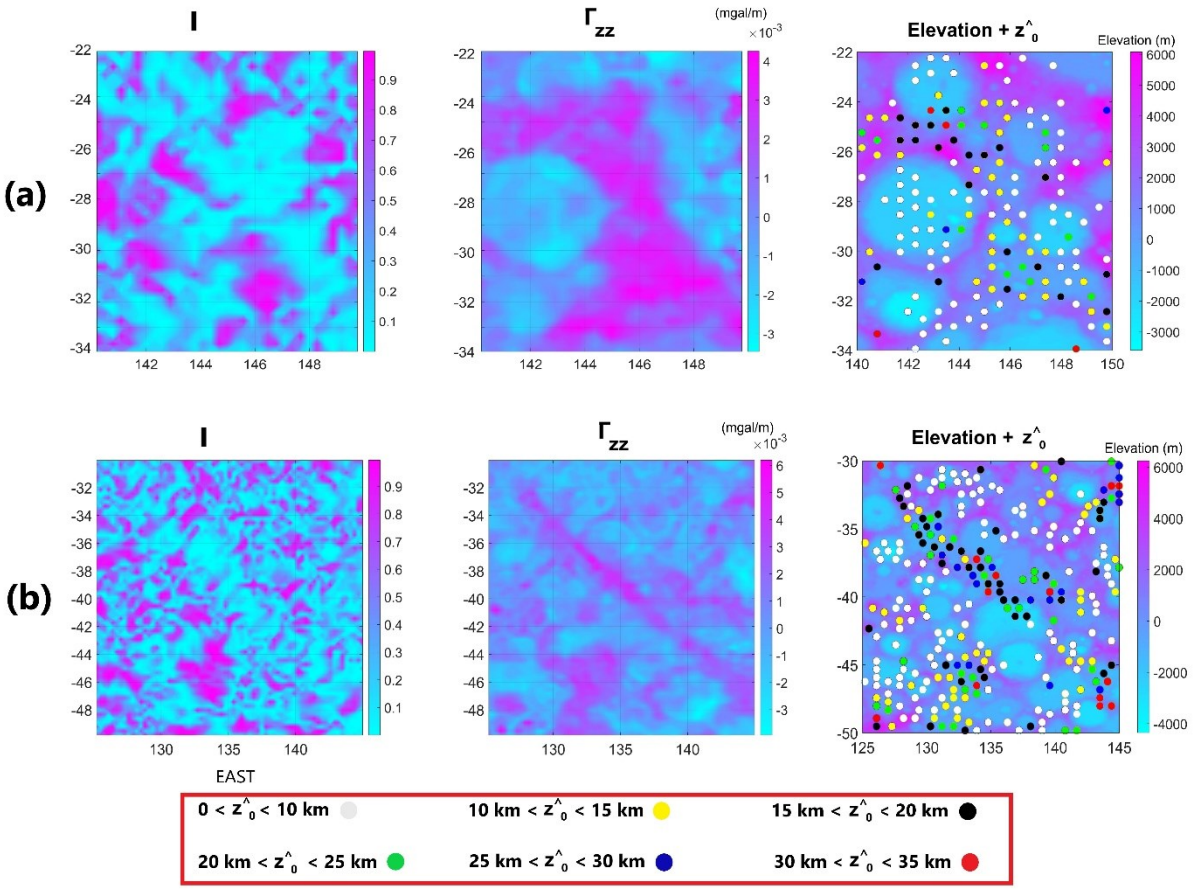

Figure 7.5: (a) and (b); from left to right; I, Γ_{zz}, and $\hat{z}_0$ fitted on elevation, for two regions on Moon.

7.4.1. Comparison with Euler deconvolution

Figures 7.6 (a) and (b) illustrate the depth estimations (z_{ED}) obtained using the Euler deconvolution method[28] with three different structural indices. From left to right, the structural indices are represented as SI=0.5, 1, and 2, corresponding to POP, LOP, and PP, respectively.

The Euler deconvolution technique is designed to examine three limiting cases (POP, LOP, and PP). Therefore, it is not feasible to employ varying structural indices within a single map. SI=0.5 sets the minimum depth range, and SI=2 determines the maximum depth range. The final solution for each area is chosen based on a priori geological information and the interpreter's judgment.

In this process, a sliding window of 30 km by 30 km, comprising 9 data points, was used. To enhance the reliability of the calculations, solutions with $z_{ED} < 10\ (SI)(\sigma_z)$ were discarded, as recommended by Thompson (1982)[28]. Here, σ_z represents the standard deviation of the estimated depth (z_{ED}), calculated from the covariance matrix of the estimated model parameters[187].

A comparison between Figures 7.5 and 7.6 confirms that our solutions fall within the depth ranges calculated by Euler deconvolution, which typically range from 0 to 35 km (see Figures 7.5 and 7.6). It is worth noting that Euler deconvolution provides only a rough estimate of the depth solutions due to the fixed nature of SI in its algorithm. In contrast, our method has the capability to distinguish between different SI values at each data point. Therefore, we believe that our method offers higher accuracy and reliability in depth estimation.

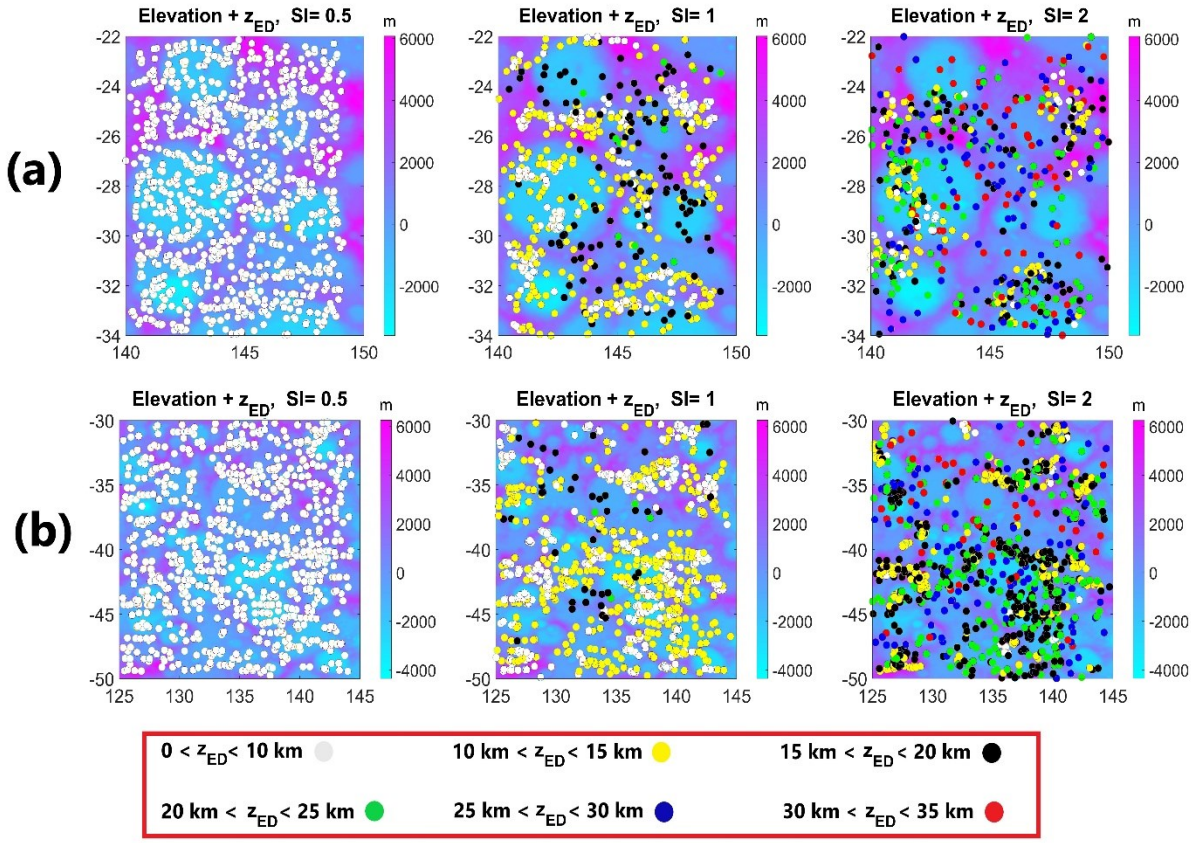

Figure 7.6: (a) and (b); depths attained from Euler Deconvolution method (z_{ED}) fitted on elevation for structural indices (SI) from left to right; 0.5, 1, and 2, for two regions on Moon.

7.5 Conclusion

We designed a novel method for detecting the depth of a causative body based on its relative horizontal dimensions, as indicated by the dimensionality indicator (I). The method categorizes causative bodies based on their horizontal spread, distinguishing between those falling within the line of poles and point pole (LOP-PP) category and those within the line of poles and plane of poles (LOP-POP) category, and introduces two types of solutions accordingly.

The introduced method estimates the depth of anomalous bodies with any dimensionality and, in limiting cases, becomes similar with the well-known Euler Deconvolution method. When the depth extent of a body is limited and small, the estimated depth ($\hat{z}_0$) corresponds to the center of mass, while for bodies with large depth extent, the $\hat{z}_0$ relates to the center of top surface.

The $\hat{z}_0$ is influenced by both the depth extent and the dimensionality of the causative body. As the depth extent increases, the impact of I on the estimated depth becomes more pronounced. Additionally, the behavior of $\hat{z}_0$ varies between the LOP-PP and LOP-POP categories, with LOP-POP solutions exhibiting lower errors for larger values of I.

The method is applied to defined synthetic isolated and interfering sources, both with and without noise. Once the stability of these solutions was achieved, we applied this method to lunar data that showed the presence of two significant linear structures. The results are aligned with the inferred geological information, validating the effectiveness of the approach.

Compared with some other techniques like Euler deconvolution method, our methodology presents more accurate estimates, and our solutions occur within those of Euler deconvolution which sets the upper and lower boundaries of the depth solutions. It requires fewer assumptions about the geology, i.e., limits assumptions to whether the gravity signal arises from a body within the LOP-PP category or the LOP-POP category. Additionally, to estimate the depth, only one data point is necessary. This new method can estimate the depth of anomalous causative bodies across a wide range of dimensionality from 2D to 3D.

Furthermore, our method, while straightforward, and not mathematically complicated provides a robust and efficient means for depth estimation of anomalous constructs, offering valuable insights into subsurface geology.

7.6 Data availability

The datasets generated and/or analysed during the present study are available in the [Planetary Data System (PDS)] repository, [https://pds-geosciences.wustl.edu/]. Matlab-based Graflab software was used for calculation of the Marussi tensor components.

Acknowledgement

The Authors thank Hakan Ucar for his comments on the paper. GK, and KK were partially supported from the Czech Science Foundation, grants 23-06075S.

Author contributions

K.K. wrote the main manuscript text, processed the data and prepared figures. G.K. wrote the main manuscript text.

Competing interests

The authors declare no competing interest.

Additional information

Correspondence and requests for materials should be addressed to K.K.

Reprints and permissions information is available at www.nature.com/reprints.

Publisher's note Springer Nature remains neutral with regard to jurisdictional claims in published maps and

institutional affiliations.

Chapter 8

Future Directions and New Research Areas Triggered by This Thesis

Gravity and magnetic aspects have great potential to be used in both planetary and engineering geophysics. Regarding planetary applications, these functionals could be exercised on other planets like Jupiter and Mars. Although the current resolution of the gravity field model of Mars, Venus and Jupiter is low compared to Earth and Moon, their gravity aspects are inspiring. Additionally, when higher degrees and orders of the spherical harmonic functions become available through future planetary missions, the zones studied previously could be reexamined for more detailed investigations. Furthermore, increasing degrees and orders of the harmonic functions reveal new geological features that are visible in neither their current gravity models nor geological observations. For example, these potential field parameters could be employed for the detection of unexplored buried impact craters that are not observable through geological studies alone. Volcanic activities and variations in crustal thickness are also among the features that could be deciphered through potential field investigations. One new feature that is especially emphasized in this thesis is specifying the deformational level, strain-stress condition, and structural weaknesses through SA and CF. Some potential research objectives raised by this study are:

- Detection of buried impact craters on rocky planets.
- Examination of the activity stages of volcanic features.
- Examination of the existence of megaplumes on the northern hemisphere of Mars compared with its southern hemisphere.
- Investigation of deformational level and existence of structural weakness on Mars.

References

1. Blakely, R. J. *Potential Theory in Gravity and Magnetic Applications*. (Cambridge University Press, Cambridge, 1995). doi:10.1017/CBO9780511549816.
2. Heiskanen, W. A. & Moritz, H. Physical geodesy. *Bull. Geodesique* **86**, 491–492 (1967).
3. Lowrie, W. *Fundamentals of Geophysics*. (Cambridge University Press, Cambridge, 2007). doi:10.1017/CBO9780511807107.
4. Telford, W. M., Geldart, L. P. & Sheriff, R. E. *Applied Geophysics*. (Cambridge University Press, 1990).
5. Beiki, M. & Pedersen, L. B. Eigenvector analysis of gravity gradient tensor to locate geologic bodies. *Geophysics* **75**, I37–I49 (2010).
6. Blakely, R. J. & Simpson, R. W. Approximating edges of source bodies from magnetic or gravity anomalies. *Geophysics* **51**, 1494–1498 (1986).
7. Bott, M. H. P. & Smith, R. A. The estimation of the limiting depth of the gravitating bodies. *Geophysical Prospecting* **6**, 1–10 (1958).
8. Edwards, A. J., Maki, J. T. & Peterson, D. G. Gravity Gradiometry as a Tool for Underground Facility Detection. *JEEG* **2**, 137–142 (1997).
9. Hansen, R. O. & Simmonds, M. Multiple-source Werner deconvolution. *Geophysics* **58**, 1792–1800 (1993).
10. Jacobsen, B. H. A case for upward continuation as a standard separation filter for potential-field maps. *GEOPHYSICS* **52**, 1138–1148 (1987).
11. Karimi, K., Shirzaditabar, F., Amirian, A. & Mansoobi, A. Center of Mass estimation of simple shaped magnetic bodies using eigenvectors of Computed Magnetic Gradient Tensor. *JESP* (2019) doi:10.22059/jesphys.2019.256185.1006999.
12. Karimi, K., Oveisy Moakhar, M. & Shirzaditabar, F. Location and dimensionality estimation of geological bodies using eigenvectors of gravity gradient tensor. **44**, 63–71 (2018).

13. Pedersen, L. B. & Rasmussen, T. M. The gradient tensor of potential field anomalies: Some implications on data collection and data processing of maps. *GEOPHYSICS* **55**, 1558–1566 (1990).
14. Peters, L. J. The direct approach to magnetic interpretation and its practical application. *Geophysics* **14**, 290–320 (1949).
15. Pilkington, M., Hildebrand, A. R. & Ortiz-Aleman, C. Gravity and magnetic field modeling and structure of the Chicxulub Crater, Mexico. *Journal of Geophysical Research: Planets* **99**, 13147–13162 (1994).
16. Saad, A. H. Understanding gravity gradients—a tutorial. *The Leading Edge* **25**, 942–949 (2006).
17. Andrews-Hanna, J., et all. Gravity gradients of Venus, 47th Lunar and Planetary Science Conference. in (2016).
18. Andrews-Hanna, J. C. *et al.* Ancient Igneous Intrusions and Early Expansion of the Moon Revealed by GRAIL Gravity Gradiometry. *Science* **339**, 675–678 (2013).
19. Harris, L. & Bédard, J. Crustal evolution and deformation in a non-plate tectonic Archaean Earth: Comparisons with Venus. In: Dilek Y, Furnes H (Eds), Evolution of Archean Crust and Early Life, Modern Approaches in Solid Earth Sciences 7, Springer, Chapter 9, 215-288. ISBN 978-94-007-7614-2 & ISBN 978-94-007-7615-9 (eBook). in 215–288 (2014). doi:10.1007/978-94-007-7615-9_9.
20. Harris, L. B. & Bédard, J. H. Interactions between continent-like 'drift', rifting and mantle flow on Venus: gravity interpretations and Earth analogues. *Geological Society of London Special Publications* **401**, 327–356 (2015).
21. Klokočník, J., Kostelecký, J., Cílek, V. & Bezděk, A. *Subglacial and underground structures detected from recent gravito-topography data*. (Cambridge scholars publishing, Newcastle upon Tyne, 2020).

22. Klokočník, J., Kostelecký, J., Kalvoda, J., Eppelbaum, L. V. & Bezděk, A. Gravity Disturbances, Marussi Tensor, Invariants and Other Functions of the Geopotential Represented by EGM 2008. *JESR* 88–101 (2014) doi:10.18005/JESR0203003.
23. Wieczorek, M. A. Gravity and Topography of the Terrestrial Planets. in *Treatise on Geophysics: Second Edition* 153–193 (2015). doi:10.1016/B978-0-444-53802-4.00169-X.
24. Wieczorek, M. A. *et al*. The Crust of the Moon as Seen by GRAIL. *Science* **339**, 671–675 (2013).
25. Fowler, C. M. R. *The Solid Earth: An Introduction to Global Geophysics*. (Cambridge University Press, Cambridge, 2005).
26. Parasnis, D. S. *Principles of Applied Geophysics*. (Springer, London, 1996).
27. Hofmann-Wellenhof, B. & Moritz, H. *Physical Geodesy*. (SpringerWienNewYork, Wien, 2006).
28. Thompson, D. T. EULDPH: A new technique for making computer-assisted depth estimates from magnetic data. *Geophysics* **47**, 31–37 (1982).
29. Reid, A. B., Allsop, J. M., Granser, E. L., Millett, A. J. & Somerton, I. W. Magnetic interpretation in three dimensions using Euler deconvolution. *Geophysics* **55**, 80–91 (1990).
30. Beiki, M., Pedersen, L. & Nazi, H. Interpretation of aeromagnetic data using eigenvector analysis of pseudogravity gradient tensor. *Geophysics* **76**, (2011).
31. Karimi, K. & Shirzaditabar, F. Using the ratio of the magnetic field to the analytic signal of the magnetic gradient tensor in determining the position of simple shaped magnetic anomalies. *J. Geophys. Eng.* **14**, 769–779 (2017).
32. Klokocnik, J., Kostelecký, J., Bezdek, A. & Kletetschka, G. Gravity strike angles: A modern approach and tool to estimate the direction of impactors of meteoritic craters. *Planetary and Space Science* **194**, 105113 (2020).

33. Klokočník, J., Kostelecký, J., Cílek, V., Kletetschka, G. & Bezděk, A. Gravity aspects from recent gravity field model GRGM1200A of the Moon and analysis of magnetic data. *Icarus* **384**, 115086 (2022).

34. Klokočník, J., Kostelecký, J., Bezděk, A., Kletetschka, G. & Staňková, H. A 200 km suspected impact crater Kotuykanskaya near Popigai, Siberia, in the light of new gravity aspects from EIGEN 6C4, and other data. *Sci Rep* **10**, 6093 (2020).

35. Klokočník, J., Kostelecký, J., Varadzinová, L., Bezděk, A. & Kletetschka, G. A Gravity Search for Oil and Gas and Groundwater in Egypt Using the Strike Angles Derived from EIGEN 6C4. *Applied Sciences* **10**, 8950 (2020).

36. Klokočník, J., Kostelecký, J., Cílek, V., Bezděk, A. & Pešek, I. A support for the existence of paleolakes and paleorivers buried under Saharan sand by means of "gravitational signal" from EIGEN 6C4. *Arab J Geosci* **10**, 199 (2017).

37. Pham, L. T. *et al.* An improved approach for detecting ridge locations to interpret the potential field data for more accurate structural mapping: A case study from Vredefort dome area (South Africa). *Journal of African Earth Sciences* **175**, 104099 (2021).

38. Mikhailov, V. G., Pajot, G., Diament, M. & Price, A. Tensor deconvolution: A method to locate equivalent sources from full tensor gravity data. *Geophysics* **72**, 161–169 (2007).

39. Pham, L. T., Oksum, E. & Do, T. D. Edge enhancement of potential field data using the logistic function and the total horizontal gradient. *Acta Geod Geophys* **54**, 143–155 (2019).

40. Yuan, Y. *et al.* Depth estimation of potential field sources by using improved Chebyshev-Padé downward continuation in wave number domain. *Earth and Space Science* **7**, (2020).

41. Zhang, C., Mushayandebvu, M. F., Reid, A. B., Fairhead, J. D. & Odegard, M. Euler deconvolution of gravity tensor gradient data. *Geophysics* **65**, 512–520 (2000).

42. Zhou, W. Normalized full gradient of full tensor gravity gradient based on adaptive iterative Tikhonov regularization downward continuation. *Journal of Applied Geophysics* **118**, 75–83 (2015).

43. Zhou, W. N., Zhang, C. & Zhang, D. L. Depth estimation of potential fi eld by using a new downward continuation based on the continued fraction in space domain. *Earth and Space Science* **8**, (2021).

44. Zuo, B., Kass, M. A., Hu, X. & Geng, M. Full-tensor gravity gradient eigenvector analysis for locating complex geological source positions. *Nonlin. Processes Geophys* (2017) doi:https://doi.org/10.5194/npg-2016-75, 2017.

45. Kalvoda, J., Klokočník, J. & Kostelecký, J. Regional correlation of the Earth Gravitational Model 08 with morphogenetic patterns of the Nepal Himalaya. *AUC GEOGRAPHICA* **45**, 53–71 (2021).

46. Mizera, J. *et al.* Parent crater for Australasian tektites beneath the sands of the Alashan Desert, Northwest China: Best candidate ever? in *In the Footsteps of Warren B. Hamilton: New Ideas in Earth Science* (eds. Foulger, G. R. et al.) vol. 553 0 (Geological Society of America, 2022).

47. Connerney, J. E. P. *et al.* The global magnetic field of Mars and implications for crustal evolution. *Geophysical Research Letters* **28**, 4015–4018 (2001).

48. McKenzie, D. The Relationship between Topography and Gravity on Earth and Venus. *Icarus* **112**, 55–88 (1994).

49. Watts, A. B. *Isostasy and Flexure of the Lithosphere*. (Cambridge University Press, 2001).

50. Mataragio, J. & Kieley, J. Application of full tensor gradient invariants in detection of intrusion-hosted sulphide mineralization: implications for deposition mechanisms. (2009) doi:https://doi.org/10.3997/1365-2397.27.1301.29032.

51. Zengerer, M. An Overview of Tensors, Gradient and Invariant Products in Imaging and Qualitative Interpretation. *ASEG Extended Abstracts* **2018**, 1–8 (2018).

52. Miller, H. G. & Singh, V. Potential field tilt—a new concept for location of potential field sources. *Journal of Applied Geophysics* **32**, 213–217 (1994).

53. Kletetschka, G. *et al.* Distribution of water phase near the poles of the Moon from gravity aspects. *Sci Rep* **12**, 4501 (2022).

54. Karimi, K., Kletetschka, G. & Meier, V. Comparison between the geological features of Venus and Earth based on gravity aspects. *Sci Rep* **13**, 12259 (2023).

55. Karimi, K., Kletetschka, G., Mizera, J., Meier, V. & Strunga, V. Formation of Australasian tektites from gravity and magnetic indicators. *Sci Rep* **13**, 12868 (2023).

56. Plado, J. Gravity and magnetic signatures of meteorite impact structures. (Tartu : Tartu Ülikooli Kirjastus, 2000).

57. Karimi, K. & Kletetschka, G. Subsurface geology detection from application of the gravity-related dimensionality constraint. *Sci Rep* **14**, 2440 (2024).

58. Lemoine, F. G. *et al.* GRGM900C: A degree 900 lunar gravity model from GRAIL primary and extended mission data. *Geophysical Research Letters* **41**, 3382–3389 (2014).

59. Bucha, B., Hirt, C. & Kuhn, M. Divergence-free spherical harmonic gravity field modelling based on the Runge–Krarup theorem: a case study for the Moon. *J Geod* **93**, 489–513 (2019).

60. Barker, M. K. *et al.* A new lunar digital elevation model from the Lunar Orbiter Laser Altimeter and SELENE Terrain Camera. *Elsevier* (2015).

61. Smith, D. E. *et al.* The Lunar Orbiter Laser Altimeter Investigation on the Lunar Reconnaissance Orbiter Mission. *Space Sci Rev* **150**, 209–241 (2010).

62. Ince, E. S. *et al.* ICGEM – 15 years of successful collection and distribution of global gravitational models, associated services, and future plans. *Earth System Science Data* **11**, 647–674 (2019).

63. Amante, C. & Eakins, B. W. ETOPO1 arc-minute global relief model : procedures, data sources and analysis. https://repository.library.noaa.gov/view/noaa/1163.

64. Maus, S. *et al.* EMAG2: A 2–arc min resolution Earth Magnetic Anomaly Grid compiled from satellite, airborne, and marine magnetic measurements. *Geochemistry, Geophysics, Geosystems* **10**, (2009).

65. Konopliv, A. S., Banerdt, W. B. & Sjogren, W. L. Venus Gravity: 180th Degree and Order Model. *Icarus* **139**, 3–18 (1999).

66. Smrekar, S. E. et al. VERITAS (Venus Emissivity, Radio science, INSAR, Topography And Spectroscopy): a proposed discovery mission. *abstract No. 1449. 51st Lunar and Planetary Science Conference* (2020).

67. pds-geosciences.wustl.edu - /mgn/mgn-v-rss-5-gravity-l2-v1/mg_5201/topo/. https://pds-geosciences.wustl.edu/mgn/mgn-v-rss-5-gravity-l2-v1/mg_5201/topo/.

68. Bucha, B. & Janák, J. A MATLAB-based graphical user interface program for computing functionals of the geopotential up to ultra-high degrees and orders. *Computers & Geosciences* **56**, 186–196 (2013).

69. Nabighian, M. N. Toward a three-dimensional automatic interpretation of potential field data via generalized Hilbert transforms: Fundamental relations. *GEOPHYSICS* **49**, 780–786 (1984).

70. Tsunakawa, H., Takahashi, F., Shimizu, H., Shibuya, H. & Matsushima, M. Surface vector mapping of magnetic anomalies over the Moon using Kaguya and Lunar Prospector observations. *Journal of Geophysical Research: Planets* **120**, 1160–1185 (2015).

71. Smith, R. M., Gates, M., Cassady, A. & Krezel, J. An overview of NASA's exploration mission 2 (EM-2). in *2018 IEEE Aerospace Conference* 1–11 (IEEE, Big Sky, MT, USA, 2018). doi:10.1109/AERO.2018.8396585.

72. Terada, K. *et al.* Biogenic oxygen from Earth transported to the Moon by a wind of magnetospheric ions. *Nat Astron* **1**, 1–5 (2017).

73. Zanna, G. D., Dere, K. P., Young, P. R., Landi, E. & Mason, H. E. CHIANTI – An atomic database for emission lines. Version 8. *A&A* **582**, A56 (2015).

74. Wang, H. Z. *et al.* Earth Wind as a Possible Exogenous Source of Lunar Surface Hydration. *ApJL* **907**, L32 (2021).

75. Seki, K., Elphic, R. C., Hirahara, M., Terasawa, T. & Mukai, T. On Atmospheric Loss of Oxygen Ions from Earth Through Magnetospheric Processes. *Science* **291**, 1939–1941 (2001).

76. Kletetschka, G. *et al.* Magnetic zones of Mars: Deformation-controlled origin of magnetic anomalies. *Meteoritics & Planetary Science* **44**, 131–140 (2009).

77. Harada, Y. *et al.* Marsward and tailward ions in the near-Mars magnetotail: MAVEN observations. *Geophysical Research Letters* **42**, 8925–8932 (2015).

78. Kahn, P. G. K. & Pompea, S. M. Nautiloid growth rhythms and dynamical evolution of the Earth–Moon system. *Nature* **275**, 606–611 (1978).

79. Jakosky, B. M. *et al.* MAVEN observations of the response of Mars to an interplanetary coronal mass ejection. *Science* **350**, aad0210 (2015).

80. Ozima, M. *et al.* Terrestrial nitrogen and noble gases in lunar soils. *Nature* **436**, 655–659 (2005).

81. Shizgal, B. D. & Arkos, G. G. Nonthermal escape of the atmospheres of Venus, Earth, and Mars. *Reviews of Geophysics* **34**, 483–505 (1996).

82. Angelopoulos, V. *et al.* Electromagnetic Energy Conversion at Reconnection Fronts. *Science* **341**, 1478–1482 (2013).

83. Walker, I. K., Moen, J., Mitchell, C. N., Kersley, L. & Sandholt, P. E. Ionospheric effects of magnetopause reconnection observed using ionospheric tomography. *Geophysical Research Letters* **25**, 293–296 (1998).

84. Hultqvist, B., Øieroset, M., Paschmann, G. & Treumann, R. A. Processes leading to plasma losses into the high-latitude atmosphere. in *Magnetospheric Plasma Sources and Losses: Final Report of the ISSI Study Project on Source and Loss Processes* (eds. Hultqvist, B.,

Øieroset, M., Paschmann, G. & Treumann, R. A.) 85–135 (Springer Netherlands, Dordrecht, 1999). doi:10.1007/978-94-011-4477-3_3.

85. Wilson, J. K., Mendillo, M. & Spence, H. E. Magnetospheric influence on the Moon's exosphere. *Journal of Geophysical Research: Space Physics* **111**, (2006).
86. Mishra, S. K. & Bhardwaj, A. Electrostatic charging of permanently shadowed craters on the Moon. *Monthly Notices of the Royal Astronomical Society: Letters* **496**, L80–L84 (2020).
87. Piquette, M. & Horányi, M. The effect of asymmetric surface topography on dust dynamics on airless bodies. *Icarus* **C**, 65–74 (2017).
88. Stubbs, T. J., Vondrak, R. R. & Farrel, W. M. in Moon and Near-Earth Objects. *Advances in Space Research (eds P. Ehrenfreund et al.) 59–66 (Elsevier Science Bv, 2006)* **37**,.
89. Carroll, A. *et al.* Laboratory measurements of initial launch velocities of electrostatically lofted dust on airless planetary bodies. *Icarus* **352**, 113972 (2020).
90. Colwell, J. E., Gulbis, A. A., Horányi, M. & Robertson, S. Dust transport in photoelectron layers and the formation of dust ponds on Eros. *Icarus* **175**, 159–169 (2005).
91. Hughes, A. L. H., Colwell, J. E. & DeWolfe, A. W. Electrostatic dust transport on Eros: 3-D simulations of pond formation. *Icarus* **195**, 630–648 (2008).
92. Robinson, M. S., Thomas, P. C., Veverka, J., Murchie, S. & Carcich, B. The nature of ponded deposits on Eros. *Nature* **413**, 396–400 (2001).
93. Thomas, N. *et al.* Redistribution of particles across the nucleus of comet 67P/Churyumov-Gerasimenko. *A&A* **583**, A17 (2015).
94. Russell, C. T. & Angelopoulos, V. Foreword. *Space Sci Rev* **165**, 1–2 (2011).
95. Studinger, M., Bell, R. E. & Tikku, A. A. Estimating the depth and shape of subglacial Lake Vostok's water cavity from aerogravity data. *Geophysical Research Letters* **31**, (2004).
96. Zhao, S. *et al.* Statistical study of magnetotail flux ropes near the lunar orbit. *Sci. China Technol. Sci.* **59**, 1591–1596 (2016).

97. Greenwood, J. P. *et al.* Hydrogen isotope ratios in lunar rocks indicate delivery of cometary water to the Moon. *Nature Geosci* **4**, 79–82 (2011).

98. Saal, A. E. *et al.* Volatile content of lunar volcanic glasses and the presence of water in the Moon's interior. *Nature* **454**, 192–195 (2008).

99. Clark, R. N. Detection of Adsorbed Water and Hydroxyl on the Moon. *Science* **326**, 562–564 (2009).

100. Mitrofanov, I. *et al.* Testing polar spots of water-rich permafrost on the Moon: LEND observations onboard LRO. *Journal of Geophysical Research: Planets* **117**, (2012).

101. Ogino, T., Kobayashi, T., Takahashi, T. & Kanamori, H. Velocity Profiles in the Shallow Lunar Subsurface Deduced from Laboratory Measurements with Simulants. *Journal of Aerospace Engineering* **29**, 04016039 (2016).

102. Hayne, P. O. *et al.* Global Regolith Thermophysical Properties of the Moon From the Diviner Lunar Radiometer Experiment. *Journal of Geophysical Research: Planets* **122**, 2371–2400 (2017).

103. Konopliv, A. S. *et al.* High-resolution lunar gravity fields from the GRAIL Primary and Extended Missions. *Geophysical Research Letters* **41**, 1452–1458 (2014).

104. Honniball, C. I. *et al.* Molecular water detected on the sunlit Moon by SOFIA. *Nat Astron* **5**, 121–127 (2021).

105. Kenkmann, T., Poelchau, M. H. & Wulf, G. Structural geology of impact craters. *Journal of Structural Geology* **62**, 156–182 (2014).

106. Collins, G. S., Melosh, H. J., Morgan, J. V. & Warner, M. R. Hydrocode Simulations of Chicxulub Crater Collapse and Peak-Ring Formation. *Icarus* **157**, 24–33 (2002).

107. Kletetschka, G., Ocampo Uria, A., Zila, V. & Elbra, T. Electric discharge evidence found in a new class of material in the Chicxulub ejecta. *Sci Rep* **10**, 9035 (2020).

108. Masaitis, V. L. Morphological, structural and lithological records of terrestrial impacts: an overview. *Australian Journal of Earth Sciences* **52**, 509–528 (2005).

109. Mangold, N., Adeli, S., Conway, S., Ansan, V. & Langlais, B. A chronology of early Mars climatic evolution from impact crater degradation. *Journal of Geophysical Research: Planets* **117**, (2012).

110. Senft, L. E. & Stewart, S. T. Dynamic fault weakening and the formation of large impact craters. *Earth and Planetary Science Letters* **287**, 471–482 (2009).

111. Wieczorek, M. A., Weiss, B. P. & Stewart, S. T. An Impactor Origin for Lunar Magnetic Anomalies. *Science* **335**, 1212–1215 (2012).

112. Hayne, P. O. *et al.* Evidence for exposed water ice in the Moon's south polar regions from Lunar Reconnaissance Orbiter ultraviolet albedo and temperature measurements. *Icarus* **255**, 58–69 (2015).

113. Lucey, P. G. The Poles of the Moon. *Elements* **5**, 41–46 (2009).

114. Zhu, C. *et al.* Untangling the formation and liberation of water in the lunar regolith. *Proceedings of the National Academy of Sciences* **116**, 11165–11170 (2019).

115. Angelopoulos, V. The ARTEMIS Mission. *Space Sci Rev* **165**, 3–25 (2011).

116. Andrews-Hanna, J. C. *et al.* Ancient igneous intrusions and early expansion of the Moon revealed by GRAIL gravity gradiometry. *Science* **339**, 675–678 (2013).

117. Murphy, A. & Dickinson, J. L. Exploring Exploration Play Models with FTG Gravity Data. *European Association of Geoscientists & Engineers* (2009) doi:https://doi.org/10.3997/2214-4609-pdb.241.murphy_paper1.

118. Pajot, G., de Viron, O., Diament, M., Lequentrec-Lalancette, M.-F. & Mikhailov, V. Noise reduction through joint processing of gravity and gravity gradient data. *GEOPHYSICS* **73**, I23–I34 (2008).

119. Head, J. W. The geologic evolution of Venus: Insights into Earth history. *Geology* **42**, 95–96 (2014).

120. Bickford, M. The Web of Geological Sciences: Advances, Impacts, and Interactions. (2013).

121. Davis, A. M. *Meteorites, Comets, and Planets: Treatise on Geochemistry, Second Edition, Volume 1*. (Elsevier Science, 2005).
122. Treiman, A. H. Geochemistry of Venus' Surface: Current Limitations as Future Opportunities. in *Exploring Venus as a Terrestrial Planet* 7–22 (American Geophysical Union (AGU), 2007). doi:10.1029/176GM03.
123. McKinnon, W. B., Zahnle, K. J., Ivanov, B. A. & Melosh, H. J. *Cratering on Venus: Models and Observations*. 969 (1997).
124. Namiki, N. & Solomon, S. C. Impact crater densities on volcanoes and coronae on venus: implications for volcanic resurfacing. *Science* **265**, 929–933 (1994).
125. Solomatov, V. & Moresi, L. Stagnant lid convection on Venus. *Journal of Geophysical Research* **101**, 4737–4754 (1996).
126. James, P. B., Zuber, M. T. & Phillips, R. J. Crustal thickness and support of topography on Venus. *Journal of Geophysical Research: Planets* **118**, 859–875 (2013).
127. Bindschadler, D. L., Schubert, G. & Kaula, W. M. Coldspots and hotspots: Global tectonics and mantle dynamics of Venus. *Journal of Geophysical Research* **97**, 13495–13532 (1992).
128. Ivanov, M. & Head, J. Tessera Terrain on Venus: A Survey of the Global Distribution, Characteristics, and Relation to Surrounding Units from Magellan Data. *J. Geophys. Res.* **101**, (1996).
129. Phillips, R. & Hansen, V. Geological Evolution of Venus: Rises, Plains, Plumes, and Plateaus. *Science* **279**, 1492–1497 (1998).
130. Ivanov, M. A. & Head, J. W. Formation and evolution of Lakshmi Planum, Venus: Assessment of models using observations from geological mapping. *Planetary and Space Science* **56**, 1949–1966 (2008).
131. Weller, M. & Kiefer, W. The Physics of Changing Tectonic Regimes: Implications for the Temporal Evolution of Mantle Convection and the Thermal History of Venus. *Journal of Geophysical Research: Planets* **125**, (2020).

132. Schubert, G., Turcotte, D. L. & Olson, P. *Mantle Convection in the Earth and Planets*. (Cambridge University Press, 2001).
133. Head, III, Peterfreund, A., Garvin, J. & Zisk, S. Surface characteristics of Venus derived from Pioneer Venus altimetry, roughness, and reflectivity measurements. *Journal of Geophysical Research* **90**, (1985).
134. STOFAN, E. R. *et al.* Geology of a rift zone on Venus: Beta Regio and Devana Chasma. *GSA Bulletin* **101**, 143–156 (1989).
135. Basilevsky, A. & Head, J. Beta Regio, Venus: Evidence for uplift, rifting, and volcanism due to a mantle plume. *Icarus* **192**, 167–186 (2007).
136. Stofan, E., Smrekar, S., Bindschadler, D. & Senske, D. Large Topographic Rises on Venus: Implications for Mantle Upwelling. *Journal of Geophysical Research* **100**, (1995).
137. Guseva, E. N. Classification of the rift zones of venus: Rift valleys and graben belts. *Solar System Research* **50**, 184–196 (2016).
138. Ivanov, M. & Head, J. The history of tectonism on Venus: A stratigraphic analysis. *Planetary and Space Science* **113–114**, (2015).
139. Smrekar, S., Kiefer, W. & Stofan, E. Large Volcanic Rises on Venus. (1997).
140. O'Rourke, J. G. & Smrekar, S. E. Signatures of Lithospheric Flexure and Elevated Heat Flow in Stereo Topography at Coronae on Venus. *Journal of Geophysical Research: Planets* **123**, 369–389 (2018).
141. Grimm, R. E. & Phillips, R. J. Anatomy of a Venusian Hot Spot: Geology, Gravity, and Mantle Dynamics of Eistla Regio. *Journal of Geophysical Research* **97**, 16035–16054 (1992).
142. Gilmore, M. S. & Head, J. W. Morphology and deformational history of Tellus Regio, Venus: Evidence for assembly and collision. *Planetary and Space Science* **154**, 5–20 (2018).
143. Byrne, P. K. *et al.* A globally fragmented and mobile lithosphere on Venus. *Proceedings of the National Academy of Sciences* **118**, e2025919118 (2021).

144. Mussett, A. E., Khan, M. A. & Button, S. Looking into the Earth: An Introduction to Geological Geophysics. *Higher Education from Cambridge University Press* https://www.cambridge.org/highereducation/books/looking-into-the-earth/F46E6696F2CA6B8BA193E1D29F4FBB99 (2000) doi:10.1017/CBO9780511810305.

145. Grimm, R. E. & Phillips, R. J. Tectonics of Lakshmi Planum, Venus: Tests for Magellan. *Geophysical Research Letters* **17**, 1349–1352 (1990).

146. Ansan, V., Vergely, P. & Masson, Ph. Model of formation of Ishtar Terra, Venus. *Planetary and Space Science* **44**, 817–831 (1996).

147. Bindschadler, D. L., Schubert, G. & Kaula, W. M. Mantle flow tectonics and the origin of Ishtar Terra, Venus. *Geophysical Research Letters* **17**, 1345–1348 (1990).

148. Senske, D. A., Head, J. W., Stofan, E. R. & Campbell, D. B. Geology and structure of Beta Regio, Venus: Results from Arecibo Radar Imaging. *Geophysical Research Letters* **18**, 1159–1162 (1991).

149. Kiefer, W. S. & Swafford, L. C. Topographic analysis of Devana Chasma, Venus: implications for rift system segmentation and propagation. *Journal of Structural Geology* **28**, 2144–2155 (2006).

150. Vezolainen, A., Solomatov, V., Basilevsky, A. & Head, J. Uplift of Beta Regio: Three-dimensional models. *Journal of Geophysical Research (Planets)* **109**, 8007 (2004).

151. Koeberl, C. *et al.* Tektite glasses from Belize, Central America: Petrography, geochemistry, and search for a possible meteoritic component. *Geochimica et Cosmochimica Acta* **325**, 232–257 (2022).

152. Mizera, J., Řanda, Z. & Kameník, J. On a possible parent crater for Australasian tektites: Geochemical, isotopic, geographical and other constraints. *Earth-Science Reviews* **154**, 123–137 (2016).

153. Rochette, P. *et al.* Impact glasses from Belize represent tektites from the Pleistocene Pantasma impact crater in Nicaragua. *Commun Earth Environ* **2**, 1–8 (2021).

154. Stauffer, P. H. Anatomy of the Australasian tektite strewnfield and the probable site of its source crater. in 285–289 (1978).
155. Mizera, J. Quest for the Australasian impact crater: Failings of the candidate location at the Bolaven Plateau, Southern Laos. *Meteoritics & Planetary Science* **57**, 1973–1986 (2022).
156. Sieh, K. *et al.* Australasian impact crater buried under the Bolaven volcanic field, Southern Laos. *Proceedings of the National Academy of Sciences* **117**, 1346–1353 (2020).
157. Hawke, P. J., Buckingham, A. J. & Dentith, M. C. Modelling Source Depth and Possible Origin of Magnetic Anomalies Associated with the Yallalie Impact Structure, Perth Basin, Western Australia. *Exploration Geophysics* **37**, 191–196 (2006).
158. Saada, S. A., Mickus, K., Eldosouky, A. M. & Ibrahim, A. Insights on the tectonic styles of the Red Sea rift using gravity and magnetic data. *Marine and Petroleum Geology* **133**, 105253 (2021).
159. Hamimi, Z., Eldosouky, A. M., Hagag, W. & Kamh, S. Z. Large-scale geological structures of the Egyptian Nubian Shield. *Sci Rep* **13**, 1923 (2023).
160. Urrutia-Fucugauchi, J., Arellano-Catalán, O., Pérez-Cruz, L. & Romero-Galindo, I. A. Chicxulub Crater Joint Gravity and Magnetic Anomaly Analysis: Structure, Asymmetries, Impact Trajectory and Target Structures. *Pure Appl. Geophys.* **179**, 2735–2756 (2022).
161. Yang, X. *et al.* Formation of the highest sand dunes on Earth. *Geomorphology* **135**, 108–116 (2011).
162. Wang, F. *et al.* Formation and evolution of the Badain Jaran Desert, North China, as revealed by a drill core from the desert centre and by geological survey. *Palaeogeography, Palaeoclimatology, Palaeoecology* **426**, 139–158 (2015).
163. Du, J. *et al.* Cenozoic tectono-geomorphic evolution of Yabrai Mountain and the Badain Jaran Desert (NE Tibetan Plateau margin). *Geomorphology* **389**, 107857 (2021).
164. IKCEST. https://www.ikcest.org/index.htm.

165. Wang, Z. *et al.* Groundwater characteristics and climate and ecological evolution in the Badain Jaran Desert in the southwest Mongolian Plateau. *zgdzyw* **4**, 421–432 (2021).
166. Wang, X.-S. & Zhou, Y. Investigating the mysteries of groundwater in the Badain Jaran Desert, China. *Hydrogeol J* **26**, 1639–1655 (2018).
167. Dai, D., Cao, J., Lai, P. & Wu, Z. TEM study on particles transported by ascending gas flow in the Kaxiutata iron deposit, Inner Mongolia, North China. *Geochemistry: Exploration, Environment, Analysis* **15**, 255–271 (2015).
168. Mindat.org,. . Gaxun Tal Mine (Kaxiutata Mine).
169. Pilkington, M., Hildebrand, A. R. & Ortiz-Aleman, C. Gravity and magnetic field modeling and structure of the Chicxulub Crater, Mexico. *Journal of Geophysical Research: Planets* **99**, 13147–13162 (1994).
170. Valet, J.-P. *et al.* Constraining the age of the last geomagnetic reversal from geochemical and magnetic analyses of Atlantic, Indian, and Pacific Ocean sediments. *Earth and Planetary Science Letters* **506**, 323–331 (2019).
171. Daubar, I. J. & Kring, D. A. Impact-induced Hydrothermal Systems: Heat Sources and Lifetimes. 1727 (2001).
172. Ivanov, B., Deutsch, A., Ostermann, M. & Ariskin, A. Solidification of the Sudbury impact melt body and nature of the offset dikes - Thermal modeling. (1997).
173. Liang, X. *et al.* Warm Island Effect in the Badain Jaran Desert Lake Group Region Inferred from the Accumulated Temperature. *Atmosphere* **11**, 153 (2020).
174. Förste, C. *et al.* EIGEN-6C4 The latest combined global gravity field model including GOCE data up to degree and order 2190 of GFZ Potsdam and GRGS Toulouse. 55102156 Bytes, 3 Files GFZ Data Services https://doi.org/10.5880/ICGEM.2015.1 (2014).
175. Balmino, G., Vales, N., Bonvalot, S. & Briais, A. Spherical harmonic modelling to ultra-high degree of Bouguer and isostatic anomalies. *J Geod* **86**, 499–520 (2012).

176. Smith, R. A. Some depth formulae for local magnetic and gravity anomalies. *Geophysical Prospecting* **7**, 55–63 (1959).

177. Werner, S. Interpretation of magnetic anomalies at sheet-like bodies. *Sveriges Geologiska Undersok* **43**, (1953).

178. Hartman, R. R., Teskey, D. J. & Friedberg, J. L. A system for rapid digital aeromagnetic interpretation. *Geophysics* **36**, 891–918 (1971).

179. Barongo, J. O. Euler's differential equation and the identification of the magnetic point-pole and point-dipole sources. *Geophysics* **49**, 1549–53 (1984).

180. Marson, I. & Klingele, E. E. Advantages of Using the Vertical Gradient of Gravity for 3-D Interpretation. *Geophysics* **58**, 1588–1595 (1993).

181. Wedge, D. Mass anomaly depth estimation from Full Tensor Gradient gravity data. *IEEE Workshop on Applications of Computer Vision (WACV), Clearwater Beach, FL, USA* 526–533 (2013) doi:10.1109/WACV.2013.6475064.

182. Karimi, K., Shirzaditabar, F., Amirian, A. & Mansoobi, A. Center of Mass Estimation of Simple Shaped Magnetic Bodies Using Eigenvectors of Computed Magnetic Gradient Tensor. *JESP* **45**, 15–25 (2020).

183. Karimi, K., Oveisy Moakhar, M. & Shirzaditabar, F. Location and dimensionality estimation of geological bodies using eigenvectors of computed gravity gradient tensor. *JESP* **44**, 63–71 (2018).

184. Sanso, F., Barzaghi, R. & Tscherning, C. Choice of norm for the density distribution of the Earth. *Geophys J Royal Astronomical Soc* **87**, 123–141 (1986).

185. Nagy, D., Papp, G. & Benedek, J. The gravitational potential and its derivatives for the prism | SpringerLink. https://link.springer.com/article/10.1007/s001900000116.

186. Hartmann, W. K. & Gaskell, R. W. Planetary cratering 2: Studies of saturation equilibrium. Meteoritics 32, 109. doi:10.1111/j.1945- 5100.1997.tb01246.x. (1997).

187. Geophysical Data Analysis: Discrete Inverse Theory (Third Edition). in (ed. Menke, W.) xv–xxxvi (Academic Press, Boston, 2012). doi:10.1016/B978-0-12-397160-9.00016-3.